Personalized computational models of deep brain stimulation

A Dissertation
SUBMITTED TO THE FACULTY OF
UNIVERSITY OF MINNESOTA
BY

Benjamin Adam Teplitzky

IN PARTIAL FULFILLMENT OF THE REQUIREMENTS
FOR THE DEGREE OF
DOCTOR OF PHILOSOPHY

Advisor: Dr. Matthew D. Johnson

December 2016

Acknowledgements

I would like to acknowledge and thank my advisor, Matt Johnson for his mentorship, guidance, and encouragement. Working with Matt has been an absolute pleasure and I appreciate the time and effort he has dedicated to my development as a scientist and engineer. I look forward to passing along the knowledge and wisdom he's given me to those I mentor in the future. Matt's dedication to science, positive attitude, and engagement has made my time in the Neuromodulation Research and Technology Lab a truly great experience.

Thank you, members of my committee: Afshin Divani, Bob Meisel, Tay Netoff, and Kip Ludwig. I feel extremely fortunate to have had such excellent mentors and collaborators. I thank you all for your investments of time and energy in my personal, intellectual, and career development.

Thank you to all the members of the Neuromodulation Research and Technology Lab for all your help and support, so many of you were instrumental to the success of this work and my development as a scientist. I'd also like to thank my collaborators at the UMN Center for Magnetic Resonance Research and at the UMN Minnesota Supercomputing Institute, without whom, this work could not have been accomplished.

Thank you to my friends and family. I could not have come this far without your love and support. I would especially like to thank Chelsea Teplitzky, my wonderful wife to whom I was married while pursuing my PhD. Thank you for joining me on this adventure and for all your love and support. And thank you for our son, Louie Teplitzky who's changed my world. Thank you to my parents, Martha Lappin and Victor Teplitzky who have always supported me and encouraged me. Thank you also to my sisters, Kim and Jenna for all your love and support. I love you all so very much.

Finally, I would like to gratefully acknowledge my funding sources for making this work and my PhD training possible: The National Science Foundation Graduate Research Fellowship Program and Systems Neuroengineering IGERT (00006595 and DGE-1069104), the MnDRIVE (Minnesota’s Discovery, Research and Innovation Economy) initiative, the National Institutes of Health (R01-NS081118), and the Michael J. Fox Foundation.

Dedication

For Victor, Claire, and Marian

“Remember that all models are wrong; the practical question is how wrong do they have to be to not be useful.”
- George E. P. Box

Abstract

Deep brain stimulation (DBS) therapy is used for managing symptoms associated with a growing number of neurological disorders. One of the primary challenges with delivering this therapy, however, continues to be accurate neurosurgical targeting of the DBS lead electrodes and post-operative programming of the stimulation settings. Two approaches for addressing targeting have been advanced in recent years. These include novel DBS lead designs with more electrodes and computational models that can predict cellular modulation during DBS. Here, we developed a personalized computational modeling framework to (1) thoroughly investigate the electrode design parameter space for current and future DBS array designs, (2) generate and evaluate machine learning feature sets for semi-automated programming of DBS arrays, (3) study the influence of model parameters in predicting behavioral and electrophysiological outcomes of DBS in a preclinical animal model of Parkinson's disease, and (4) evaluate feasibility of a novel endovascular targeting approach to delivering DBS therapy in humans. These studies show how independent current controlled stimulation with advanced machine learning algorithms can negate the need for highly dense electrode arrays to shift, steer, and sculpt regions of modulation within the brain. Additionally, these studies show that while advanced and personalized computational models of DBS can predict many of the behavioral and electrophysiological outcomes of DBS, there are remaining inconsistencies that suggest there are additional physiological mechanisms of DBS that are not yet well understood. Finally, the results show how computational models can be beneficial for prospective development of novel approaches to neuromodulation prior to large-scale preclinical and clinical studies.

Table of Contents

List of Tables

List of Figures

List of Abbreviations

7 HuIM	7 Hu invariant moments
AC	Anterior commissure
ACA	Anterior cerebral artery
ACoA	Anterior communicating artery
ALIC	Anterior limb of the internal capsule
AN-Th	Anterior nucleus of the thalamus
CM/pf-Th	Centromedian/parafasicularis nucleus of the thalamus
CoM	Center of mass
CSF	Cerebrospinal fluid
CST	Corticospinal tract
CT	Computed tomography
DBS	Deep brain stimulation
DBSA	Deep brain stimulation array
DFT	Discrete Fourier transform
DoC	Disorder of consciousness
DTI	Diffusion tensor imaging
DWI	Diffusion weighted imaging
ET	Essential tremor
ETI	Electrode tissue interface
FDA	Food and drug administration
FEA	Finite element analysis
FFEM	Fourier finite element method
GPi	Globus pallidus internus
HDE	Humanitarian device exemption
IC	Internal capsule
ICV	Internal cerebral vein
iDFT	Inverse discrete Fourier transform
ITP	Inferior thalamic peduncle
latHyp	Lateral hypothalamus
LH	Lateral habenula
LN-Th	Lateral nucleus of the thalamus
LPFS	Legendre polynomial feature set

M1	Motor cortex
MER	Microelectrode recording
MPTP	1-methyl-4-phenyl-1,2,3,6 tetrahydropyridine
MUMPS	Multifrontal massively parallel sparse direct solver
NAc	Nucleus accumbens
NV	Normalized volume constraint
OCD	Obsessive-compulsive disorder
PAG/PVG	Periaqueductal gray/periventricular gray
PC	Posterior commissure
PD	Parkinson’s disease
pHyp	Posterior hypothalamus
PPN	Pedunculopontine nucleus
RoA	Region of activation
RPFS	Region properties feature set
SE	Scaled eigenvalue
SgCwm	Subgenual cingulate white matter
STN	Subthalamic nucleus
SWI	Susceptibility-weighted imaging
TRD	Treatment resistant depression
TS	Gilles de la Tourette Syndrome,
VC	Volume constraint
VC/VS	Ventral capsule/ventral striatum
Vc-Th	Ventralis caudalis nucleus of the thalamus
Vim	Ventrolateral intermedus nucleus of the thalamus
Vim-Th	Ventrolateral intermedus nucleus of the thalamus
VMH	Ventromedial hypothalamus
VPL/VPM	Ventral posterolateral/ventro-posteromedial nucleus of the thalamus
VS	Ventral striatum
VTA	Volume of tissue activated

1. Introduction

1.1.Deep brain stimulation

Deep brain stimulation therapy is used for managing symptoms associated with a growing number of neurological and cognitive disorders, particularly in cases where medication is ineffective or not well tolerated. In the United States, several brain areas have been approved or been granted a humanitarian device exemption (HDE) by the Food and Drug Administration (FDA) as targets for DBS therapy to treat the symptoms of essential tremor (ET) [1], Parkinson's disease (PD) [2], dystonia [3], and obsessive-compulsive disorder (OCD) [4]. To date, over 120,000 DBS leads have been implanted and DBS surgery has become common practice for treating subsets of patients suffering from these disorders.

DBS therapy was originally inspired by the practice of lesioning tissue within the globus pallidus internus (GPi) or the ventrolateral intermedus (Vim) nucleus of the thalamus for treating patients with severe idiopathic PD or ET, respectively [5,6]. While the mechanisms of DBS are not yet completely understood, perhaps the most elegant theory states that electrical stimulation acts as a reversible and adjustable information-lesion, thereby producing a similar therapeutic effect to anatomical lesioning [7,8]. Motivated by this hypothesis, a subset of putatively therapeutic DBS targets currently under investigation include those already recognized as lesion targets. For example, the anterior limb of the internal capsule (ALIC) for treatment resistant OCD [9] and the anterior cingulate for treatment resistant depression (TRD) [10]. Other putatively therapeutic DBS targets have been identified through studies using electrophysiology to relate stimulation of a particular brain region to a particular behavior (e.g. stimulation of the ventromedial and lateral hypothalamus for eating disorders [11]) or through serendipitous discovery (e.g. stimulation of the fornix for memory disorders [12]). Investigations into the safety and efficacy of delivering therapeutic electrical stimulation to numerous brain targets are currently underway and include both cortical and deep brain (Table 1) structures.

Table 1. Conditions and respective DBS targets: current and investigational.

Clinical disorder	Targeted neural region [13–18]
Parkinson’s disease	STN[a], GPi[a], PPN, CM/pf-Th
Essential tremor	Vim-Th[a], CM/pf-Th
Dystonia	GPi[b], STN[b]
Obsessive-compulsive disorder	ALIC[b], NAc, VC/VS, ITP, STN
Tourette syndrome	GPi, CM/pf-Th
Treatment resistant depression	SgCwm, VS, STN, GPi, ITP, NAc, ALIC, LH
Addiction	NAc
Cluster headache	pHyp
Chronic pain	PAG/PVG, VPL/VPM-Th, Vc-Th
Obesity/anorexia nervosa	VMH, latHyp, NAc
Alzheimer’s disease	Fornix
Epilepsy	CM/pf-Th, AN-Th, STN, hippocampus
Disorder of consciousness	LN-Th
Aggressive behavior	Hypothalamus

[a]*FDA approved,* [b]*Humanitarian device exemption*

ALIC=anterior limb of the internal capsule, AN-Th=anterior nucleus of the thalamus, CM/pf-Th=centromedian/parafasicularis nucleus of the thalamus, GPi=globus pallidus internus, ITP=inferior thalamic peduncle, latHyp=lateral hypothalamus, LH=lateral habenula, LN-Th=lateral nucleus of the thalamus, NAc=nucleus accumbens, PAG/PVG=periaqueductal gray/periventricular gray, pHyp=posterior hypothalamus, SgCwm=subgenual cingulate white matter, STN=subthalamic nucleus, Vc-Th=ventralis caudalis nucleus of the thalamus, VC/VS=ventral capsule/ventral striatum, Vim-Th=ventrolateral intermedus nucleus of the thalamus, VMH=ventromedial hypothalamus, VPL/VPM=ventral posterolateral/ventro-posteromedial nucleus of the thalamus, VS=ventral striatum.

1.2.Challenges associated with DBS

Deep brain stimulation is a procedure that is considered on an individual basis. The process generally begins with referral of a patient to a DBS surgical center by a patient’s primary physician who, in the case of PD or ET, may be a neurologist or movement disorders specialist. A patient’s primary physician and a neurosurgeon will generally work closely with the patient to consider potential costs and benefits of neurosurgical implantation of a DBS system. Patient selection criteria for DBS depend on the disorder being treated; however, consideration generally includes two key factors: potential therapeutic benefit and ability to tolerate surgery.

1.2.1. Therapeutic benefit and directional steering

Assessing the potential therapeutic benefit can be difficult, particularly in the case of novel DBS applications. Guidelines for assessing the potential therapeutic benefit have been proposed in the literature and continue to evolve as clinicians gain more experience using DBS for the treatment of a wide variety of brain disorders [19–22]. In the most common use-case for DBS, STN or GPi DBS for Parkinson's disease, the best predictor of therapeutic benefit is considered an excellent initial response to the drug, levodopa [23]. Within this subset of potential therapeutic responders, however, DBS efficacy is highly dependent on lead trajectory and placement [24].

The success of DBS therapy relies heavily on accurate electrode placement within the brain [25]. The stereotactic technique is used to deliver a DBS lead along a preplanned implantation trajectory to the correct depth. This technique has been advanced over several decades by high-precision instruments and improved medical imaging. However pre-operative imaging is commonly confounded by intra-operative brain shift [26–28]. Accurate lead placement facilitates precise electrical stimulation of the targeted brain region and avoidance of brain regions known to induce side-effects. The size of these anatomical targets, and their proximity to brain regions known to induce side-effects, dictate that leads be placed with millimeter-scale accuracy [29]. Attaining this level of accuracy is particularly difficult in the case of DBS because deep brain structures are targeted using implant trajectories that originate from the cranial surface. Therefore, small deviations from the surgical plan can result in large discrepancies between the planned final lead location and the actual lead location. Evidence of suboptimal lead placement can be gathered during surgery using intraoperative microelectrode recordings (MER) and electrical stimulation. This information can then be used to determine a new lead trajectory and allow for correction without additional surgical procedures. Following surgery, current steering may be used to compensate for small errors in final lead placement by adjusting stimulation parameters.

Currently, the process of DBS therapy is most commonly delivered using the Medtronic DBS system. The DBS leads currently offered by Medtronic consist of a stack of four 1.5 mm tall cylindrical shell electrodes distributed along a 1.27 mm diameter lead with electrode separation of 1.5 (model 3387) or 0.5 (model 3389). Such leads provide the opportunity to select the best electrode for stimulation in a manner that can compensate for leads that are placed more deep or shallow than planned [30–33]. In the case of PD, the optimal stimulation configuration is selected for a patient through monopolar review, whereby a clinician will systematically increase the stimulation amplitude using each electrode while assessing therapeutic benefit and side-effects [34]. If no optimal stimulation configuration is found using monopolar settings a clinician may explore bipolar settings as well. This programming method works well in the case of PD or ET where many of the motor signs and side-effects present quickly in response to stimulation, on the order of several seconds to minutes. However, the therapeutic effects of DBS on dystonia, for example, may take weeks to months to manifest and therefore make selection of stimulation parameters much more difficult [35].

Medical software and computational models made specifically for DBS applications have the potential to assist clinicians in both surgical planning and stimulation parameter selection. Such software provides the ability to plan surgical trajectories using patient-specific medical imaging data and to better select stimulation parameters by estimating a volume of tissue activated (VTA) using any number of electrodes and stimulation amplitudes. While such computational tools are useful for programming conventional DBS, they will become necessary for stimulation parameter selection as advancements in lead fabrication techniques enable DBS leads with more electrodes and more complex stimulation configuration possibilities. Such computational tools will also become necessary for selection of stimulation parameters for clinical indications in which DBS does not respond quickly to electrical stimulation.

As of 2016, new DBS lead designs with novel and potentially clinically advantageous features have been granted the European CE Mark and one has gained FDA approval for sale in US markets. Several of these novel designs include electrodes distributed radially around the lead, which allows for directional current steering in two dimensions rather than one. For this reason, these deep brain stimulation arrays (DBSA) are anticipated to improve patient outcomes by allowing clinicians to better customize stimulation to individual patients and better compensate for suboptimal DBS lead placement. However, selection of stimulation parameters using leads with more electrodes will require new approaches, as will be shown in the subsequent chapters, leveraging predictive modeling to help manage the increased number of stimulation options.

1.2.2. Surgical tolerance and vascular complications

In its current form, DBS has proven to be a safe and reliable treatment option for many patients; however, complications associated with craniotomy, meningeal damage, micro bleeds, ventricular penetration, and risk of severe hemorrhage disqualify many patients from surgical candidacy. These risks can be partially mediated by the use of high-precision instruments and improved medical imaging, but can be confounded by intra-operative brain shift [26–28], which may lead to unanticipated vascular damage and breaching the ventricular wall during MER and lead implantation [36]. Risk factors for the occurrence of hemorrhage in DBS surgery have been studied extensively and correlated with the use of MER, sulcal incursion, and breaching the ventricular walls [37–41]. The reported symptomatic effects of clearly observable vascular events following DBS surgery include increased relative risk of post-operative seizure [42], permanent neurological deficit [43], post-operative confusion [44], and subsequent extended hospital stays [45]. Reports on the symptomatic effects of small bleeds exist, but remain difficult to interpret as small bleeds are likely underreported [38] due to a lack of blood-sensitive pre- and post-operative imaging [36,46].

Patient factors shown to be correlated with increased risk of hemorrhage include hypertension [39,47], age [40,48], male gender [49], and vascular malformation [50]. These rates have also been shown to vary across target [51,52] and may relate to lead trajectory and target proximity to large blood vessels. For example, GPi DBS for PD carries a higher risk of hemorrhage than STN DBS [51–54] and this may be related to the close proximity of the A1 segment of the anterior cerebral arteries (ACA) to the ventral border of GPi. Alternatively, reports of cognitive complications for STN DBS are higher in comparison to GPi DBS and are correlated with the use of transventricular lead implantation trajectories [44].

Patient factors associated with hemorrhage and comorbidities such as dementia are utilized as exclusion criteria during prescreening for DBS surgical eligibility [55–59]. It is impossible to know the number of patients excluded from surgery due to risk factors associated with stereotactic lead implantation; however, one study showed that 30% of patients deemed eligible for STN DBS surgery by prescreening were later excluded, with reasons pertaining to neuropsychological disorders (48.3%) cited as the most common reason [56]. The same study found that 10% of excluded patients were poorly motivated for surgery, while a later survey assessment of patient receptivity to DBS for ET found that nearly two-thirds of patients interviewed would not consider undergoing surgery [60]. These studies indicate that risk factors, exclusion criteria, and patient reservations associated with transcranial lead implantation may leave a large population of medication-refractory patients underserved by DBS therapy [61]. The development of new and complementary techniques for delivering DBS may help to expand the patient population served by DBS. Technologies that are of particular interest include endovascular approaches (discussed in chapter 4) that enable electrodes to be implanted without penetrating brain tissue and microvasculature [62–64].

1.3.Computational modeling of DBS

Computational models of DBS generate a prediction of cellular activation during stimulation, which are represented spatially by defining a volume of tissue activated or by activation profile curves that are brain region specific. These models provide a platform to study DBS therapy in a manner that complements experimental studies. In the past two decades computational models have been used in studies to explore mechanisms of DBS [8,65], to guide surgical planning and patient programing [66–69], and to evaluate novel DBS lead designs [70–72]. Advancements in model complexity and available computational power have improved the usefulness of these models by enabling the creation of individualized or ‘personalized’ models of DBS. These personalized models rely on medical imaging data to reflect subtle aspects of neural anatomy and generate model solutions that are specific to individual patients. Using anatomical medical imaging data, models of DBS span the macro and micro scale by combining a patient-specific volume conductor model of the brain with multi-compartment cell models populated throughout brain regions that are segmented and reconstructed.

1.3.1. Volume conductor models of the brain

Volume conductor models of the brain incorporate electrical properties of tissue and provide the means to solve for time and spatially dependent electric potential in the brain during stimulation. These models rely on the governing equations of electromagnetic phenomena, Maxwell's equations. Stimulation waveforms used in DBS have a spectrum with minimal power above 10 kHz allowing for the use of a simplified set of equations known as the quasistatic formulation [73]:

Law of conservation of charge: $$\nabla \cdot J = 0 \tag{1}$$

Gauss' law: $$\nabla \cdot E = \frac{\rho}{\varepsilon} \tag{2}$$

Ohm's law: $$J = \sigma E \tag{3}$$

Electric field by definition: $$E = -\nabla \Phi \tag{4}$$

where J is the current density, E is the electric field, Φ is the scalar electric potential, σ is the conductivity, ρ is the charge density, ε is the permittivity. From the quasistatic formulation, assuming an infinite and homogenous medium, the domain equation for simple point source volume conductor models can be derived and used to calculate electric potential in tissue during stimulation.

For a monopolar source: $$\Phi = \frac{I}{4\pi\sigma r} \tag{5}$$

For a bipolar source: $$\Phi = \frac{I}{4\pi\sigma}\left(\frac{1}{r_1} - \frac{1}{r_2}\right) \tag{6}$$

where r is the distance between the point source and the point where electric potential is measured. For bipolar sources, the subscript 1 and 2 represent the anodic and cathodic point sources, respectively. These point source models were utilized in early modeling studies of DBS [74,75] and under specific conditions, provide valid estimates of electric potential in tissue during microelectrode stimulation [76] and DBS [77]. Point source models can be expanded upon to include multiple sources, anisotropic homogenous mediums, and semi-infinite inhomogeneous mediums. However, point source models cannot be used to compare different lead designs, represent anatomically correct brain/head models, or incorporate anatomically correct inhomogeneous and anisotropic tissue properties. Modeling of these aspects require the use of numerical techniques such as finite element analysis (FEA) or boundary element analysis and rely on discretized representations of the brain and DBS lead to solve a more generalized domain equation, which can be derived from the quasistatic formulation and used to solve for electric potential in tissue during stimulation. Using Eqs. 1, 3, and 4, the domain equation takes the following form:

$$\nabla \mathrm{J} = \nabla \cdot \sigma \mathrm{E} = \nabla \cdot \sigma \nabla \Phi = 0 \tag{7}$$

and is solved using FEA in the context of applied boundary conditions. Expanding the conductivity parameter to incorporate capacitive and dispersive tissue properties results in the formulation of the time-harmonic electro-quasistatic equation:

$$\nabla \cdot [\sigma(\omega) + j\omega\varepsilon_0\varepsilon_r(\omega)]\nabla\Phi = 0 \tag{8}$$

where ω is angular frequency, j is the imaginary unit, ε_0 is the permittivity of free space (8.85 x 10^{-12} F/m), ε_r is relative permittivity.

1.3.2. Inhomogeneous and anisotropic electrical properties of brain tissue

Accurate calculation of the voltage in tissue during electrical stimulation is highly dependent on accurate representations of the electrical properties of tissue. Early studies investigating the electrical properties of tissue demonstrated that conductivity and relative permittivity in brain tissue are frequency dependent [78] and vary for different tissues within the brain [79,80]. In a series of journal articles published in 1996 by Gabriel et al., the authors performed a comprehensive analysis of electrical properties of various biological tissues including brain gray matter, brain white matter, cerebrospinal fluid, and blood. Gabriel et al. experimentally characterized the electrical properties of these tissues

[81], performed a comprehensive meta-analysis of literature on the subject [82], and generated a mathematical model from which conductivity and relative permittivity of the investigated tissues can be calculated [83].

The Gabriel dispersion equation provides the means to generate detailed model of the brain that is inhomogeneous and dispersive. However, it does not accurately represent anisotropy, which exists in gray matter and is prominent in white matter [84]. Previous DBS computational modeling studies have established that subject-specific inhomogeneous and anisotropic tissue property maps can significantly impact model predictions [85–87] and this effect is primarily attributed to the close proximity of DBS target brain structures to highly anisotropic axonal fiber tracts. Several methods have been proposed within the literature to model anisotropy, each relying on diffusion tensor imaging (DTI).

DTI is a medical imaging technique based on MRI, which is used to map the diffusion of water molecules in tissue. The image contrast is generated by the diffusion of water molecules in response to the application of multiple magnetic field gradients. In 2001 Tuch and colleagues demonstrated a linear relationship between the diffusion of water molecules and ion movement in the brain, which allows for the calculation of an anisotropic conductivity tensor from DTI [88]. Using this relationship, the matrix of conductivity tensor eigenvalues (Λ_σ) is calculated by scaling the diffusion tensor eigenvalues (λ_1, λ_2, and λ_3) by a factor s:

$$\Lambda_\sigma = s * \begin{bmatrix} \lambda_1 & 0 & 0 \\ 0 & \lambda_2 & 0 \\ 0 & 0 & \lambda_3 \end{bmatrix} \tag{9}$$

The anisotropic conductivity tensor (σ) is then calculated from its eigendecomposition using the matrix of DTI eigenvectors (V):

$$\sigma = V \Lambda_\sigma V^T \tag{10}$$

In addition to the Tuch method for incorporating anisotropy, several other methods have been proposed within the literature, whereby the matrix of conductivity tensor eigenvalues is calculated differently. Examples include: (1) constraining the volume of each diffusion tensor and imposing a predefined anisotropy ratio [89] and (2) normalizing each diffusion tensor eigenvalue by the diffusion tensor volume and scaling the result by the isotropic conductance value for the appropriate tissue [90]. Each of these techniques generates personalized tissue property maps that are used to create personalized computational models that are inhomogeneous, anisotropic, and in the case of the two examples provided, allow for the inclusion of dispersion. To calculate the potential in tissue during electrical stimulation using these complex tissue property maps, simple electrostatic or time-domain FEA stimulations cannot be utilized. Rather, the analysis must be performed in the frequency domain following the technique described by Butson and McIntyre in 2005 for neurostimulation applications [91], termed the Fourier finite element method.

1.3.3. Waveform modulation using the Fourier finite element method

The Fourier finite element method (FFEM) allows for computation of a time-dependent stimulation waveform throughout the volume conductor model. For models of DBS, the FFEM involves first transforming the stimulation pulse into the frequency domain using the discrete Fourier transform (DFT). Next, FEA is performed in the frequency domain for stimulation at each of frequency bins contained within the DFT solution. To capture the dispersive effects in tissue, tissue properties may be assigned for each FEA frequency using the appropriate frequency-dependent values from the Gabriel dispersion equation. Next, at any coordinate within the finite element model, the complex voltage from the FEA solution is used to scale and shift the DFT result. Finally, the inverse DFT (iDFT) of the scaled and shifted spectrum is used to generate a time-dependent stimulation waveform that has been sculpted by the resistive, capacitive, and dispersive aspects of the tissue map.

Using the FFEM in combination with personalized volume conductor models of the brain provides the ability to model small changes in the time-dependent stimulation waveforms delivered using DBS. Ultimately, however, the effects of DBS are dependent on cellular responses to stimulation. Therefore, multi-compartment cell models are paired with volume conductor models to generate spatial activation profiles and activation profile curves.

1.3.4. Modeling cellular activation

Volume conductor models provide the means to estimate potential in brain tissue during stimulation; however, the ultimate goal is to understand the impact of electrical stimulation on neurons. Simple equivalent circuit models of axons are used for this purpose. For example, a length of axon membrane, or node, may be modeled using a capacitance (C_m) to represent the resting cell membrane, placed in parallel with a battery, representing the resting potential of the cell, and a resistance (R_m), representing the resistance of the membrane ion channels connected in series. A fiber can then be created by linking multiple nodes together using an axial resistance that represents the axon internal resistance. Simulating the response of this circuit to an applied electric field can be performed using circuit modeling software such as Simulink or the Neuron programming environment [92]. The cellular response to stimulation, firing of an action potential or not, is dependent on the transmembrane potential (V_m), which is the difference between the intracellular and extracellular (V_e) voltage minus the resting potential. An action potential occurs when the difference of the extracellular voltage across two nodes is large enough to cause a transmembrane potential that exceeds the threshold potential of the cell, which opens voltage gated sodium channels. Relying on these principles and using Kirchoff's law, one can formulate the nonlinear cable equation for unmyelinated axons [73,93]:

$$\lambda^2 \frac{\partial^2 V_m}{\partial x^2} + \tau_m \frac{\partial V_m}{\partial t} - V_m = -\lambda^2 \frac{\partial^2 V_e}{\partial x^2} \tag{11}$$

where λ is the space constant:

$$\lambda = \frac{1}{2}\sqrt{\frac{R_{sm} d}{R_a}} \tag{12}$$

where R_{sm} is the specific membrane resistance, R_a is the axoplasmic-specific resistance, and d is the axon diameter. The axon time constant, τ_m, is given by:

$$\tau_m = R_m C_m \tag{13}$$

Further, one can model the effect of an applied electric field on a myelinated axon using the discrete cable equation for myelinated axons [94,95]:

$$\frac{R_n}{R_a}\Delta^2 V_m - R_n C_n \frac{\partial V_m}{\partial t} - V_m = -\frac{R_n}{R_d}\Delta^2 V_e \tag{14}$$

where R_n is the membrane resistance at the node of Ranvier, R_a is the resistance between adjacent nodes, C_n and is the capacitance at the node of Ranvier:

$$R_n = \frac{R_{sn}}{\pi d l} \tag{15}$$

$$R_a = \frac{4R_{sa}L}{\pi d^2} \tag{16}$$

$$C_n = C_{sn}\pi d l \tag{17}$$

where d is the unmyelinated fiber diameter, l is the node of Ranvier length, L is the distance between nodes, and the subscript s indicates specific resistance or capacitance of the membrane at the nodes. This set of equations differs from the unmyelinated cable equation in that is takes into account the presence of the myelin sheath, which causes action potential propagation to occur through salutatory conduction. For axon models within the central nervous system, such as those presented within this thesis, the anatomy generally mandates the use of the cable equation for myelinated axons.

Modeling of cellular activity that was performed in the following sections of this thesis utilized populations of individual multi-compartment axon models are used to predict cellular activation. These models are based on the McIntyre et al. double-cable model of a generalized mammalian nerve fiber [96], which represents the axon as a repeating series of compartments representing different aspects of a myelinated axon, with a single compartment representing each node of Ranvier. Simulating the response of the double-cable model of a generalized mammalian nerve fiber is performed using Neuron programming environment [92] by applying an extracellular voltage to each compartment that is consistent with the voltage calculated from FEA volume conductor model solution during DBS. Quantifying the cellular responses from a population of model axons was performed by varying the stimulation amplitude in order to determine the minimum amplitude that results in the occurrence of an action potential for each model neuron within the population. Using the stimulation threshold for each axon, axons which are activated by stimulation at specific amplitudes are grouped to define a spatial activation profile or an activation profile curve.

1.4.Objectives and research goals

Despite high interest in personalized models of deep brain stimulation that combine highly complex volume conductor models with multi-compartment cell models, these models are underutilized for assessment of novel electrode technologies. Additionally, while these models provide the means to estimate cellular responses to electrical stimulation with a high degree of precision, the accuracy of these estimates are dependent on assumptions regarding tissue electric properties and the placement and biophysics of cellular models. The following chapters of this thesis describe computational modeling efforts to evaluate novel DBS electrode designs in the context of relevant anatomical models and seek to address the issue of model validation using behavioral and electrophysiological measures.

Chapter 2 describes the development of a computational model to evaluate the utility of DBS arrays with increasing numbers of electrodes distributed around a DBS lead. This study compared the ability of various lead designs to steer current using quantified measures. This study then evaluated the accuracy of several machine learning feature sets for predicting the optimal stimulation configuration using a four radial electrode deep brain stimulation array. Chapter 3 describes the development of a personalized computational model of deep brain stimulation using a preclinical animal model for computational model validation. In this study, model predictions using a range of personalized tissue property maps were evaluated using experimental data, which included behavioral responses and electrophysiological recordings from motor cortex. Chapter 4 describes the development of a personalized model of endovascular DBS. This study used a personalized model to map out the neurovasculature of a single-subject and compare the effects of endovascular DBS to conventional DBS using two investigational brain targets.

2. DBS array design and machine learning feature sets

This chapter reprinted with permission from Frontiers in Computational Neuroscience.

Teplitzky BA, Zitella LM, Xiao Y and Johnson MD (2016) Model-Based Comparison of Deep Brain Stimulation Array Functionality with Varying Number of Radial Electrodes and Machine Learning Feature Sets. Front. Comput. Neurosci. 10:58. doi: 10.3389/fncom.2016.00058

2.1.Overview

2.1.1. Objective

Deep brain stimulation (DBS) leads with radially distributed electrodes have potential to improve clinical outcomes through more selective targeting of pathways and networks within the brain. However, increasing the number of electrodes on clinical DBS leads by replacing conventional cylindrical shell electrodes with radially distributed electrodes raises practical design and stimulation programming challenges.

2.1.2. Approach

Computational modeling was used to investigate: (1) how the number of radial electrodes impact the ability to steer, shift, and sculpt a region of neural activation (RoA), and (2) which RoA features are best used in combination with machine learning classifiers to predict programming settings to target a particular area near the lead. Stimulation configurations were modeled using 27 lead designs with one to nine radially distributed electrodes. The computational modeling framework consisted of a three-dimensional finite element tissue conductance model in combination with a multi-compartment biophysical axon model. For each lead design, two-dimensional threshold-dependent RoAs were calculated from the computational modeling results.

2.1.3. Main results

The models showed more radial electrodes enabled finer resolution RoA steering; however, stimulation amplitude, and therefore spatial extent of the RoA, was limited by charge injection and charge storage capacity constraints due to the small electrode surface area for leads with more than four radially distributed electrodes. RoA shifting resolution was improved by the addition of radial electrodes when using uniform multi-cathode stimulation, but non-uniform multi-cathode stimulation produced equivalent or better resolution shifting without increasing the number of radial electrodes. Robust machine learning classification of 15 monopolar stimulation configurations was achieved using as few as three geometric features describing a RoA.

2.1.4. Significance

The results of this study indicate that, for a clinical-scale DBS lead, more than four radial electrodes minimally improved in the ability to steer, shift, and sculpt axonal activation around a DBS lead and a simple feature set consisting of the RoA center of mass and orientation enabled robust machine learning classification. These results provide important design constraints for future development of high-density DBS arrays.

2.2. Background

Deep brain stimulation is a neurosurgical intervention for symptomatic treatment of a number of brain disorders. The success of DBS therapy relies on accurate electrode placement within the brain [25] and generation of spatially defined tissue voltage distributions that can precisely modulate brain activity with millimeter, or even sub-millimeter resolution [29]. The size of the anatomical targets, and their proximity to neural pathways that when stimulated generate unwanted side-effects, making selective modulation challenging for this therapy. Commercial DBS leads currently consist of a stack of cylindrical shell electrodes that can accommodate current steering along the lead axis [30–33]. Such current steering can be useful for enhancing the ability to target the subthalamic nucleus [67,85,97], globus pallidus [98,99], and motor thalamus [85,97,100]. However, the cylindrical electrode design of current DBS leads produces predominantly axisymmetric modulation of neuronal activity [100]. This axisymmetric modulation enables inadequate flexibility to adapt stimulation to compensate for neurosurgical targeting errors tangential to the DBS lead [100,101] or for targeting anatomical regions with complex geometries [87,102]. In such cases, delivering therapy without evoking side effects such as phantom sensory perceptions, involuntary motor contractions, and cognitive/mood changes can be challenging [31,67,100].

The concept of current steering with implantable electrode arrays has existed in the fields of spinal cord stimulation [103,104], intracochlear stimulation [105,106], and retinal stimulation [107,108] for some time. Recent computational and experimental work has also applied this concept to preclinical and clinical DBS electrode arrays, which employ three to four radially distributed electrodes per row and several rows per lead [101,109–113]. Such DBS arrays have potential to improve steering, shifting, and sculpting of neural activation beyond the capacity of conventional DBS leads with cylindrical shell electrodes. However, it is presently not clear how the number of radial DBSA electrodes impact the ability to steer, shift, and sculpt a region of neural activation.

In addition to the challenges associated with understanding current steering with DBS arrays, leads with more than the conventional four electrodes have the potential to create significant patient programming challenges. Currently, clinicians select programing settings for a patient using trial-and-error through a monopolar review. A clinician will systematically stimulate through each of the available electrodes using increasing stimulation amplitudes, evaluate the patient's symptoms and the presence of side effects, and select the optimal stimulation configuration for the patient [34]. With only four electrodes this can be a time consuming and imprecise task. Increasing the number of electrodes has the potential to greatly complicate this problem, making programming impractical or even infeasible in a clinical setting. To address this issue, model based optimization algorithms [114] and machine learning classifiers [115] have been proposed. In general, the goal of these algorithms is to use medical imaging to determine the location of an implanted DBS lead relative to the targeted brain region and using this information, predict potentially therapeutic stimulation settings in order to guide the clinician in programming the implanted DBS system. Implementation of such techniques; however, relies heavily on the identification of robust quantifiable measures, or features, that describe the desired region or volume of activation. Currently, it remains unclear which RoA features are best used in combination with machine learning classifiers to predict programming settings to target a particular area near a DBSA.

In the first section of this manuscript we used computational modeling to explore DBSA lead design and current steering strategies. In particular, we calculated the maximum stimulation amplitude for various DBSA designs in the context of charge injection and charge storage capacity limits. We then investigated the size, shape, and location of a region of neural activation resulting from stimulation using a variety of electrode configurations within these limits. In the second section of this manuscript, we evaluate various machine learning feature sets for predicting stimulation settings to target a particular region near the DBS lead.

2.3.Methods

2.3.1. Radially segmented DBS arrays

Twenty-four deep brain stimulation array and three non-array leads were created in COMSOL Multiphysics v4.4. DBSA leads included two to nine electrodes per row. Each DBSA electrode was constructed by projecting an ellipse onto the cylindrical lead body and extruding the resulting surface 0.1 mm into the lead body. The width of the projected ellipse (Figure 1) was calculated using the equation of a chord whose endpoints lie on a circle with a diameter equal to the lead body diameter, 1.27 mm (Equations 18, 19).

$$\Theta = \frac{360}{n} \tag{18}$$

$$electrode\,width = d * \sin\left(\frac{\Theta}{2}\right) \tag{19}$$

where Θ was the center-to-center electrode separation, d was the lead body diameter, and n was the number of radial electrodes in a row. Non-array leads included conventional cylindrical shell electrodes. Both array and non-array electrodes were constructed with three heights: 0.5, 1.0, and 1.5 mm. Each DBS lead included four rows of electrodes and the separation between rows was equal to electrode height. Each lead diameter was 1.27 mm in accordance with the diameter of the clinical Medtronic 3387 and 3389 DBS leads (Medtronic Inc., Minneapolis, MN). To simplify reference to each DBS lead design, the following naming convention was implemented: DBSA–e[number of radial electrodes]–h[electrode height]. For example, DBSA–e4–h1.5 would refer to the DBSA lead with 4 radial electrodes per row, each with a height of 1.5 mm.

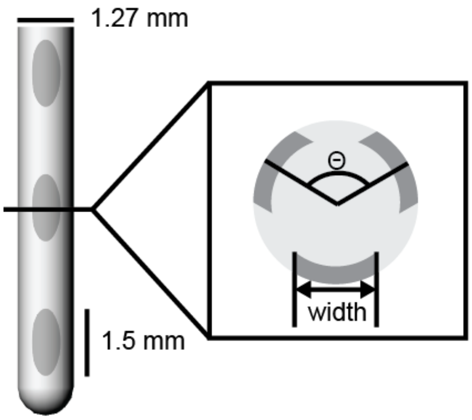

# of radial contacts	Electrode width (mm)	Radial separation Θ (degrees)
2	0.898	180
3	0.635	120
4	0.486	90
5	0.3925	72
6	0.3287	36
7	0.2826	51.4
8	0.2478	45
9	0.2205	40

Figure 1. DBSA lead design. DBSA leads were designed with two to nine electrodes per row. DBSA electrode width and radial separation were calculated for each lead design using Equations (18, 19). The DBSA–e3–h1.5 lead design is shown. Electrode height was 1.5 (shown), 1.0, or 0.5 mm. *Tissue conductance models*

Simulations were conducted using only the bottom row of electrodes for each lead. A three-dimensional tissue conductance model was created for each stimulation configuration using Comsol Multiphysics v4.4 and solved for using the finite element method (FEM; Figure 2A). Each tissue model incorporated a lead body (σ = 1e−12 S/m), electrodes (σ = 1e6 S/m), a 0.25 mm thick encapsulation layer (σ = 0.18 S/m [116,117]), and a 20 cm diameter sphere representing bulk neural tissue (σ = 0.3 S/m [79,80]). Point current-sources were placed at the three-dimensional center of each electrode. The surface of the bulk neural tissue sphere was set to ground, i.e., zero volts, via Dirichlet boundary conditions. A variable resolution mesh containing quadratic tetrahedral elements ranging from 0.2 mm near the electrode to 10 mm near the model perimeter was generated via Delaunay triangulation. The resulting mesh contained 280,000–310,000 elements depending on the lead design. To confirm that further mesh refinement was not advantageous, the average relative change in the calculated potentials were determined at the midpoint of each axon model compartment using a mesh with elements that were two and three times smaller than the previously described model. The average relative change in the calculated potentials was found to be < 1% for these more refined models.

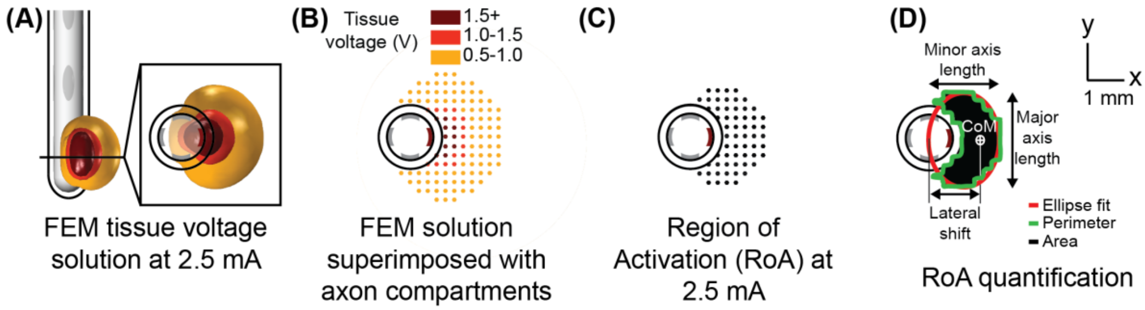

FEM tissue voltage solution at 2.5 mA

FEM solution superimposed with axon compartments

Region of Activation (RoA) at 2.5 mA

RoA quantification

Figure 2. Modeling axonal activation. Tissue voltage during stimulation was modeled for each stimulation configuration using the finite element method (A). The multi-compartment axon model population superimposed with extracellular potentials derived from the tissue voltage predictions (B). A spatial axonal activation profile, or region of activation (RoA) plot resulting from stimulation at 2.5 mA (C). RoA quantification using regional properties calculated from a closed binary image of the RoA plot (D).

To investigate impact of the changes to the electrode-tissue interface (ETI) resulting from novel electrode geometries, a three-element Randles equivalent circuit model of the ETI was constructed for the lead with the smallest and largest electrode surface areas. In these models, the Fourier FEM described by Butson and McIntyre [91] was implemented so that capacitive effects of the ETI could be captured. Briefly, the Fourier FEM was carried out by creating a waveform with a 90 μs cathodic pulse in the time domain (dt = 1 μs), performing the 1024 point discrete Fourier transform (DFT), solving the finite element model ($\varepsilon_r = 1 \times 10^6$ [83]) at each of the 513 frequencies represented within the DFT (0–512 kHz), scaling and phase shifting the finite element model results by the DFT magnitude and phase, and finally performing the 1024 point inverse DFT on the result to reconstruct the stimulation waveform in the time domain. The equivalent circuit model was represented at the electrode surface within the frequency dependent finite element model as a circuit terminal using the Comsol Multiphysics AC/DC module. In accordance with previous work [118], the equivalent circuit model included an access resistance, Ra, in series with a parallel RC pair consisting of a faradaic resistance, Rf, and double layer capacitance, Cdl. Ra was calculated using the finite element model solution for 1 volt applied at the electrode surface from which the effective applied current was calculated by integrating the normal current density across the electrode surface and taking the reciprocal. Rf and Cdl were calculated from the distributed faradaic resistance (150 Ω-cm^2 [119]) and the distributed double layer capacitance (30 μF/cm^2 [119]) using the electrode surface area. Inclusion of the ETI was confirmed to have no discernable impact on the stimulation results, and thus the ETI equivalent circuit model was excluded from subsequent simulations.

2.3.3. Stimulation configurations

Current-regulated stimulation was modeled using one or multiple independent sources. Variations on stimulation configuration were constrained to monopolar settings and included single-cathode stimulation, uniform multi-cathode stimulation, and non-uniform multi-cathode stimulation. Uniform multi-cathode stimulation involved uniformly splitting the total cathodic current across all designated cathodes. Non-uniform multi-cathode stimulation involved assigning different proportions of total cathodic current to a single, primary cathode, and evenly distributing the remaining cathodic current across the remaining electrodes in a given row. Simulations of 15 monopolar single-cathode and uniform multi-cathode stimulation configurations using only the DBSA–e4–h1.5 lead were used for machine learning feature set analysis.

2.3.4. Multi-compartment axon models

Three-dimensional multi-compartment myelinated axon models were distributed within a lead-centered 13-by-13 mm grid. Axons were separated by 0.25 mm and aligned parallel to the DBS lead. While the axon model orientations were generated in an artificial framework, the orientations were generally similar to fiber tracts (e.g., corticospinal tract of internal capsule) [115] that course approximately parallel to clinical DBS lead targets (e.g., subthalamic nucleus DBS) and that are hypothesized to elicit side effects when stimulated [120]. Fibers were modeled with a 2 μm diameter [121] and populated with compartments representing nodes of Ranvier, myelin attachment segments, paranode main segments, and internode segments connected through an axial resistance. Axon compartment properties were consistent with the multi-compartment cable model axon developed and described in detail by McIntyre et al. [122].

Rather than incorporating tissue conductance using the computationally expensive Fourier FEM method, the quasistatic solution at each axon compartment was scaled by a time-varying experimentally-recorded 135 Hz charge-balanced current-regulated stimulation waveform [123] (Equation 20).

$$\Phi(x, y, z, t) = \Phi(x, y, z) * w(t) \tag{20}$$

Extracellular potential, represented by Φ for a given model axon compartment was scaled by the time varying 135 Hz waveform, *w(t)*. The charge-balanced waveform consisted of a 90 μs pulse followed by a 400 μs interphase delay and a 3 ms pulse with opposite polarity. The waveform-scaled extracellular potential was dynamically incorporated into the model axon compartments (Figure 2B) using the Neuron programming environment v7.3 [124]. Within the Neuron programming environment, the axonal membranes were perturbed by driving membrane current using the extracellular mechanism (*e_extracellular*), with parameters consistent with previous work [102].

2.3.5. Calculating neural activation thresholds and regions of activation

The total applied cathodic current threshold for inducing axonal spiking was calculated for each model axon within each tissue voltage model using a binary threshold-searching algorithm. The algorithm relied upon trial-and-error within a narrowing range of stimulation amplitudes that was considered to have converged once the range of stimulation amplitudes was reduced to 0.01 mA. Axons were considered “activated” if an action potential was recorded within 3 ms of stimulation following 8 out of 10 stimulation pulses at the distal node of Ranvier. For each stimulation configuration, two-dimensional spatial activation plots, referred to as region of activation (RoA) plots, were generated by plotting the cross-section of the axon population with activation-thresholds less than or equal to a specified stimulation amplitude (Figure 2C). Where charge storage capacity and charge injection limits were considered, the maximum safe stimulation amplitude was calculated using Equations 21 and 22, respectively. The reversible charge storage capacity, 150 $\mu C/cm^2$, represented the upper limit of reported values [125,126] for platinum-iridium electrodes like those generally used in DBS for cathodic-pulse leading charge balanced waveforms. The charge injection limit was characterized by a safety factor, k = 2.0, was derived from the charge per phase verses charge density per phase relationship [125,127] as a limit for safe charge delivery to neural tissue.

$$I_{CSC} = \frac{CSC \times A}{pw} \tag{21}$$

$$I_{SF} = \frac{\sqrt{A \times 10^{k}}}{pw} \tag{22}$$

With stimulation amplitude in amperes, *I*; charge storage capacity in μC/cm^2, *CSC*; surface area of a single electrode in cm^2, *A*; and cathodic pulse-width, *pw*.

2.3.6. RoA quantification

Binary image analysis techniques were used to extract quantifiable metrics from each RoA at amplitudes ranging from 1 to 5 mA in 0.1 mA increments resulting in 41 RoAs per stimulation configuration. These techniques were used for quantification rather than precise measurement of the spatial activation profile to ensure that the process could be replicated in the context of post-operative medical imaging for the purpose of patient programing. Post-processing began with saving RoA plots spanning the 13-by-13 mm axon-space within 20-by-20 cm lead-centered images. A binary transform of each image was performed and morphologically closed using disk-shaped elements in order to preserve the ellipsoidal nature of the region. Regional properties including area, perimeter, center-of-mass (CoM), major axis length, and minor axis length were extracted from each of the closed images (Figure 2).

From these regional properties, several metrics were calculated to compare lead designs. These included lateral shift, angular shift, aspect ratio, target region coverage, and target region overspill. Lateral shift was calculated as distance from the lead-center to the RoA CoM in the direction of the primary cathode (usually along the x-axis). Angular shift, in the context of single-cathode stimulation through two neighboring electrodes, was calculated as the angle, in degrees, between vectors running from the lead-center to each RoA CoM. Aspect ratio was calculated as the RoA minor axis length divided by the RoA major axis length. Target region coverage and overspill were calculated for a set of experiments where a target region was placed between neighboring electrodes. These experiments were run using only the DBSA–e4–h1.5, which has electrodes separated by 90°. The target region, therefore, was generated from the same lead but was rotated 45° about the lead-center. Overlap between the target region and the activated region was calculated by first multiplying the binary image transforms of the two regions and then calculating the percent of the target region area covered by the overlapped region. Overspill was estimated by multiplying the binary image transforms of the activated region and the inverse of the target region, and then calculating the resulting area in mm2. Overlap and overspill were calculated for stimulation amplitudes ranging from 1 to 5 mA at 0.1 mA increments using three monopolar configurations. All processing and calculations of regional properties were performed using the Matlab Image Processing Toolbox (v2014b).

2.3.7. Feature sets

Feature sets (Table 2) were derived from simulations of 15 monopolar stimulation configurations using the DBSA–e4–h1.5 lead (Figure 3). Because RoA measures were conducted at 41 amplitudes (1 to 5 mA in 0.1 mA increments) using 15 stimulation configurations, feature sets for 41 × 15 = 615 RoAs were generated. Post-processing of RoA plots was performed using the same binary image analysis techniques as described in Section 2.3.6. From the post-processed binary images, three feature sets were generated: a region properties feature set (RPFS), a Legendre polynomial feature set (LPFS) [128], and a 7 Hu invariant moments feature set (7 HuIM) [129]. The RPFS included the common region properties; center or mass, area, perimeter, convex hull area, solidity as well as features derived from an ellipse fit to the RoA; eccentricity, orientation, major axis length, and minor axis length. The LPFS was generated using the distance transform of each RoA binary image. The distance transform results were sorted in ascending order, normalized to the largest value, and fit to a 9th order Legendre polynomial. The features consisted of the coefficients of this 9th order Legendre polynomial. The majority of features that were investigated originate from computer vision applications where desirable traits include invariance to scale, rotation, and translation [130]. We hypothesized that the ideal feature set for prediction of stimulation configuration would (1) be rotation and translation variant since RoA direction underlies current steering, and (2) scale invariant with regard to stimulation amplitude but not with regard to RoA offset. To achieve this, distance of the RoA CoM from lead-center in the x and y directions were included in each feature set.

Table 2. Features extracted from simulations using the DBSA-e4-h1.5 lead.

Number	Feature
1	Center of mass x-coordinate
2	Center of mass y-coordinate
3	Eccentricity of ellipse fit
4	Orientation of ellipse fit
5	Major axis length of ellipse fit
6	Minor axis length of ellipse fit
7	Area
8	Perimeter
9	Convex hull area
10	Solidity
11-20	Legendre polynomial coefficients from distance transform [128]
20-27	7 Hu invariant moments [129]

Twenty-seven features were extracted from each RoA. The region properties feature set (RPFS) included features 1 through 10. The Legrendre polynomial feature set (LPFS) included features 1, 2, and 11 through 20. The 7-Hu invariant moments feature set (7HuIM) included features 1, 2, and 20 through 27.

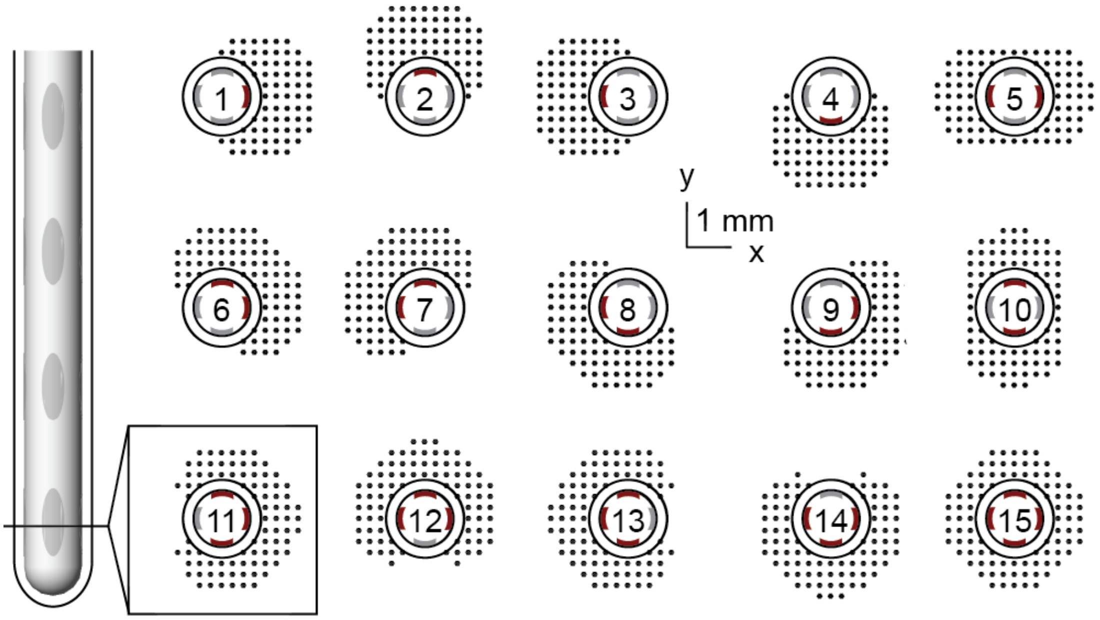

Figure 3. Machine learning feature set generation. Machine learning features were extracted from simulation results spanning 15 monopolar stimulation configurations at simulation amplitudes ranging from 1 to 5 mA in 0.1 mA increments.

2.3.8. Classification and feature set quality assessment

Each of the 615 samples in the proposed classification problem included all features (Table 2) from a single RoA. The goal of the classification problem was to classify each sample, using a subset of features i.e., one of the three feature sets, as originating from the correct stimulation configuration, of which there were 15. The quality of each feature set was assessed using 10-fold cross validation of five classification models: k-nearest neighbor (KNN), naïve Bayes (NB), a multi-class support vector machine (mSVM) with a radial-basis function kernel [131], a two-layer feed-forward pattern recognition neural network (NN) with 20 hidden elements, and a random forest (RF) decision tree ensemble with 100 trees [132]. All models except the mSVM were implemented using the Matlab Statistics Toolbox (v2014b). Training and testing data sets were pseudo-randomly divided within each cross validation fold such that each class was represented approximately equally and no samples were used for both training and testing. Classification accuracy was calculated for each fold as the number of correctly classified samples divided by the number of classified samples. The mean accuracy and standard error of the accuracy were then calculated across all 10 folds.

Feature importance was assessed using sequential forward selection and Breiman's random forest algorithm. Sequential forward selection was performed using the neural network and naïve Bayes classifiers. In each case, starting with an empty feature set, the classifier was run using each of the 27 features and the feature with the highest accuracy was considered the most important and added to the feature set. Classification was then performed using each of the remaining 26 features in combination with the first elected feature, and again the feature with the highest accuracy was considered the most important and added to the feature set. This process was repeated until the feature set contained 10 of the 27 features. From the random forest classifier, feature importance was assessed by calculating the increase in prediction error that resulted from random permutation of each feature across the out-of-bag samples. Features with the greatest effect on error were considered the most important.

2.4. Results

2.4.1. Stimulation amplitude limits

Increasing the number of radial electrodes resulted in a reduced electrode surface area. This in-turn lowered the theoretical stimulation amplitude that could be safely delivered through each electrode to neural tissue. More precisely, as the number of radial electrodes was increased both charge storage capacity and charge injection constraints limited the safe stimulation amplitude. This relationship followed an exponentially decaying trend (Figure 4). Charge injection constraints limited stimulation amplitude for leads with five or fewer radial electrodes with an electrode height of 1.5 mm. Charge storage capacity limited the stimulation amplitude for leads with more than five radial electrodes and electrode height of 1.5 mm. As electrode height was decreased, the intersection of the two lines: charge storage capacity constrained amplitude and charge injection constrained amplitude was shifted left, toward a smaller number of radial electrodes. Charge storage capacity was found to be the limiting factor for all DBSAs with an electrode height of 0.5 mm. In accordance with the inclusion of surface area in Equations 21 and 22, stimulation amplitude limited by charge storage capacity was proportional to the electrode height, while stimulation amplitude limited by charge injection was proportional to the square root of electrode height. Most electrode designs (23/27) were limited to stimulation amplitudes below 10 mA per electrode, while approximately half (13/27) were limited to amplitudes below 5 mA using the 150 $\mu C/cm^2$ and $k = 2.0$ limits. All DBSA designs with an electrode height of 0.5 mm were limited to amplitudes below 5 mA per electrode.

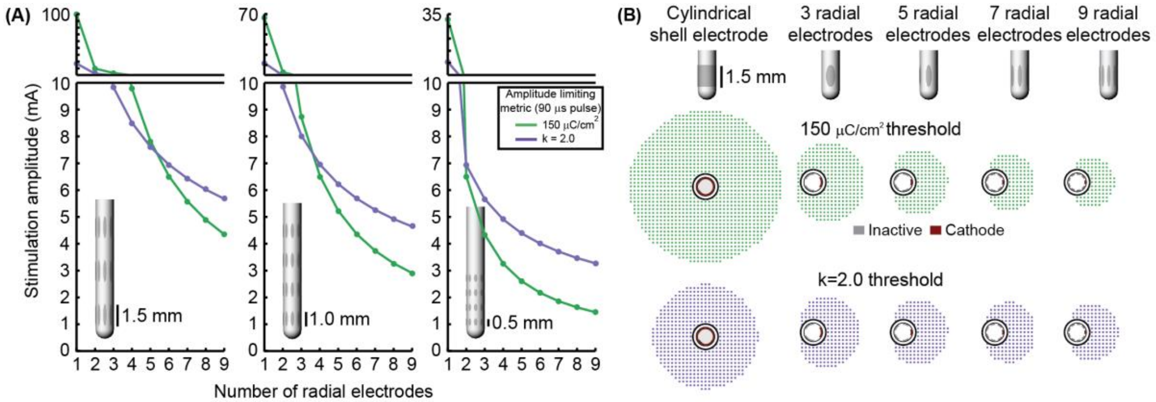

Figure 4. Stimulation amplitude limits. Maximum stimulation amplitude (for a biphasic waveform with a 90 µs initial pulse) was calculated for each lead design using a charge storage capacity of 150 µC/cm^2 and a safety factor limit of k = 2.0 (A). RoAs resulting from stimulation amplitude limits for several example DBSA lead designs (B).

2.4.2. *Steering, shifting and sculpting activation with single-cathode monopolar DBS*

Lateral shift, angular shift, and aspect ratio were used to evaluate the ability of each lead to shift, steer, and sculpt a RoA using monopolar stimulation within the range of 1–5 mA. Lateral shift for cylindrical shell electrodes did not significantly vary from zero as they produced a radially symmetric RoA. For all DBSA lead designs, at 1 mA, lateral shift increased from 0 mm to ~1.1 mm, regardless of the number of radial electrodes (Figure 1) or electrode height. Lateral shift increased moderately from 1.1 mm to 1.3 mm with stimulation amplitude increasing beyond 1 mA for all DBSA lead designs. Aspect ratio increased with stimulation amplitude at a similar rate for DBSA lead designs with the same electrode height (Figure 5). Electrodes with shorter heights were found to produce a slightly more circular RoA resulting in an aspect ratio closer to 1. For instance, the mean aspect ratio at 1 and 5 mA increased from 0.48 and 0.63 for DBSAs with 1.5 mm electrodes to 0.51 and 0.65 for DBSAs with 0.5 mm electrodes.

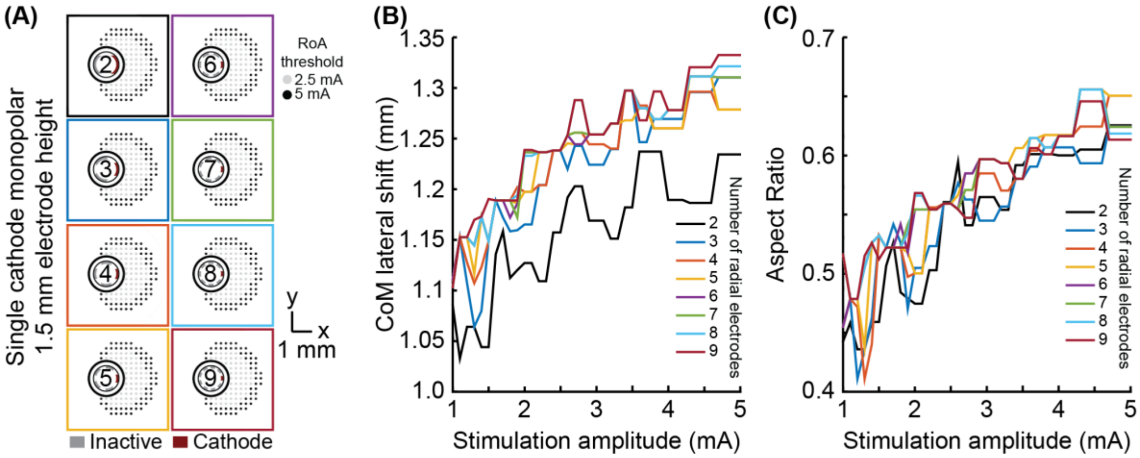

Figure 5. Monopolar single-cathode lateral shift and aspect ratio. RoA lateral shift and aspect ratio for monopolar single-cathode stimulation using DBSA lead designs with 1.5 mm electrode height within the range of 1–5 mA. Similar RoAs were produced from all DBSA designs (A). As stimulation amplitude was increased, lateral shift and aspect ratio both increased at similar rates (B,C).

Angular shift varied in accordance with angular separation of electrodes (Figure 6). For example, the six radial electrode lead incorporated electrodes separated by 60° and the RoA CoM angular shift resulting from stimulation through neighboring contacts was calculated to be 60°. Angular shift did not vary for leads with different electrode height nor did it vary with stimulation amplitude.

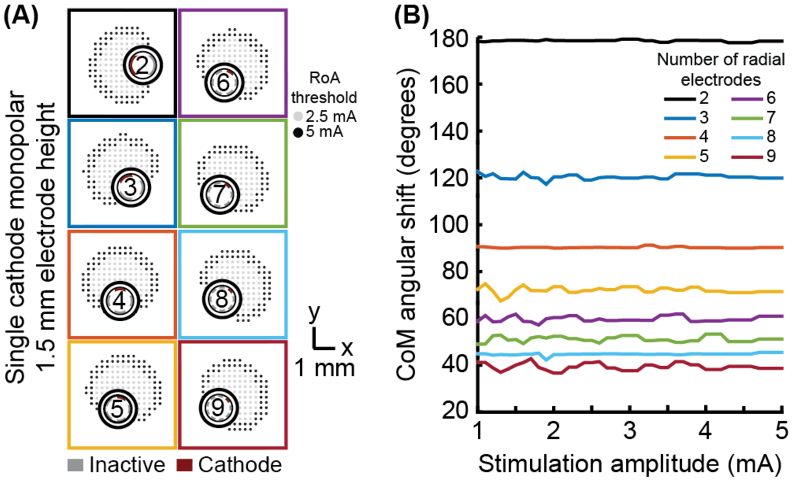

Figure 6. Monopolar single-cathode steering. Angular shift for monopolar single-cathode stimulation using DBSA lead designs with 1.5 mm electrode height within the range of 1 to 5 mA. DBSA leads with more electrodes were capable of finer RoA CoM angular shifting (A) in accordance with electrode angular separation (B).

None of the stimulation configurations tested resulted in complete coverage of a rotated target region without moderate to large overspill (Figure 7). The dual cathode configuration performed the best overall. The angular shift for this configuration was closest to 45° and target coverage was highest with the lowest spillover.

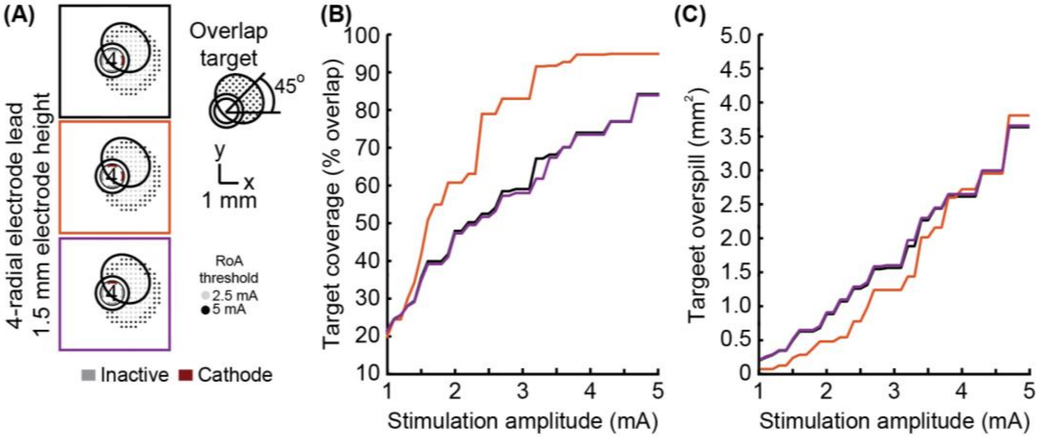

Figure 7. Steering toward an offset target region. Steering activation toward a target region between electrodes was investigated using DBSA–e4–h1.5 with single-cathode and multi-cathode stimulation configurations (A). The multi-cathode configuration performed best with a 45° angular shift (B) and exhibited the largest overlap and smallest overspill for any given stimulation amplitude (C).

2.4.3. Shifting and sculpting activation with multi-cathode monopolar DBS

For each DBSA lead design, uniform multi-cathode stimulation using a larger proportion of available radial electrodes enabled shifting of the RoA CoM from 0, lead-center, to ~1.3 mm in the direction of the primary cathode. The resolution with which RoA CoM could be shifted from one extreme to the other increased as the number of radial electrodes increased (Figure 8). Lateral shift increased slightly for larger stimulation amplitudes and did not change with electrode height. Increasing the proportion of active electrodes first decreased then increased aspect ratio for leads with more than four radial electrodes. The initial decrease in aspect ratio was a result of added cathodes facing the same direction as the center-most cathode. In general, increasing the proportion of active electrodes increased the aspect ratio toward one, indicating a more radially uniform RoA. These trends were found to be consistent for DBSA lead designs with different electrode heights.

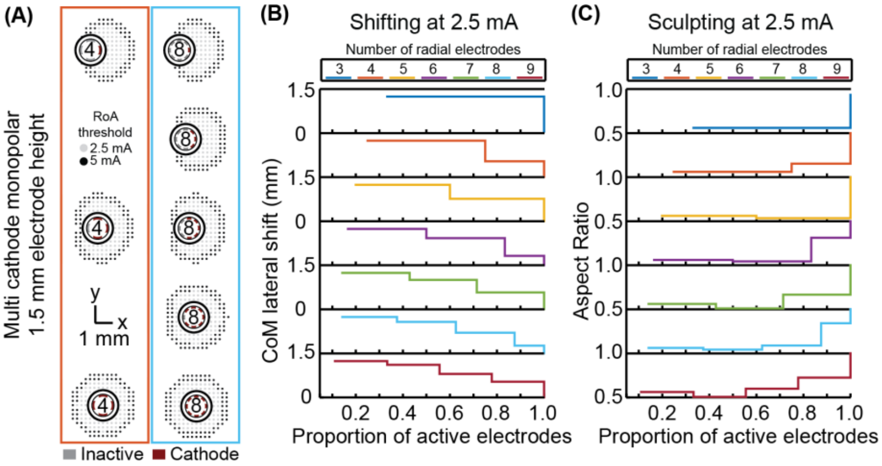

Figure 8. Incremental CoM shifting using monopolar multi-cathode stimulation. Monopolar stimulation currents were uniformly split across an increasing number of radial electrodes for each DBSA (A). DBSAs with more radial electrodes enabled shifting within the same range but at improved resolution (B). Aspect ratio decreased initially for DBSAs with more than 4-radial electrodes and increased from ~0.5 to 1 as the proportion of active electrodes increased (C).

Non-uniform multi-cathode stimulation enabled RoA CoM shifting within the same range as uniform current shifting, but with improvement in shifting resolution (Figure 8). Shifting resolution approximately doubled non-uniform multi-cathode stimulation using DBSA–e4–h1.5 in comparison to uniform multi-cathode stimulation using DBSA–e8–h1.5. The aspect ratio range was approximately the same for uniform and non-uniform multi-cathode stimulation; however, the aspect ratio profile shifted to the left indicating that the non-uniform multi-cathode stimulation produced more circular RoAs (Figure 9).

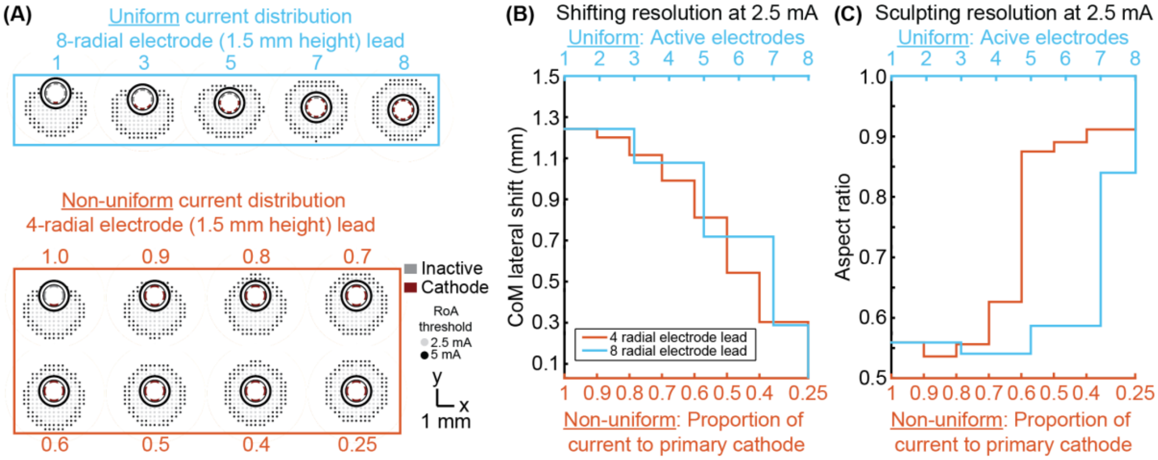

Figure 9. Multi-cathode, non-uniform current shifting of the CoM. Monopolar stimulation currents uniformly split across an increasing number of radial electrodes

using DBSA–e8–h1.5 compared to monopolar stimulation non-uniformly split across electrodes using DBSA–e4–h1.5 (A). Non-uniform configurations using DBSA–e4–h1.5 resulted in improved shifting resolution in comparison to uniform configurations using DBSA–e8–h1.5 (B). Aspect ratio profile was similar for the two strategies but was shifted for non-uniform current shifting indicating more circular RoAs were generated from non-uniform shifting (C).

2.4.4. Classification

Cross validation using 10 folds was performed using three feature sets in combination with five machine learning algorithms. In general, high mean classification accuracy was achieved with low standard error across the 10 folds. The random forest classification algorithm, which involves automated feature selection, performed best, achieving perfect classification using any of the three feature sets (Figure 10). Of the remaining classifiers where no feature selection/reduction was performed: the neural network classifier achieved perfect accuracy and the naïve Bayes classifier achieved accuracy above 0.95 using the RPFS. Classification using the RPFS produced the highest accuracy for all except in the case of the k-nearest neighbors classifier. The LPFS and 7 HuIM feature set achieved similar accuracy when used in combination with the neural network, naïve Bayes and k-Nearest neighbors classifiers.

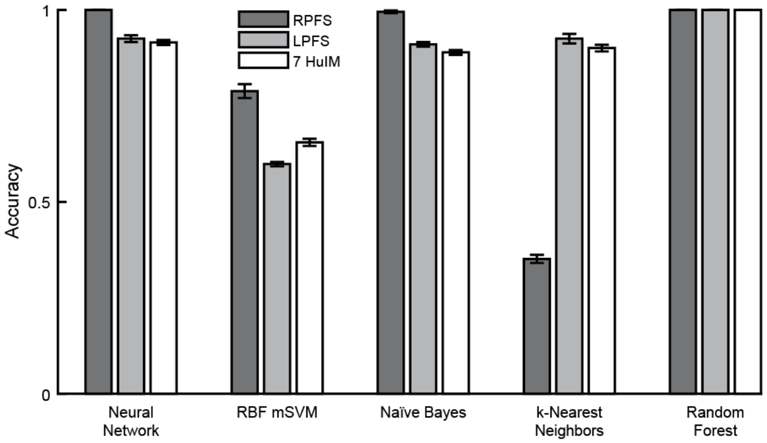

Figure 10. Classification accuracy. Mean classification accuracy and accuracy standard error (represented by error bars) were calculated for each classifier/feature set combination across 10-folds. Perfect classification of monopolar stimulation settings was achieved with the random forest classifier using any of the three feature sets. The neural network, naïve Bayes and random forest classifiers achieved perfect or near perfect accuracy using the region properties feature set.

2.4.5. Feature importance

Sequential forward selection and results from the random forest classification algorithm were used to evaluate feature importance. Mean accuracy was calculated as an indicator of feature importance at each stage of the forward selection for both the neural network and naïve Bayes classifiers. From the random forest algorithm, mean effect on prediction error resulting from random permutation of each feature across the out-of-bag samples was used as an indicator of feature importance. A low standard error was calculated for all indicators of feature importance. Using either the neural network or naïve Bayes classifier, mean accuracy converged to one after the addition of the same four features: CoM x-coordinate, CoM y-coordinate, ellipse fit eccentricity and ellipse fit orientation. These same four features were ranked as the most important by the random forest algorithm (Figure 11). Although all features were included in the analysis, forward selection using the neural network and naïve Bayes classifiers resulted in the most important features being from only the RPFS.

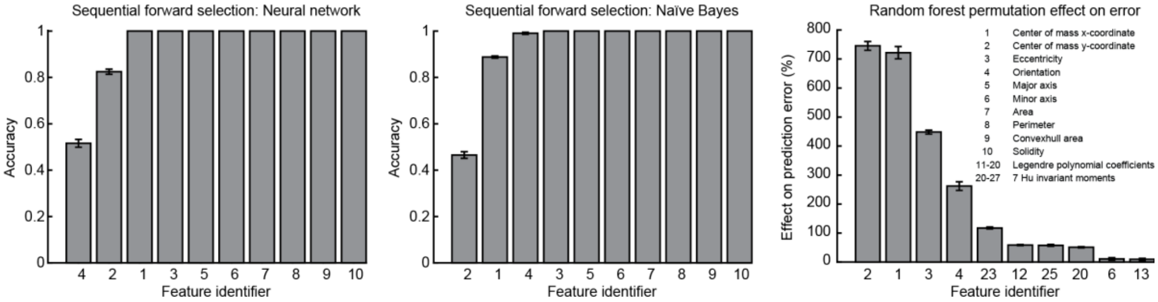

Figure 11. Feature importance. Sequential forward selection accuracy converged to one after the addition of features 1, 2, and 4 using both the neural network and naïve Bayes classifiers. From the random forest algorithm, the effect on classification error was increased most by the random permutation of features 1, 2, 3, and 4. Features 1: CoM x-coordinate, 2: CoM y-coordinate, and 4: ellipse fit orientation were found to be the most important features and using only these three features in combination with the neural network and naïve Bayes classifiers enabled perfect classification.

2.5. Discussion

While DBS therapy is often successful in managing the symptoms of a range of medication-refractory brain disorders, the spatial precision with which the therapy can be delivered using a conventional lead with cylindrical shell electrodes can be limiting for cases of slight neurosurgical targeting error or for brain regions with complex morphologies. Previous studies have developed methodologies to steer and direct activation volumes along a DBS lead studies [30–33,85], but less is known about programming stimulation settings around a DBS lead [101]. The results of this study show for a DBS lead embedded within or near a fiber tract that: (1) four ellipsoidal electrodes around a DBS lead provided good flexibility to steer, sculpt, and shift a region of neural activation without exceeding the charge storage capacity of platinum-iridium electrodes or charge injection limits for neural tissue, and (2) a small feature set, including only three geometric features representing a target region enabled robust machine learning classification of electrode stimulation configuration.

2.5.1. DBS array design considerations

Microfabrication processes enable new opportunities to develop stimulating probe technology with many more electrode sites than what is currently in clinical use for DBS applications [101,133,134]. Increasing the number of electrodes and in turn decreasing the size of electrodes has several important effects on the region of neural tissue including limiting the spatial extent of the RoA due to charge storage capacity and charge injection limits [30,125]. Previous preclinical studies in animal models of neurological disorders have also noted that DBS therapy is partially based on modulating the neuronal firing patterns of a fairly large volume of tissue [98,99] within a target volume [29]. Thus, while increasing the number of electrodes may provide more spatially focused stimulation, generating a therapeutic effect through DBS arrays is likely to require grouping electrodes together for high-density DBS arrays. This grouping approach would be complicated by radial diffusion properties that result in higher charge densities near the edges of each electrode in a group [30,118].

In this study, we extend these results showing that charge storage capacity and charge injection are limiting factors, though to different extents as the number of radially electrodes is increased. For DBSA designs with small electrode surface areas, advanced electrode coatings [126,135,136] may address the issue of charge storage capacity, but the charge injection limits will remain an issue as was shown for DBSA lead designs with five or more radial electrodes. Elliptical electrodes with height ranging from 0.5 to 1.5

mm and width ranging from 0.2 to 0.9 mm were used in this study. For electrodes with the largest height and the smallest width, it is possible that these highly eccentric electrodes would have higher charge density values at the ends of the electrode major axis [137] similar to how large current density values are found at the corners of rectangular electrodes [30].

2.5.2. Shaping the region of activation

One of the primary motivations for advances in DBS lead and stimulator designs is to enable compensation for sub-optimally placed leads. Ideally, leads with cylindrical shell electrodes are implanted with one of the electrodes at the geometric center of the neural target enabling good stimulation coverage with minimal overspill. With targets that are several centimeters deep and only millimeters across, precise lead placement can be challenging. With a cylindrical shell electrode, a small offset in the final lead location may significantly limit stimulation efficacy and result in stimulation induced side effects resulting from activation of nearby pathways. DBSAs have been proposed as able to compensate for such placement issues [101,110,112]. As we have shown, monopolar stimulation through a single radial electrode resulted in a 1–1.3 mm RoA CoM lateral shift and increasing stimulation amplitude minimally affected the CoM location. Additional radial electrodes or proportional current steering provided options to incrementally shift the RoA CoM with sub-millimeter resolution, but in cases where more than a 1 mm shift in the RoA CoM is needed for compensation of lead misplacement, this need would not be adequately addressed by any of the DBSA designs evaluated in this study. The results showed that uniform multi-cathode stimulation enabled incremental CoM shifting, but was limited by the number of available radial electrodes. Non-uniform multi-cathode stimulation resulted in better shifting resolution with four radial electrodes than could be achieved using uniform multi-cathode stimulation with eight radial electrodes. From this we conclude that fewer electrodes does not limit shifting if non-uniform stimulation strategies are used. However, practical implementation of non-uniform stimulation requires fine and independent control of multiple stimulation channels. In regard to lead design, leads with fewer radial electrodes may be preferable because of larger electrode surface areas and possibly less complex manufacturing processes. In regard to implantable pulse generator design, fewer independent current sources may be preferable to allow for device miniaturization.

Stimulators with independent current-regulated channels are well-established in the fields of spinal cord stimulation for pain mediation [138], auditory nerve stimulation for hearing restoration [139], and retinal stimulation for vision restoration [107]. The advent of stimulators with independent channels in these fields have prompted significant research into the utility of various stimulation strategies for directing and focusing current, particularly in the case of auditory nerve stimulation, where highly conductive fluid separates the stimulating electrodes from the stimulation target [140]. Strategies for steering and focusing stimulation include the use of multiple sources to steer a region of neural activation and the use of bipolar stimulation to narrowly focus current [106,141]. These strategies have been implemented with varying degrees of success for cochlear implants and spinal cord stimulation. These strategies have also been investigated in DBS systems via modeling studies [31,85] and clinical studies [32,33] for the purpose of steering neural activation along the length of a conventional DBS lead. Our results indicate that for steering, shifting, and sculpting of neural activation around the lead, a DBSA with four electrodes per row combined with a pulse generator that has independent current sources for each electrode would be highly effective at steering and shifting a region of neural activation around a DBSA lead. Our results also indicate that more than four electrodes would be minimally advantageous.

Radial shifting and steering have potential to benefit clinical outcomes for a number of DBS targets [142]. For instance, the subthalamic nucleus target for Parkinson's disease is adjacent to the corticospinal tract of internal capsule [31] and non-motor territories of the subthalamic nucleus [67] that when stimulated can lead to adverse side effects. The ventral intermediate nucleus of thalamus, which is the primary target for treating Essential Tremor, is adjacent to the internal capsule, the somatosensory nucleus of thalamus, and non-motor pathways involved in language and cognition [143]. Similarly, the pedunculopontine tegmental area is replete with adjacent fibers of passage including the superior cerebellar peduncle, medial and lateral lemnisci, and the central tegmental tract among others that may have confounding effects on treatment of medication-refractory gait disorders [87]. Radial current shifting and steering may also have important applications to DBS targets that are embedded within fiber tracts including those for depression [144], obsessive compulsive disorder [145], and memory disorders [12].

2.5.3. Machine learning to facilitate programming

Along with greater flexibility in directing neural activation, DBS arrays present exponentially more options during programming. This necessitates the use of (1) guided programming through computational algorithms [114,115], and (2) empirical algorithms that rely on the spatial distribution of electrophysiological biomarkers [146]. Here, we investigated feature sets to be used in building machine learning classifiers for predicting DBSA stimulation settings. These feature sets were constructed from the two-dimensional computational modeling results of axonal activation using the DBSA–e4–h1.5 lead and relied upon computer vision feature extraction techniques. In computer vision, feature extraction is commonly performed to identify objects that may be "viewed" by a machine using images or video that was captured and processed internally. Robust computer vision identification requires that objects be identifiable when viewed at different distances, angles, and locations within the field of view requiring the use of scale, rotation, and translation invariant feature sets [130]. The feature sets we have designed for use in machine learning classifiers for DBS rely on these same principles, but include a center of mass estimate that is relative to the lead-center so that changes in the RoA direction and shift may be detected. In addition to investigating the value of various features for such classification algorithms, we have demonstrated robust machine learning classification of electrode stimulation configuration using a single row of electrodes. Our investigation into feature sets revealed that excellent classification could be achieved using a small number of two dimensional geometric features that may be readily translated in three-dimensional geometric measures. Running axon model simulations, feature extraction, and classifier training required significant computation time, but the resulting five classification algorithms were able to be deployed in less than 1 min using a conventional desktop computer. The speed with which such algorithms can be deployed demonstrates the power and practicality of such algorithms for use in clinical DBS programming.

2.5.4. Limitations

The quasistatic finite element models used for predicting tissue voltage in this study were idealized as isotropic and were homogeneous within bulk neural tissue. Increasingly complex models that more precisely model tissue conductivity using diffusion weighted imaging have been introduced in the past decade and have been shown to impact biophysical simulation results [29,147,148], particularly for modeling of electrical stimulation near white matter fiber tracts [29,149]. Further, the conductance values utilized in the tissue models presented here rely on experimentally determined values for conductance that are subject to uncertainty as evident by the range of values reported within the scientific literature [82,150]. Variations of tissue conductance within the range of reported values have been shown to lead to significant uncertainty in the activation predictions of biophysical models [151]. Additionally, stimulus waveforms propagating through encapsulation and brain tissue are likely to be influenced reactive tissue impedances [152–155] and the quasistatic model does not incorporate this feature. Using the modeling framework presented here, future work may assess the impact of variations in conductance, brain anisotropy, and reactive tissue response on the DBSA design and feature selection for model based programing algorithms.

The multi-compartment axon models used in this study were idealized straight cables coursing parallel to the DBS lead. Modeling work with straight axons has potential utility for DBS targets that are within or near large fiber tracts that have minimal curvature [12,144,145,156]. However, it is important to consider that this idealized model geometry lacks the anatomical trajectories known to occur in many targets of DBS. In these cases, factors such as stimulating regions with networks of cellular and axonal processes [87], inducing complex cellular entrainment patterns [7,157], and increasing the likelihood of axonal conduction failure due to axonal branching [158], lack of myelination [159], and synaptic fatigue [160] should be considered.

Elimination of the ETI from the finite element models relied on a subset of simulations that incorporated an ETI equivalent circuit model that assumed the electrode material was platinum-iridium. To avoid exceeding the charge storage capacity of the electrodes with a clinically acceptable factor of safety, realistic lead designs with small electrodes would likely require the use of coatings such as iridium oxide [126], PEDOT [161], or TiN [162] for which lumped ETI equivalent circuit model values would likely differ.

2.6. Conclusions

DBS arrays with radially distributed electrodes have potential to improve patient outcomes by enhancing the flexibility of directing stimulation around an implanted DBS lead. Clinical DBS leads with cylindrical shell electrodes do not exceed electrode charge storage capacity or charge injection limits due to the large surface area and existing voltage or current compliances of current implantable pulse generators. However, segmenting the cylindrical shell electrode design into two or more electrodes around the lead circumference would bring these stimulation limits into consideration. For DBSAs, monopolar single-cathode stimulation was useful for shifting the RoA CoM from lead-center to 1.3 mm in the direction of the stimulating electrode. Shifting resolution on the scale of 0.1 mm was achievable with four radial electrodes using non-uniform distribution of current, suggesting a higher density DBSAs would not be needed to achieve clinically relevant RoA shifting if independent current sources are utilized. A simple feature set consisting of the RoA center of mass and orientation enabled robust machine learning classification with accuracy equal to 1 for a range of monopolar stimulation settings.

2.7.Acknowledgements

We thank the Minnesota Supercomputing Institute (MSI) for providing computational resources. This study was supported by funding from the Michael J Fox Foundation, the University of Minnesota MnDRIVE (Minnesota's Discovery, Research and Innovation Economy) initiative, NIH R01-NS081118, NSF-IGERT (Systems Neuroengineering, DGE-1069104), and NSF-GRFP (00006595 to BT).

3. Evaluation and analysis of personalized computational models of DBS

Teplitzky BA, Johnson LA, Zhang S, Zitella LM, Patriat R., Nebeck S, Connolly AT, Yacoub E, Adriany G, Harel N, Vitek JL, Johnson, MD. Evaluation and analysis of factors contributing to variance in computational models deep brain stimulation. *In Preparation.*

3.1.Overview

3.1.1. Objective

The goal of this study was to validate predictions from a series of computational models using *in vivo* electrophysiological recordings and behavioral assessment during deep brain stimulation of the globus pallidus internus.

3.1.2. Approach

Stimulation thresholds for evoking motor contractions during globus pallidus internus deep brain stimulation were evaluated in two non-human primates, one with a miniaturized DBS lead and one with a DBS array. In the subject with the DBS array, cortical recordings were used to generate a prediction of percent activation within the arm representation of the corticospinal tract. Subject-specific computational models using the scaled eigenvalue, the volume constraint, and the normalized volume constraint methods to represent tissue conductivity were constructed and used to predict activation within the arm representation of the corticospinal tract. Model results using the three different methods were compared to motor contraction thresholds and, in one subject, compared to stimulation induced cellular activation measured in motor cortex.

3.1.3. Main Results

Stimulation induced activation in motor cortex at the motor contraction threshold amplitude was measured within the range of 8-16% for distal electrodes and 0% for most proximal electrodes. Motor contractions were able to be induced using all electrodes, but higher stimulation amplitudes were required for increasingly proximal electrodes. In comparison to motor contraction thresholds, model predictions using the DBS array strongly over predicted the degree of directional steering. Error between model predictions and motor cortex recordings was lowest for models that relied on the normalized volume constraint and was largest for models that relied on the scaled eigenvalue method.

3.1.4. Significance

The finding that the normalized volume constraint method for modeling brain tissue conductivity generated model predictions that best align with experimental data has important implications for the DBS modeling community, which has in the past relied primarily on the scaled eigenvalue method for modeling brain tissue conductivity. Additionally, the misalignment between behavioral outcomes and model predictions suggests that more comprehensive and anatomically correct representations of model cell distributions may be required to generate clinically relevant model outcomes.

3.2.Background

The clinical success of deep brain stimulation (DBS) therapy largely depends on the accuracy of DBS lead implantation and the degree to which stimulation settings can be adjusted without eliciting adverse side effects. Computational models of DBS that integrate both predictions of the induced electric field in brain tissue and predictions of biophysical neuron responses to electric fields [122] have provided notable successes in advancing DBS therapy. These models have supported (1) studies investigating the therapeutic mechanisms of DBS in preclinical animal models [99,163,164] and in humans [8,65,68,144,165] (2) development of neurosurgical planning software [69], (3) retrospective identification of neural pathways underlying side effects of DBS [66,67], (4) prospective approaches to optimize stimulation settings on an individual basis [114,115], and designing and evaluating novel DBS lead and stimulation technology [70–72]. While such modeling efforts rely on bioelectric principles and assumptions that have been characterized in part *in vivo* [66,86], the overall modeling framework has yet to undergo rigorous behavioral and electrophysiological validation.

To date, the most advanced models of DBS attempt to accurately incorporate *subject-specific* brain anatomy at submillimeter resolution using high-field magnetic resonance imaging [148]. Such imaging approaches provide important context for constructing inhomogeneous and anisotropic conductivity maps of brain tissue as well as morphological rendering of fiber tracts within the brain using diffusion weighted imaging [166–169]. Finite element models incorporating these conductivity maps in the context of a subject's DBS lead implant(s) are then integrated with multi-compartment equivalent circuit models of neurons and fiber tracts. This framework thus facilitates predicting transmembrane currents imposed by stimulation [93,94,170,171] and whether or not those perturbations result in stimulation-induced action potential generation or other modulation of ongoing neuronal activity [8,172].

Quantification of the population response to stimulation is generally made using either a VTA or an activation profile curve. VTAs specific to an electrode or stimulation waveform can be created and overlaid onto medical imaging to visualize brain regions that may be modulated by different stimulation configurations. An activation profile represents a percent of neurons activated within a specific fiber tract or brain region by a particular stimulation configuration. Percent activation can be a useful measure for optimizing stimulation parameters, particularly in situations where side-effect regions cannot be completely avoided. Because of their complexity, many parameters contribute to the predictions from these models and although individual aspects of these models have been examined, such as the FEA tissue voltage predictions in the subthalamic nucleus area and thalamus [86], the VTA and activation profile approaches have yet to be rigorously validated.

The goal of this study was to evaluate computational model predictions by comparing activation profiles from various tissue conductivity maps to *in vivo* electrophysiological recordings and behavioral assessments in the context of globus pallidus internus (GPi) deep brain stimulation leads. Two non-human primates were chronically implanted with either a DBS lead consisting of eight stacked cylindrical electrodes [99] or a radially segmented deep brain stimulation array (DBSA) [134]. In both cases, stimulation was delivered at amplitudes above and below the threshold for evoking muscle contractions resulting from putative activation of the adjacent corticospinal tract (CST) of the internal capsule (IC). The choice of the GPi target, as opposed to the subthalamic nucleus (STN) for example, was motivated by the fact that the GPi (unlike the STN) does not have direct projections two or from the cortex. In one primate, single cell recordings in the arm representation of motor cortex ($M1_{arm}$) were acquired during stimulation using a 100-channel microelectrode array. Cortical recordings were analyzed in order to identify stimulation induced antidromic activity, from which a percent activation of the arm representation within internal capsule was inferred. Additionally, subject-specific computational models of DBS were generated for each primate in order to compare predictions to muscle contraction thresholds (both subjects) and $M1_{arm}$ recordings (one subject).

3.3.Methods

3.3.1. Experimental procedure

3.3.1.1.Subjects

Two rhesus macaque monkeys, *macaca mulatta*, were subjects in this study: Monkey N (18 year old female, naïve) and Monkey J (15 year old female, rendered parkinsonian with the neurotoxin 1-methyl-4-phenyl-1,2,3,6 tetrahydropyridine, MPTP [157]). Both animals took part in other parallel studies and the modeling results were retrospective in context. All procedures were performed in compliance with the United States Public Health Service policy on the humane care and use of laboratory animals, and were approved by the University of Minnesota Institutional Animal Care and Use Committee.

3.3.1.2.Preoperative imaging

Preoperative MRI was acquired using a passively shielded 7 Tesla magnet (Magnex Scientific) at the University of Minnesota Center for Magnetic Resonance Research. Subjects were anesthetized with Isoflurane (2.5%) and monitored for depth of anesthesia during imaging sessions. Imaging acquisition included computed tomography (CT), T1-weighted imaging (T1-W), T2-weighted imaging (T2-W), susceptibility-weighted imaging (SWI), and diffusion-weighted imaging (DWI) (Table 3). SWI was acquired with a 3D flow-compensated gradient echo sequence.

Table 3. Subject and imaging sequence information (iso: isometric).

Subject	Sex	Age (years)	Anatomical imaging			Diffusion weighted imaging			
			T1-W (mm^3)	T2-W (mm^3)	SWI (mm^3)	b-value (s/mm^2)	# of directions	FOV (mm^3)	Resolution (mm^3)
J	F	15	0.469×0.469 ×0.5	0.357×0.357 ×0.8	0.4 iso	1500	132	144×88× 50	1.1 iso
N	F	18	0.469×0.469 ×0.5	0.5 iso	0.4 iso	1500	110	144×88× 50	1.1 iso

3.3.1.3.DBS chamber placement

Microelectrode mapping of the brain and DBS lead implantation were guided using surgically implanted chambers. A coordinate system was established using the surgical planning software, Cicerone (Miocinovic et al., 2007), by co-registering preoperative CT of the cranium and anatomical MRI of the brain in AC-PC space. The zero coordinate in AC-PC space was defined as the midpoint of an imagined line in the brain's sagittal plane connecting the anterior and posterior commissure tracts. Coordinates for the chamber implant location were determined by aligning the central axis of chamber with the GPi. Chambers and head restraints were implanted during an aseptic surgical procedure as described previously [99,174]. Briefly, craniotomies were made under stereotactic guidance leaving the underlying dura intact, and cephalic recording chambers were secured in place using a combination of surgical bone screws and dental acrylic. Subject J was implanted with one chamber oriented along the parasagittal plane at an anterior angle of 38 degrees to target the GPi. Subject N was implanted with a chamber oriented along the coronal plane at a lateral angle of 32 degrees, with the latter used for targeting the sensorimotor external and internal segments of globus pallidus.

3.3.1.4.Mapping, lead implantation, and postop imaging

Microelectrode mapping of the brain was used to determine the precise lead implant location using techniques similar to those using in human functional neurosurgery [175]. The borders of the GPi were mapped in each subject by recording cell activity using tungsten microelectrodes that were advanced through uniformly spaced grid sections in the cephalic chambers (Narishige Scientific Instruments). The GPi and subregions within the GPi were identified by their characteristic firing patterns in response to sensorimotor manipulation [176]. Microstimulation (10–100 μA) was used to identify the corticospinal tract of IC. Once the boundaries of the GP were established and sensorimotor territory identified, a final recording track was performed to determine the target depth for lead implantation. The tungsten microelectrode was then removed and the DBS lead was implanted to the target depth using an insertion cannula (Subject J) or stylet (Subject N). Subject J was implanted with a 0.625 mm diameter eight electrode lead (NuMED, Hopkinton, NY). Each cylindrical shell electrode was 0.625 mm in diameter, 0.5 mm tall, and separated by 0.5 mm (Figure 12, top left). Electrode contacts were labeled 0 (distal) through 7 (proximal). Subject N was implanted with a 0.6 mm diameter 32 electrode DBSA [134] (Figure 12, bottom left). DBSA electrodes were arranged with eight rows distributed along the length of the lead and separated by 0.28 mm. Each row consisted of four columns separated by 90 degrees. Each electrode was elliptical (0.36 x 0.47 mm) with the major axis aligned with the length of the lead body. The final lead location was verified using post-operative CT, which was acquired approximately one week after the lead implant procedure and co-registered to preoperative MRI (Figure 13).

In a separate surgical procedure after DBS implantation, the right hemispheric arm representation in primary motor cortex ($M1_{arm}$) of Subject J was implanted with a 96-channel Utah microelectrode array (Figure 12, right) (Pt-Ir, 1.5 mm depth, 0.4 mm inter-electrode spacing, Blackrock Microsystems) using methods described previously [177,178]. M1 was identified by sulcal landmarks (i.e. central sulcus, arcuate sulcus and precentral dimple) and the arm representation was identified through intra-operative stimulation of the cortical surface using a stainless steel ball electrode (Grass Technologies Corporation).

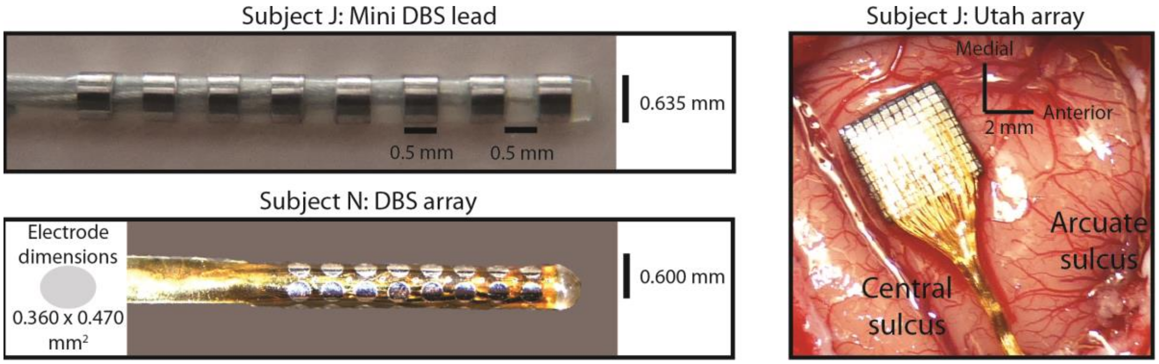

Figure 12. Stimulation and recoding implants. Subject J was implanted with an eight cylindrical electrode DBS lead (top left) and a 96-channel Utah microelectrode array (right). Subject N was implanted with a 32 ellipsoidal electrode DBS array (bottom left).

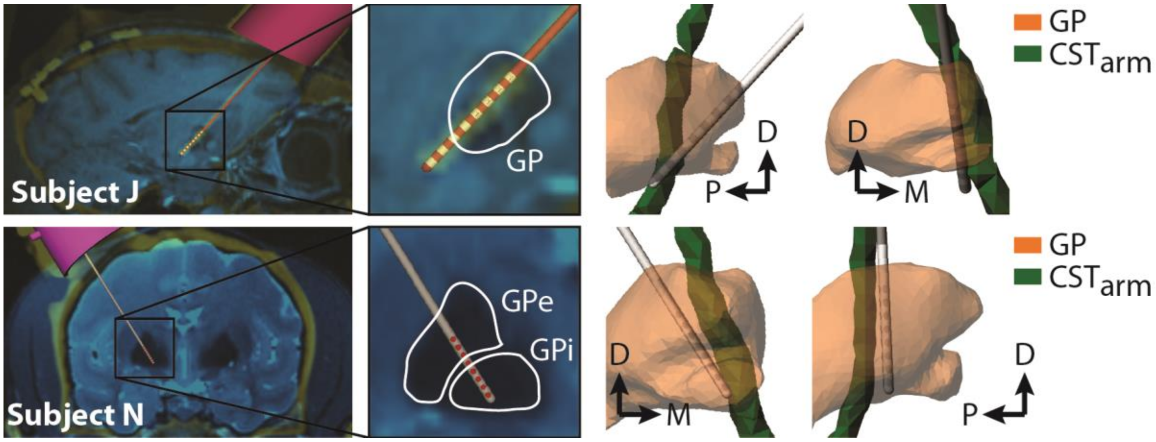

Figure 13. Image co-registration and model lead placement. Preoperative MRI was co-registered with postoperative CT in order to confirm the location of the implanted lead (left). The lead, the globus pallidus (GP), and the arm representation within the corticospinal tract (CST$_{arm}$) were constructed for each subject (right).

3.3.1.5.Assessment of thresholds for stimulation-induced motor contractions

Subjects were trained to allow passive manipulation of the limbs using positive reinforcement techniques. Stimulation pulse trains were delivered through each electrode at varying amplitudes in order to determine electrode-specific stimulation thresholds for inducing involuntary motor contractions in each subject. Current-regulated charge-balanced waveforms were delivered using an external waveform generator and a current isolator (Subject J: IZ2H, Tucker Davis Technologies; Subject N: S88X, Grass Instruments with a Model 2200, A-M Systems,). Two slightly different stimulation trains were used for the two subjects. For Subject J, the stimulation pulse consisted of an 80 μsec cathodic pulse followed immediately by an anodic pulse with equal width and amplitude. In Subject N, the stimulation pulse was a 90 μsec cathodic pulse followed by a 20 μsec interstimulus interval and then a 90 μsec anodic pulse with equal magnitude to the initial cathodic pulse. Both subjects received monopolar stimulation with the cranial chamber serving as the return electrode. Stimulation thresholds for evoking motor contractions were determined in a blinded manner such that the observing researcher was unaware of the stimulation settings while evaluating the presence of involuntary muscle contractions. For Subject N, motor contraction thresholds were collected using 16 electrode configurations. Each configuration included two impedance matched electrodes in the same column that were electrically shorted such that stimulation was delivered simultaneously through both electrodes. In Subject J, stimulation was delivered using electrodes 0 (distal) through 5 (proximal).

3.3.1.6.Quantification of electrophysiological recordings

In Subject J, electrophysiological recordings were collected from the $M1_{arm}$ microelectrode array a TDT workstation (RZ2 DSP, PZ5 Neurodigitizer, Tucker Davis Technologies), with both recording and stimulation operating on the same ~25 kHz sample clock. The cortical microelectrode recordings were acquired for DBS amplitudes approximately 75%, 100%, and 125% of the motor contraction stimulation amplitude threshold for each electrode. Cortical recording trials consisted of a baseline off-DBS period (~30 sec in duration), followed by an on-DBS block at each of the three stimulation amplitudes. Each block consisted of a 5 second stimulation period, followed by 5 seconds off stimulation, repeated 5 times. Raw data were filtered 0.5 Hz-12.5kHz and saved to hard disk for offline analysis. The following processing steps were performed for each of the 96 microelectrode array channels. First, a digital bandpass filter (300 Hz-3 kHz) was used to extract spike activity from the raw recording (Figure 14A). Second, DBS artifacts present in the recording were removed by a simple blanking procedure (Figure 14A). The preamplifier used had a large ±500 mV input range and artifacts did not cause saturation, so the artifact duration was brief (0.5-1 ms) and was removed by setting sample points during this period to zero. Third, spikes outside of background activity were identified in Offline Sorter (Plexon, Inc., Dallas, Texas, USA) based on a spike detection threshold set manually for each channel, ≥6 standard deviations below mean of the peak-heights histogram. Spike times typically reflected the activity of 1-3 cells and were saved for subsequent analysis. Recording channels with no clearly discernable cells outside the background (45 of 96 channels) were excluded. Finally, a peristimulus time histogram (PSTH, bin size = 0.2 msec) triggered to stimulation pulses was examined for each electrode configuration and stimulus amplitude and classified as putative antidromic based on whether short latency, low temporal jitter, high firing activity was detected following the DBS pulses (Figure 14B). The qualifier “putative” is used because classification is based solely on the PSTH, and collision experiments were not conducted to confirm that DBS-evoked activity was definitively antidromic. The firing rate in each PSTH bin was converted to a z-score relative to baseline firing rate bins taken from the off-DBS period, based on a PSTH triggered to virtual stimulation pulses. If there was a peak in the resulting PSTH with a maximum z-score >10, latency <3 msec, and low temporal jitter (width at half-max ≤3 bins), the stimulation evoked activity was classified as putative antidromic. This analysis is based in part on the assumption that neural recordings included activity from layer V pyramidal cells with axonal projections making up part of the internal capsule, which is not unreasonable given the electrode array depth of 1.5mm and the fact that putative antidromic activity was observed on many recording channels. The percentage of recording channels with putative antidromic activity was calculated (Figure 14C) and used for comparison to model predictions.

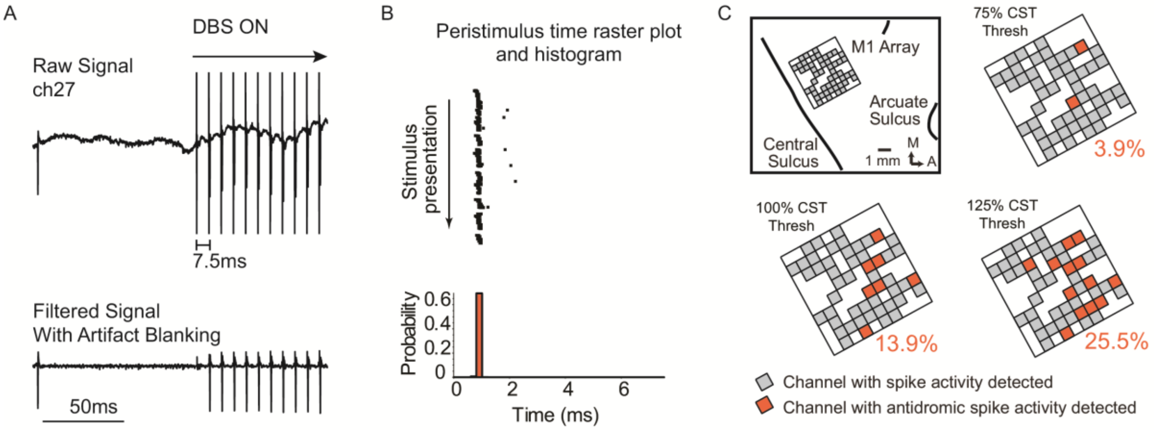

Figure 14. Antidromic activity detected in M1 during GP stimulation. (A) Example raw (top) and processed (bottom) signal from one of the channels on the 96 channel M1 microelectrode array, illustrating a putative antidromic firing in response to GP DBS. (B) Peristimulus time raster plots and histograms time locked to stimulation pulses (time = 0) were created for each recording channel and classified as antidromic or not as described in the Materials and Methods. (C) Illustration indicating the location of the M1 array on the cortical surface. Gray squares indicate channels with detectable single or multi-unit spiking activity (51/96 channels). For each stimulation configuration, neuronal responses to DBS at current levels of 75, 100, and 125% CST were characterized and the percentage of channels with antidromic responses was calculated. Additional plots show

channels with antidromic spike activity (orange) at each current level for the Monopolar C1 DBS configuration.

3.3.2. Computational modeling

Subject-specific computational models of DBS were constructed such that lead geometry, stimulation waveform, and stimulation configuration were consistent with those used during the assessment of stimulation induced muscle contractions in the two subjects. Each computational model included a finite element model of the brain and a population of multi-compartment axon cable models representing reconstructions of the arm representation within the corticospinal tract of internal capsule (CST_{arm}). Several versions of the finite element model were created in order to evaluate the effect of increased model complexity and different approaches for calculating anisotropic tissue conductivity maps.

3.3.2.1.Image registration, brain segmentation, and lead placement

Three-dimensional brain reconstructions and the placement of leads in each model were performed using co-registered pre- and postoperative subject imaging. A common coordinate system was established in DWI-space by aligning preoperative MRI and postoperative CT to the DWI dataset using Amira v6.0 (FEI, Hillsboro, OR). Digital representations of the implanted lead and chamber were aligned to the co-registered imaging data using Cicerone (Miocinovic et al., 2007) (Figure 15A). From the co-registered T1-W, T2-W, and SWI data, the brain white matter, gray matter, and the lateral ventricles were manually segmented using Mimics v15.0 (Materialise, Leuven, Belgium) (Figure 15B). Regions modeled as gray matter included the cortical and cerebellar gray matter, the basal ganglia, and thalamus. A digital representation of the chamber and lead were placed in reference to the co-registered postoperative CT data.

3.3.2.2.Tissue conductivity tensor maps

Subject specific tissue conductivity tensor maps were calculated using three approaches (Sections 3.3.2.2.1-3.3.2.2.3), each of which relied on diffusion tensors estimated from DWI (Figure 15C). Processing of the DWI was performed using FSL [179] and included eddy current correction using FDT [180], brain extraction using BET [180], estimation of diffusion parameters using BEDPOSTX [181], and fitting of the diffusion tensor model at each voxel using DTIFIT [181]. The diffusion tensor eigenvalues and eigenvectors calculated using DTIFIT were used in the calculation of the tissue conductivity tensors at respective voxels. The term, tissue conductivity tensor map, referred to the entire set of tissue conductivity tensors calculated at each DWI voxel for a single subject. At each voxel, a tissue conductivity tensor (Σ) was calculated from its eigendecomposition:

$$\Sigma = V\sigma V^T \tag{23}$$

where V is the matrix of tensor eigenvectors and σ is the diagonal matrix of conductivity tensor eigenvalues. Tissue conductivity tensor eigenvectors were assigned as equal to the diffusion tensor imaging eigenvectors [182]. In two of the approaches, isotropic conductivity and relative permittivity for gray and white matter were calculated using the Gabriel et al. Cole-Cole dispersion functions [83]. For the models that fully incorporated dielectric dispersion, tissue properties were calculated at frequencies between 1 kHz and 512 kHz at 1 kHz increments. For all other models, tissue properties were calculated at the estimated median normalized frequency of a single stimulation pulse (Table 4). In all approaches, gray matter was assumed isotropic, and cerebrospinal fluid (CSF) was assumed isotropic, frequency independent, and purely resistive (σ = 1.79 S/m, ε_r = 0) [183].

Table 4. Isotropic tissue properties at the stimulation pulse median estimated frequency for each subject.

Subject	**Stimulation pulse estimated median frequency (Hz)**	**Gray matter**		**White matter**	
		Conductivity (S/m)	**Relative permittivity**	**Conductivity (S/m)**	**Relative permittivity**
J	5530	0.110	38570	0.067	19452
N	4200	0.108	49600	0.066	23734

3.3.2.2.1. Scaled eigenvalue (SE) conductivity tensor map

The scaled eigenvalue (SE) conductivity tensor map was calculated using the linear cross-property relationship between conductivity and diffusion tensors [88]. The tissue conductivity tensor eigenvalues were calculated by scaling the diagonal matrix diffusion tensor eigenvalues (λ_1, λ_2, and λ_3) by a factor s:

$$\sigma = s * \begin{bmatrix} \lambda_1 & 0 & 0 \\ 0 & \lambda_2 & 0 \\ 0 & 0 & \lambda_3 \end{bmatrix} \tag{24}$$

where s was 0.844 S s/mm^3. The resulting diagonal matrix of conductivity tensor eigenvalues (σ) was used in Equation 23 to calculate the tissue conductivity tensor (Σ) for each voxel.

3.3.2.2.2. *Normalized volume (NV) conductivity tensor map*

The normalized volume (NV) conductivity tensor map [90,149] was calculated by scaling each diffusion tensor eigenvalue (λ_i) by the ratio of the geometric volume of the isometric conductivity tensor to the geometric volume of the diffusion tensor:

$$\sigma_i = \frac{\frac{4}{3}\pi * \sigma_{iso}^3}{\frac{4}{3}\pi * \lambda_1\lambda_2\lambda_3}\lambda_i \qquad ()$$

where σ_{iso} is the isometric conductivity of white matter and λ_1, λ_2, and λ_3 are the tensor primary, secondary, and tertiary eigenvalues. The diagonal matrix of conductivity tensor eigenvalues (σ):

$$\sigma = \begin{bmatrix} \sigma_1 & 0 & 0 \\ 0 & \sigma_2 & 0 \\ 0 & 0 & \sigma_3 \end{bmatrix} \qquad ()$$

was used in Equation 23 to calculate the tissue conductivity tensor (Σ) for each voxel.

3.3.2.2.3. *Volume constraint (VC) conductivity tensor map*

The volume constraint (VC) conductivity tensor map, described previously by [89], was calculated by constraining the geometric volume of the anisotropic conductivity tensor to equal the geometric volume of the anisotropic conductivity tensor:

$$\frac{4}{3}\pi\sigma_{\parallel}\sigma_{\perp}^{2} = \frac{4}{3}\pi\sigma_{iso}^{3} \qquad ()$$

where $\sigma_{\parallel}$ is the conductivity of white matter in the direction parallel to a fiber tract, $\sigma_{\perp}$ is the conductivity of white matter in the direction perpendicular to a fiber tract, and σ_{iso} is the isotropic conductivity of white matter. The ratio of parallel to perpendicular conductivity (r) was used to calculate conductivity in both directions:

$$\sigma_{\parallel} = \sqrt[3]{\sigma_{iso}^{3} r^{2}} \qquad ()$$

$$\sigma_{\perp} = \sqrt[3]{\frac{\sigma_{iso}^{3}}{r}} \qquad ()$$

where r was 9 [84]. The calculated value for parallel conductivity was used as the primary conductivity tensor eigenvalue and the calculated value for perpendicular conductivity was used for both the secondary and tertiary conductivity tensor eigenvalues. The diagonal matrix of conductivity tensor eigenvalues (σ) was then used in Equation 23 to calculate the tissue conductivity tensor (Σ) for each voxel.

Table 5. Anisotropic tissue properties at the stimulation pulse median estimated frequency for each subject.

Subject	**Stimulation pulse estimated median frequency (Hz)**	**White matter conductivity (S/m)**	
		Parallel	**Perpendicular**
J	5530	0.290	0.0322
N	4200	0.286	0.0317

3.3.2.3.Multi-compartment axon models

Topographic subsections of the corticospinal tract of the IC were segmented through probabilistic tractography performed using FSL [179]. Probabilistic tractography was guided by seed and way masks that were defined within the T2-W images of each subject in reference to an atlas of the rhesus macaque brain [184] and a reference text on the fiber tracts of the rhesus macaque brain [185]. A seed mask was created in the right hemispheric $M1_{arm}$ and a way mask was created within the right hemispheric internal capsule, slightly posterior and ventral of the subthalamic nucleus (STN). Masks were transformed from the T2-W coordinate system into the diffusion coordinate system using FLIRT [180,186] in FSL. The transformed mask and the output of BEDPOSTX (Section 3.3.2.2) were used by PROBTRACKX [187] in FSL to produce probabilistic maps of the region of the internal capsule that projects from $M1_{arm}$ to the spinal cord. A digital rendering of the CST_{arm} was generated by thresholding the probabilistic tractography map in reference to the previously cited reference text on the fiber tracts of the rhesus macaque brain [185]. The surface reconstruction was then used to guide construction of a population of multi-compartment axons (Figure 15D).

Each fiber tract reconstruction was pseudo-randomly populated with 1000 multi-compartment axon models. Results from simulations with 100 to 1000 axons were compared and the resulting activation profiles converged to within 1% when 500 or more axons were modeled. To prevent artifacts relating to model axon density the full population of 1000 axons were used in subsequent stimulations. The population of multi-compartment axons was constrained by cross-sectional contours from the digital surface reconstruction of the CST_{arm}. Axial contours separated by 5 mm were generated using Rhinoceros3D v4.0. Each contour was discretized into 100 points and the coordinates of these points were imported to Matlab R2015a. Using Matlab, each contour was populated with 3000 randomly distributed points. Splines connecting the nearest points from neighboring contours were calculated and the first 1000 splines were used to define the geometries of the 1000 modeled axons. Axons were modeled with a myelinated diameter of 2 μm in alignment with measurements taken from the internal capsule in the rhesus macaque [121]. Each axon was populated with compartments representing nodes of Ranvier, myelin attachment segments, paranode main segments, and internode segments connected by an axial resistance. Axon compartment properties and order were consistent with the multi-compartment axon cable model developed previously [99,122,147,164].

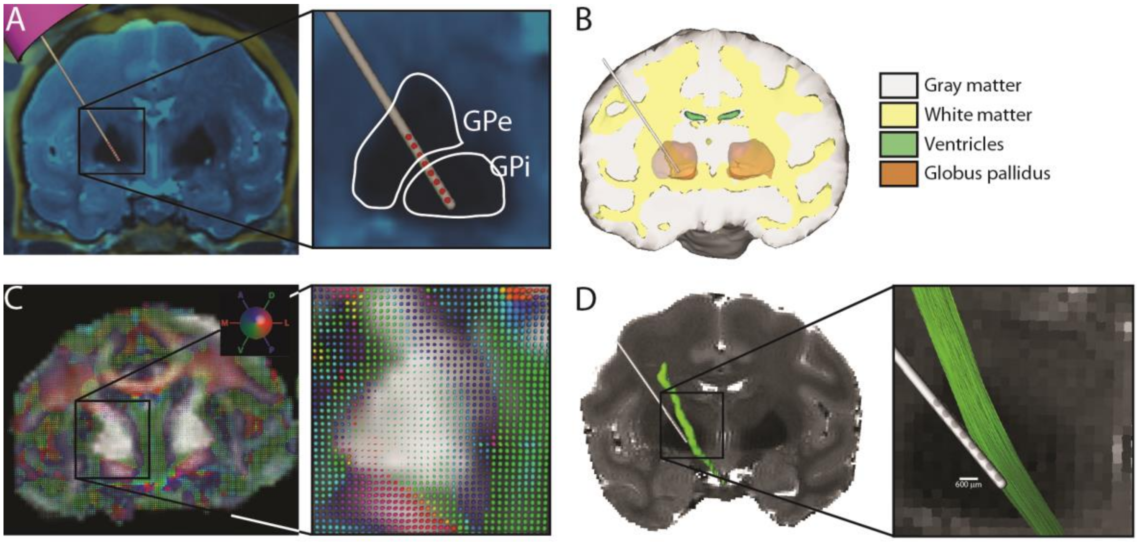

Figure 15. Brain tissues were segmented manually and multi-compartment axon tracts were created using probabilistic tractography. Preoperative MRI was co-registered with postoperative CT (A). Gray matter, white matter, and the lateral ventricles were segmented using the co-registered MRI, and a digital representation of the DBS lead was placed in accordance with the co-registered postoperative CT imaging (B). Probabilistic tractography was performed using DWI (C) to segment the $\mathrm{CST}_{\mathrm{arm}}$ within the right hemisphere (D). The segmented region of the internal capsule was used to guide the pseudorandom creation of 1000 multi-compartment axon geometries.

3.3.2.4.Finite element model

A finite element model was created for each subject in Comsol Multiphysics v5.2. Each model was created in alignment with the original DWI coordinate system so that no transformation of the tissue conductivity tensor map was required.

3.3.2.4.1. Model geometry

The geometry of the model included a smoothed reconstruction of the subject's brain, a surface representation of the cephalic chamber, the DBS(A) lead. A reconstruction of each brain was smoothed to the extent that the cortical sulci were no longer visible on the surface. The smoothed brain was used in order to simplify meshing while maintaining the overall shape. Brain reconstructions were imported using Comsol Multiphysics CAD import module. The cephalic chamber was represented as distinct region on the surface of the brain as a circle with an outer diameter of 1 cm. It should be noted that in the experimental preparation, the cephalic chamber rests on the skull; however, granulation tissue and residual fluid provide a conductive path between the chamber and brain. The DBS(A) lead was manually constructed within Comsol and included the lead body, the electrodes, and a 0.1 mm thick encapsulation layer. The location and orientation of the chamber and lead were determined using postoperative CT imaging. Depending on model complexity, the lead and electrodes were either included as volumetric entities or subtracted from the surrounding volume, leaving surface representations of the lead and electrodes.

3.3.2.4.2. Boundary conditions

The surface representation of the cephalic chamber was assigned as ground via the Dirichlet boundary condition of zero volts. The remainder of the brain surface was assigned the Neumann boundary condition of zero flux. In models where the lead and electrode geometries were modeled as surfaces rather than volumes, the lead body and inactive electrodes were assigned the Neumann boundary condition. Depending on model complexity, current-regulated stimulation was applied as a normal current density or using an equivalent circuit model of the electrode tissue interface (ETI). Both methods were implemented as boundary conditions on the surface of the stimulating electrode(s). In the case of the DBSA, the stimulation amplitude was evenly split across paired electrodes. Normal current density was calculated by dividing the maximum stimulation amplitude by the geometric surface area of the electrode. The equivalent circuit model was applied as a terminal boundary condition using the Comsol Multiphysics AC/DC module. The electrode tissue interface (ETI) was modeled as a three element Randles equivalent circuit model connected to a current-regulated source. The equivalent circuit model consisted of an access resistance, R_a, in series with a faradaic resistance, R_f, and double layer capacitance, C_{dl} connected in parallel. R_a was calculated by assigning 1 volt to the stimulating electrode (via the Dirichlet boundary condition), using Comsol to calculate normal current density during stimulation, calculating the effective applied current by integrating across the electrode surface, and dividing the stimulation voltage by the effective applied current. R_f was calculated by dividing the distributed faradaic resistance of platinum electrodes (150 Ω-cm^2 [119]) by the electrode surface area. C_{dl}

was calculated by multiplying the electrode surface area by the distributed double layer capacitance of platinum electrodes (30 μF/cm^2 [119]).

3.3.2.4.3. Mesh

Meshing was performed via Delaunay triangulation using Comsol. Mesh element size and growth parameters for the brain were varied depending on model complexity. To account for the small size and radius of the lead, electrodes, and encapsulation layer, the minimum and maximum mesh element size of these model domains was 0.01 and 0.1 mm. A small-domain mesh refinement study was performed for these small domains and further refinement of the mesh changed the average FEA results by less than 1%. The shape function order used was the Comsol default (quadratic) except where specified otherwise.

3.3.2.4.4. Material properties

Text files containing the brain tissue conductivity tensor maps and relative permittivity values at a given frequency were automatically imported to Comsol as spatially dependent variables using the Comsol module, Livelink with Matlab. The tissue properties of the brain were assigned by interpolating the tissue conductivity tensor map and relative permittivity onto the finite element mesh using the nearest neighbors function. The encapsulation layer conductivity and relative permittivity were assigned isotropic values of white matter in order to represent the presence of a glial scar [155]. In models where the lead and electrodes were included as volumes, the material properties were assigned in accordance with previous DBS modeling work (lead body: σ = 1e-13, ε_r = 2) and (electrodes: σ= 5e-6, ε_r = 1) [188,189].

3.3.2.5.Predicting stimulation induced axonal activation

3.3.2.5.1. The Fourier finite element method (FFEM)

The Fourier finite element method (FFEM), described by Butson and McIntyre [190], was used to incorporate reactive tissue components and dielectric dispersion, both of which have been shown to significantly contribute to waveform shaping [190,191]. The FFEM was implemented as follows: A subject-specific stimulation waveform (1 msec in duration and discretized into 1024 points) was created in Matlab (Figure 16A). The 1024 point discrete Fourier transform (DFT) of the stimulation waveform was calculated using Matlab, producing estimates of the stimulation pulse phase and magnitude at 513 frequencies: 0 through 512 kHz at 1 kHz increments (Figure 16B,C). At the same 513 frequencies, the FEA was used to solve the time harmonic electroquasistacic equation:

$$-\nabla[\sigma(\omega)+j\omega\varepsilon_0\varepsilon_r(\omega)]\nabla\Phi=0 \qquad ()$$

where σ is conductivity, ω is angular frequency, ε_0 is the permittivity of free space (8.85 x 10^{-12} F/m), ε_r is relative permittivity, and Φ is scalar electric potential. FEA was performed using the direct MUltifrontal Massively Parallel sparse direct Solver (MUMPS) in Comsol Multiphysics v5.2 on clusters at the Minnesota Supercomputing Institute at the University of Minnesota. In the dielectric dispersion model, tissue property maps were incorporated that were consistent with the frequency being solved. In all other models, the tissue property maps were consistent with the estimated normalized median frequency of the stimulation pulse regardless of the frequency being solved. The real and imaginary components of the calculated tissue potential (Figure 16D,E) were interpolated at the three-dimensional coordinate of each axon compartment using Comsol LiveLink with Matlab. A stimulation waveform for each compartment of each axon model was reconstructed by scaling the simulation pulse DFT by the compartment potential at each frequency, and performing the inverse DFT on the result (Figure 16F). The resulting waveform was duplicated and concatenated nine times to create a ten pulse stimulation train at 130 Hz.

3.3.2.5.2. Multi-compartment axon modeling

Stimulation pulse trains were simultaneously played into each compartment of a given axon using the NEURON v7.3 programming environment [192]. This was performed by perturbing the axonal membrane voltage using the *extracellular* mechanism (*e_extracellular),* in a manner consistent with previous modeling work [193]. Using NEURON, action potential counters were attached to each node and simple thresholding was used to detect stimulus driven spike activity. An axon was considered ‘activated’ if an action potential was detected within 3 msec following 80% of stimulation pulses. Stimulation amplitude was varied until the threshold for activation was narrowed to a window of +/-0.05 mA. Activation profiles were then created for using all 1000 axons (Figure 16G).

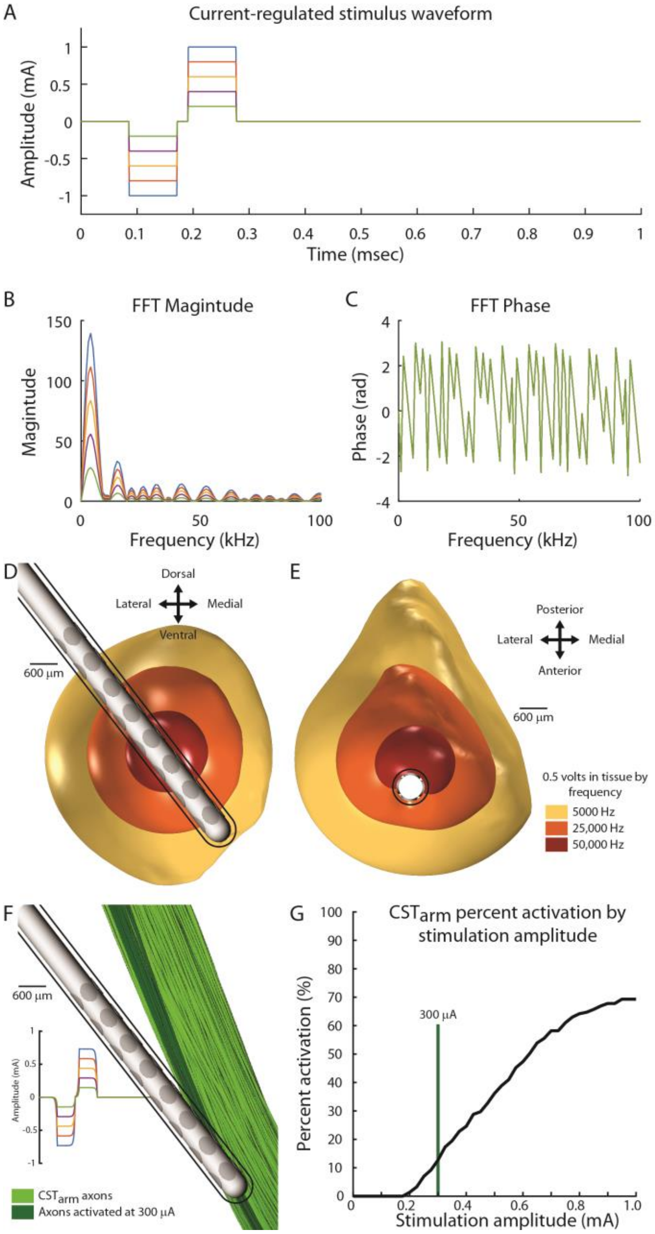

Figure 16. Axonal activation was modeled using the Fourier finite element method. The 1024-point discrete Fourier transform (DFT) of the stimulation pulse (A) was used to calculate magnitude (B) and phase (C). The time harmonic Laplace equation was solved in the frequency domain using FEA at each frequency represented within the stimulation

pulse DFT (D and E). The stimulation pulse DFT was scaled by the FEA result at the location of each axon model compartment and the inverse DFT was performed to generate a compartment-specific stimulation pulse (F). Simulations of multi-compartment axons exposed to trains of compartment-specific stimulation pulses were performed using the NEURON programing environment and used to generate activation profiles (G) for each electrode stimulation configuration.

3.3.3. Model comparison to experimental data

For both subjects, model predictions were compared to *in vivo* motor contraction thresholds for stimulation through each electrode by calculating percent error. Percent error was calculated between the motor contraction stimulation amplitude threshold and the model-predicted stimulation amplitude required to achieve 10, 15, and 20% activation, per the activation profile curve. This resulted in three values for percent error, which were calculated for each conductivity map. In Subject J, model predictions using each conductivity map were compared directly to *in vivo* cortical recording results by calculating root mean squared error (RMSE) across trials. Each trial consisted of stimulation through a single electrode at a specific stimulation amplitude. As described previously, stimulation was delivered using C0 through C5 at three different stimulation amplitudes resulting in 18 trials. Error was calculated for each trial (indicated by the subscript *i*) as the difference between the calculated percentage of experimentally recorded $M1_{arm}$ cells with putative antidromic activity (y_i) and the model-predicted percent activation ($\hat{y}_i$) during stimulation.

$$RMSE = \sqrt{\frac{1}{n}\sum_{i=1}^{n}(y_i - \hat{y}_i)^2} \qquad ()$$

where *n* is the number of trials.

3.4.Results

3.4.1. GPi-DBS motor contraction thresholds and electrophysiology in $M1_{arm}$ (Subject J)

GPi-DBS induced motor contractions in the contralateral upper extremity of Subject J (Table 6), including elbow, wrist, and finger flexion and extension. Stimulation thresholds for inducing muscle contractions were higher for electrodes located proximally along the DBS lead, which not surprisingly corresponded to the electrodes with the largest spatial separation to the CST.

Table 6. Subject J motor contraction stimulation amplitude thresholds and $\mathrm{M1_{arm}}$ percent activation.

Electrode	**Motor contraction stimulation amplitude threshold (mA)**	**Motor contraction**	**Percent activation calculated from $\mathrm{M1_{arm}}$ recordings (%)**
C5	0.8	Elbow extension	0
C4	0.7	Finger extension	0
C3	0.6	Elbow extension	8
C2	0.5	Elbow extension	10
C1	0.3	Elbow flexion	16
C0	0.2	Elbow flexion	12

Zero percent $\mathrm{M1_{arm}}$ activation was recorded at the motor contraction stimulation amplitude threshold of the two most proximal electrodes, C4 and C5. Across electrodes C0 through C3, the average percent activation recorded from cortex at the motor contraction threshold was 11.5 percent. For the electrodes where stimulation at the motor contraction threshold was greater than zero, C0 through C3, $\mathrm{M1_{arm}}$ percent activation was impacted by electrode location and stimulation amplitude (Figure 17). For each electrode, increasing stimulation to 125% of threshold and decreasing stimulation to 75% of threshold increased and decreased $\mathrm{M1_{arm}}$ percent activations respectively. For all electrodes, $\mathrm{M1_{arm}}$ percent activation decreased for electrodes that were further from the target, but this effect was most dramatic for stimulation at 125% of threshold.

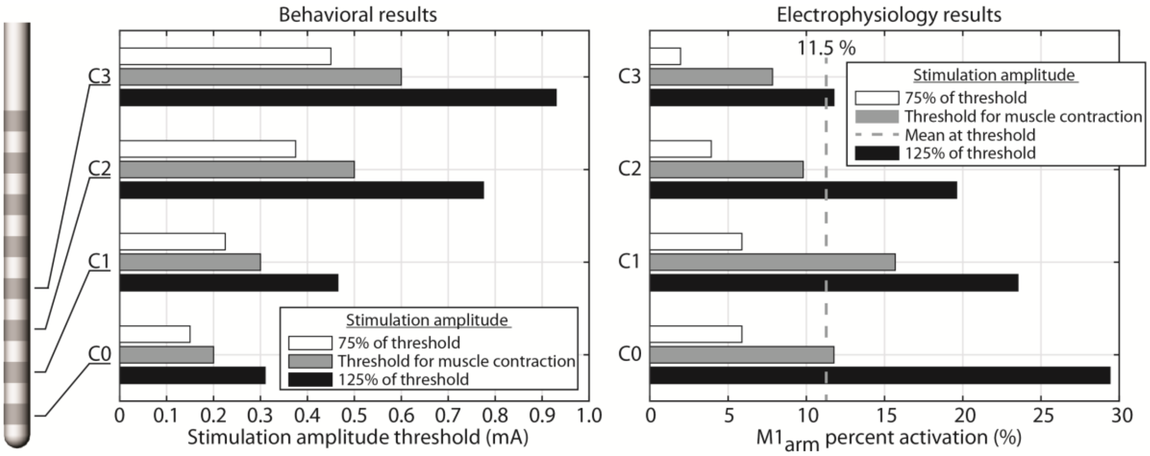

Figure 17. Motor contraction stimulation thresholds increased for more proximal electrodes. Percent activation of $M1_{arm}$ at the motor contraction stimulation threshold was highest and was within the range of 7-16 % for electrodes C0 through C3.

3.4.2. GPi-DBS conventional lead model predictions (Subject J)

DBS lead model predictions of activation (Subject J) using the three different conductivity tensor maps differed significantly within the stimulation amplitude range of 0-1 mA (Figure 18). For stimulation using any of the four most proximal electrodes, zero percent activation was predicted for stimulation ≤1 mA. Additionally, simulations using the SE conductivity map failed to reach 10% activation for stimulation ≤1 mA using any electrode. Considering only the four most distal electrodes, the magnitude of the average difference between activation profiles produced using the NV and VC conductivity maps was 6 percentage points. The average difference between activation profiles produced using the SE conductivity map and the VC and NC conductivity maps were 40% and 47%, respectively.

For the purposes of analysis 10% activation was selected for detailed consideration based on the percent activation range that was calculated from cortical recordings (Table 6). Stimulation at 0.1 mA using the most distal electrode (C0) resulted in approximately 10% activation for both the NV or VC conductivity maps; however, the two model predictions diverged as stimulation amplitude increased. The difference in percent activation increased to approximately 15 percentage points at 1 mA with the NV map producing a higher prediction of activation. The difference in activation between models incorporating the NV and VC conductivity maps for stimulation using the C1 and C2 electrodes was zero to five percentage points.

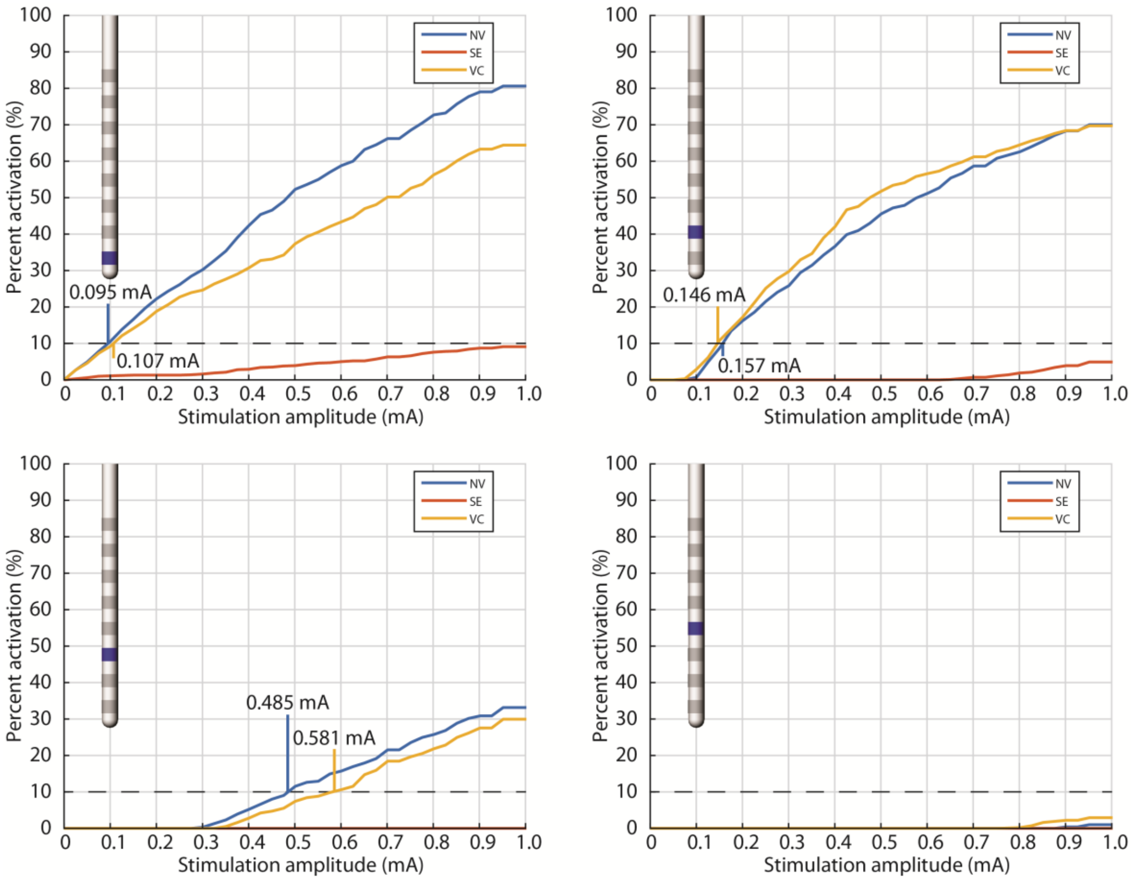

Figure 18. Activation profiles generated from models using the NV, VC and SE conductivity maps. Predictions of activation were significantly higher for the NV and VC conductivity maps in comparison to the SE map.

3.4.3. DBS model validation in reference to cortical recording results (Subject J)

Comparisons between percent activation from the $M1_{arm}$ recording array and model predictions of percent activation showed that models using the NV conductivity map produced results that best aligned with the experimental results in Subject J (Figure 19). Only stimulation using the three most distal electrodes: C0, C1, and C2 produced results where both model predictions of percent activation and $M1_{arm}$ calculations of zero percent activation were non-zero (Figure 19, left). The SE conductivity map performed poorest with a RMSE equal to 11.8. The NV conductivity map performed best with a RMSE equal to 6.08 (Figure 19, right). Prediction errors from the SE conductivity map were positive indicating the models under predicted percent activation. Prediction errors from the NV and VC conductivity maps were positive except for stimulation using C0 at 75% and 100% of the motor contraction threshold and stimulation using C1. Considering only electrodes C0, C1, and C3, the VC conductivity map modeling results produced slightly more accurate predictions of percent activation than the NV conductivity map in all cases except for the 75% and 100% of the motor contraction thresholds using C0.

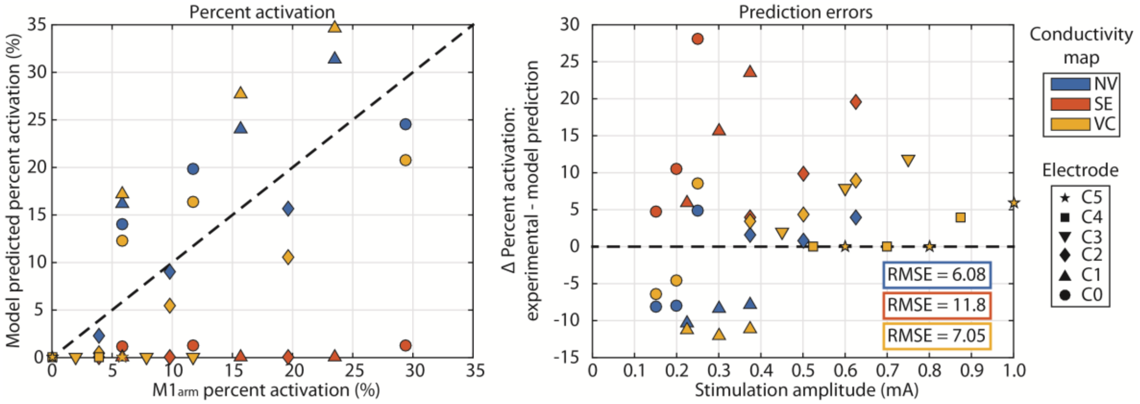

Figure 19. The NV conductivity map out performed both the SE and VC conductivity maps in terms of both RMSE and the coefficient of determination. The models under predicted activation except in the case of stimulation using C1 and stimulation using C0 at 75% and 100% of the motor contraction threshold.

3.4.4. *Directional effects of GPi-DBS on motor contraction thresholds (Subject N)*

Directional stimulation induced motor contractions were observed in Subject N using the radially segmented DBS array (Figure 20). The observed motor contraction was flexion of the fingers. Stimulation thresholds were highest for stimulation configurations using electrodes facing away from internal capsule (anterior). The lowest stimulation thresholds were consistently from stimulation configurations that included only electrodes nearest internal capsule (posterior). The directional bias was greatest for the most distal electrodes and decreased for more proximal rows that were farther from the internal capsule, which is consistent with the results from Subject J described above. On average, the stimulation threshold was 30% higher for electrodes facing away from the internal capsule (anterior) than for electrodes facing the internal capsule (posterior). Additionally, the difference between the stimulation threshold from the column with the highest threshold and the column with the lowest threshold was 0.12 mA on average.

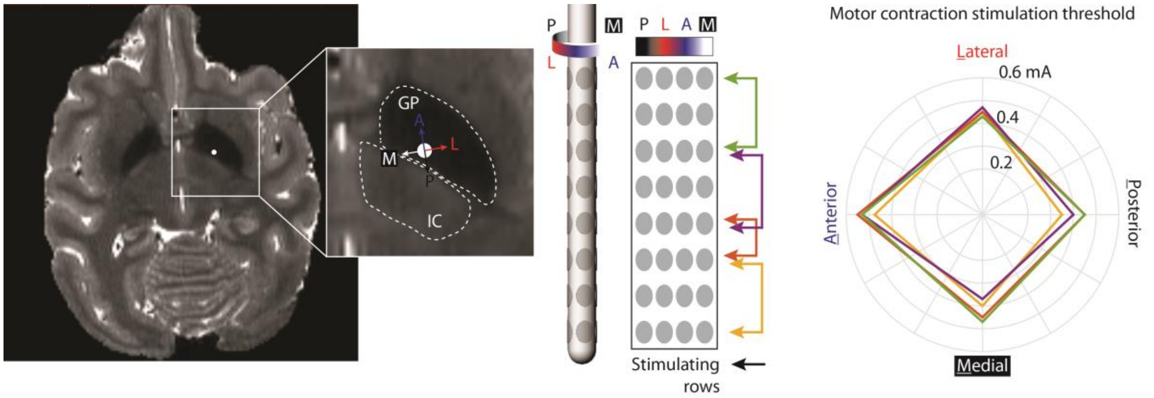

Figure 20. Motor contraction stimulation thresholds were observed to be lowest for stimulation through the posterior facing electrodes and highest for stimulation through the anterior facing electrodes. GP = globus pallidus, IC = internal capsule, A = anterior, P = posterior, M = medial, L = lateral.

3.4.5. GPi-DBS array model predictions (Subject N)

Similar to the conventional DBS lead model predictions, predictions of axonal activation with the DBS array differed significantly amongst the three different conductivity tensor maps (Figure 21). Within the 0-1 mA stimulation amplitude range, >10% activation was predicted only using the NV and VC tissue conductivity maps for the two most distal electrode groups and only for electrodes in the two columns closest to the IC. Simulations using the SE conductivity map failed to reach 10% activation for stimulation ≤1 mA using any electrode. Considering only the electrode configurations where >10% activation was predicted within 0-1 mA, the VC conductivity map predicted percentages that were 10-60 points higher that predictions produced using the NV conductivity map. Increasing the modeled stimulation amplitude range to 0-5 mA enabled for visual inspection of the model prediction trends and enabled quantification of the stimulation amplitude required to achieve 10% using the three most distal electrode groups as was done in the case of the conventional DBS lead modeling results. Within the 0-5 mA range, higher activation was predicted for the more distal electrode groups. For distal electrode groups, the activation profile plateaued when it neared 100% activation, while for more proximal electrode groups, the activation profiles were much more linear and did not plateau and/or did not near 100% activation.

The stimulation amplitudes needed to achieve 10% activation using the DBSA model were much higher than those using the DBS lead. For all electrode groups using both the NV and VC conductivity maps, the models predicted an extreme directional bias. Using any of the conductivity maps, stimulation within 0-5 mA using the most proximal electrodes did not result in predictions of at least 10% activation in all directions, and therefore, this group of electrodes was not plotted nor quantified in detail. Additionally, using the SE conductivity map, stimulation within 0-5 mA did not result in predictions of at least 10% activation in all directions for any of the electrode groups, and therefore, this group of electrodes was not plotted nor quantified in detail. On average, for both NV and VC conductivity maps, stimulation amplitude was approximately 300% higher for the electrode column with the highest required amplitude (anterior) in comparison to the electrode column with the lowest required stimulation amplitude (posterior). The range of the stimulation amplitude differential was smaller for the NV conductivity map (226-365%) than for the VC conductivity map (150-503%).

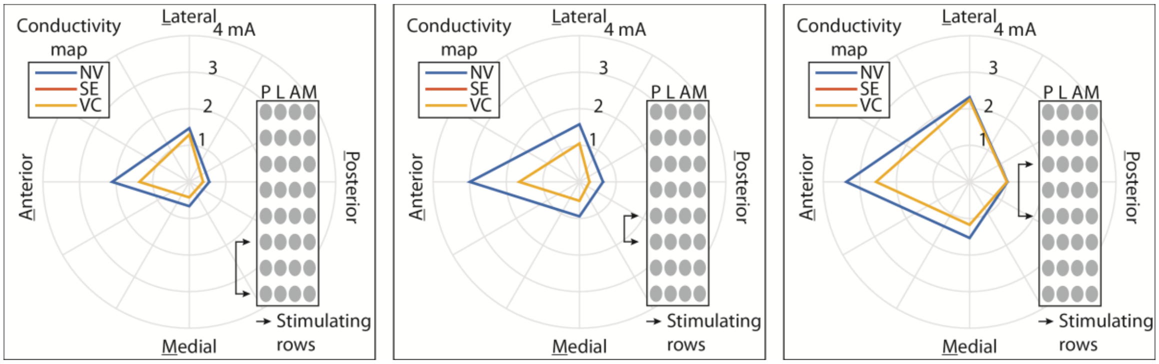

Figure 21. Model predictions of the stimulation amplitude required to reach 10% CST_{arm} activation models of Subject N using the NV and VC conductivity maps. Stimulation amplitudes predicted using the SE conductivity map was greater than 4 mA in at least one direction for each stimulating row, and therefore was excluded.

3.4.6. DBS conventional lead model predictions versus motor contraction thresholds (Subject J)

Model results were considered in the context of DBS lead motor contraction thresholds in two ways. First, by evaluating the model predicted percent activation at the motor contraction stimulation amplitude threshold using each conductivity map; and second, by calculating the percent error between the motor contraction stimulation amplitude and the model predicted stimulation amplitude required to activate 10, 15, and 20% of modeled axons (Figure 22). Using the SE conductivity map, predictions at the motor contraction threshold were less than 5% for the most distal electrode (C0) and were zero for all other electrodes. For electrodes C0 through C2, model predictions using the NV and VC conductivity maps were within 5 percentage points; however, the predicted percent activation was not consistent across electrodes. Further, comparing the results from the NV or VC conductivity maps, neither produced a consistently higher or lower prediction of activation. Percent activation predicted using either the NV and VC conductivity maps fell within the following ranges C0: 16.4 to 19.8% | C1: 24 to 27.7% | C2: 5.5 to 9%. The lowest percent error between the motor contraction stimulation amplitude and the model predicted stimulation amplitude changed for different electrodes (Figure 22). For C0 and C1 the stimulation amplitude required to activate 20% of axons using either the NV or VC conductivity maps had the lowest error, while 10% activation using either the NV or VC conductivity maps resulted in the lowest error for C2. Where the models did not predict activation of at least 10% within the 0-1 mA range, 1 mA was used to calculate the minimum error. For C3, the magnitude of the minimum error using any of the three conductivity maps was greater than 67%. For the more distal electrodes: C0, C1, and C2, models using the SE conductivity map did not predict at least 10% activation within the 0-1 mA range and, therefore, the minimum magnitude of the error was greater than 100%.

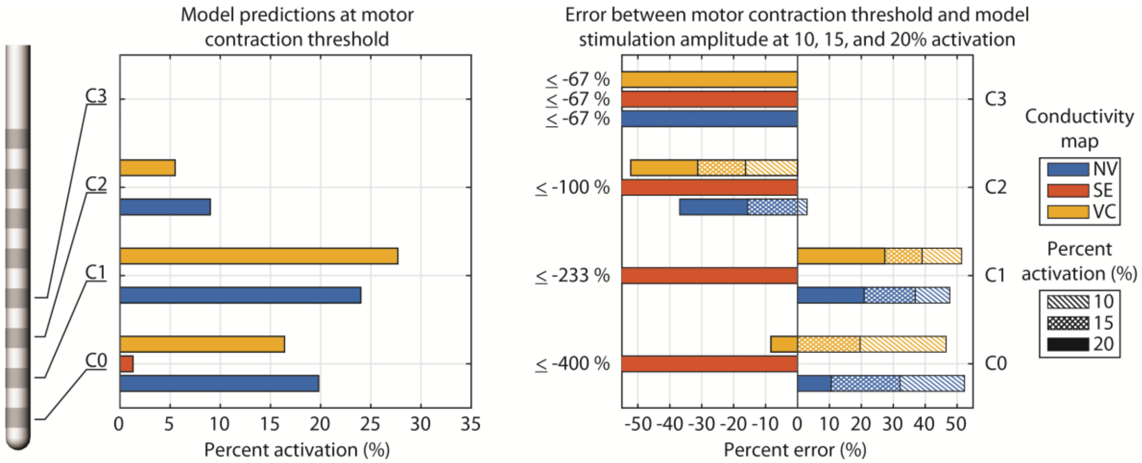

Figure 22. Model predictions of percent activation at the motor contraction threshold. Using the SE conductivity map, activation was predicted to be < 3%. Activation predicted using the NV or VC map was 5-28% and neither map resulted in predictions of consistently higher predictions. The percent error between the motor contraction stimulation amplitude and the model predicted stimulation amplitude required to activate 10, 15, and 20% exceeded 50% for all electrodes. Using the NV or VC map, error was 9-10% comparing the motor contraction threshold to the model predicted stimulation amplitude required to achieve 20% activation.

3.4.7. DBS array model predictions verses behavioral thresholds (Subject N)

Model results using the DBS array were evaluated using the same methods that were utilized for the DBS conventional lead model comparison. For all but three stimulation configurations, the models predicted zero percent activation at the motor contraction threshold. Within these three configurations, only models using the VC conductivity map predicted greater than zero percent activation, and the model predictions were less than 10%.

The magnitude of percent error between the motor contraction stimulation amplitude and the model predicted stimulation amplitudes required to activate 10, 15, and 20% of modeled axons were much higher in all cases than the percent error calculated from models of the DBS lead (

Figure 23). Where the models did not predict activation of at least 10% within the 0-5 mA range for all four directions, error was not plotted. These models included models that relied on the SE conductivity map, and models of simulation using the most proximal group of electrodes. The range of minimum errors from using the SE conductivity map was 650-1250% depending on electrode configuration. For all electrode configurations, percent error was lowest when comparing the motor contraction stimulation amplitude and the model predicted stimulation amplitude required to activate 10% of modeled axons using the VC conductivity map. Considering only the NV and VC conductivity maps using only the three most distal electrode groups, percent error was lowest, on average, for the most distal group of electrodes, which was closest to the $\mathrm{CST}_{\mathrm{arm}}$ tract, and increased with distance as the electrode groups that were used were further from the

$\mathrm{CST_{arm}}$ tract. Additionally, percent error was lowest for electrodes in columns facing the $\mathrm{CST_{arm}}$ tract and increased strongly for electrodes facing away from the $\mathrm{CST_{arm}}$ tract.

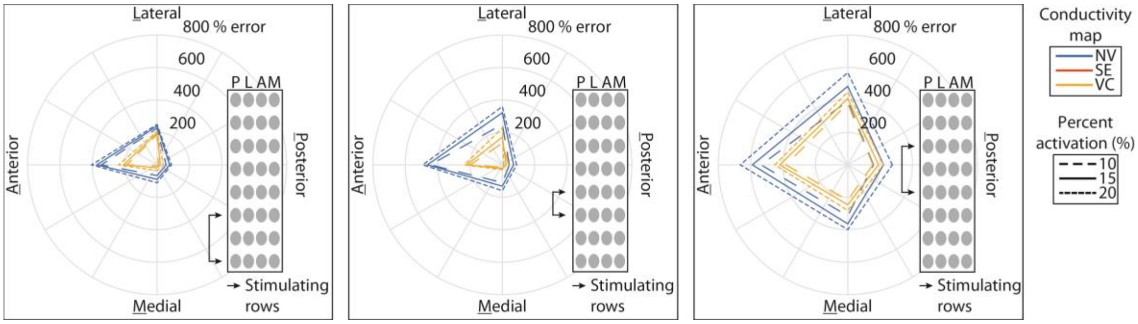

Figure 23. The magnitude of percent error between the motor contraction stimulation amplitude and the model predicted stimulation amplitude required to activate 10, 15, and 20% of the $\mathrm{CST_{arm}}$ fibers. Note that posterior and lateral columns faced the $\mathrm{CST_{arm}}$ tract.

3.5.Discussion

Models of DBS have been increasingly utilized in research and clinical practice over the past two decades. To be properly utilized, it is important to understand the accuracy of model outcomes and to understand precisely how model predictions of cellular activity relate to behavioral outcomes. This understanding is vital in circumstances where models are used to guide clinical decision making. For example, in the scenario where models are used to guide or optimize stimulation parameters; a practice that may become necessary for next-generation DBS leads with many electrodes that cannot be feasibly programed using conventional trial-and-error programming strategies. Previous studies have compared computational modeling results to therapeutic effects and side-effects in patients [66,147] and preclinical animal models [99,148,164]. However, these studies are severely limited by the lack of model validation and the unclear relationship between model predictions of cellular activation and behavioral or clinical outcomes.

Previous DBS computational modeling studies have established that subject-specific inhomogeneous and anisotropic tissue properties significantly impact model predictions [85,87]. This effect is due primarily to the inhomogeneous conductance of the brain as a whole and the close proximity of DBS target brain structures to highly anisotropic axon tracts such as the internal capsule. Several methods have been proposed within the brain modeling literature for calculating subject-specific anisotropic tissue conductivity maps [88–90]. With only a few exceptions, [149,194], DBS models have relied upon the method described by Tuch et al. for calculating subject-specific anisotropic tissue conductivity maps [66,147,148]. Comparative modeling studies using different methods for calculating subject-specific anisotropic tissue conductivity maps are rarely performed in the context of DBS and therefore model sensitivity to this parameter remains unknown.

The results of our study include: (1) stimulation induced activation in motor cortex at the motor contraction threshold amplitude was measured within the range of 8-16% for distal electrodes and 0% for most proximal electrodes. (2) Motor contractions were able to be induced using all electrodes, but higher stimulation amplitudes were required for increasingly proximal electrodes. (3) In comparison to motor contraction thresholds, model predictions using the DBS array strongly over predicted the degree of directional steering. (4) Error between model predictions and motor cortex recordings was lowest for models that relied on the normalized volume constraint method and was largest for models that relied on the scaled eigenvalue method.

3.5.1. Relating $M1_{arm}$ activity patterns to behavior

In both subjects, the stimulation amplitude required to evoke muscle contractions increased for proximal electrodes and decreased for distal electrodes. This increase was most obvious and consistent in Subject J, where the threshold stimulation amplitude increased at increments of approximately 0.1 mA as the stimulating electrode was changed from one electrode to an adjacent and more proximal electrode. It was anticipated that regardless of which electrode was used for delivering stimulation, CST_{arm} predictions of activation from cortical recordings would be generally consistent if similar motor contractions were observed. However, CST_{arm} predictions were inconsistent between distal and proximal electrodes. On average, in Subject J, 11.5% activation within CST_{arm} was measured at the stimulation amplitude threshold using the four most distal electrodes. In contrast, 0% activation was measured during stimulation using the two most proximal electrodes. This result suggests that (1) the brain area within M1 covered by a single cortical array was not sufficient to capture the full extent of antidromic

CST_{arm} activation that resulted from stimulation and/or (2) stimulation of pathways other than the CST_{arm} were responsible for generating motor contractions during stimulation using the two most proximal electrodes. Alternative pathways that may have been stimulated include those at various levels within the CST, such as fibers from premotor cortex and supplementary motor area, which are known targets of cerebellar output [195–197]. In this study, GPi was selected as the target rather than STN or thalamus in order to limit the potential for stimulating complex fiber pathways; however, projections to different cortical regions are not precisely segmented within the CST [185] making isolation of single CST subregion in this manner difficult.

3.5.2. Relating $M1_{arm}$ activity patterns and behavior to model predictions

Results from cortical recordings best aligned with model predictions of percent activation that were generated using the NV conductivity map. The error in SE map model predictions was found to be much higher than either the NV map or the VC map model predictions. Both the NV and VC maps were generated using DWI data in combination with the Gabriel dispersion model, suggesting that conductivity maps that leverage both inputs generate more accurate tissue conductivity maps. Comparing the VC and NV map errors, the different was smaller but the NV map generated a lower estimate of error. This finding indicates that the normalized DTI eigenvalues provide a better estimate of anisotropy in brain tissue conductivity than artificially imposed anisotropy using the 9:1 ratio described by Nicholson in 1965 [84]. This outcome is perhaps not surprising as the measurements taken by Nicholson did not sample enough brain areas to generate an estimate of variance; however, this observation is notable considering that it is commonly cited used to define white matter anisotropy in models of the brain.

Model predictions of activation at the stimulation thresholds for inducing motor contractions differed strongly between the DBS lead and the DBSA. NV map model predictions of activation during stimulation using the DBS lead (Subject J) were 19.8% for electrode C0, 24% for electrode C1, 9% for electrode C2 and 0% for all other electrodes. Overall, error was lowest for model predictions using the NV conductivity map; however, $M1_{arm}$ activation was approximately 10 percentage points lower than the

NV model predicted percent activation for subthreshold stimulation and threshold stimulation using electrodes where both experimental and model predicted percent activation were greater than zero. Alternatively, for suprathreshold stimulation, model predictions were 2-5 percentage points higher than $M1_{arm}$ percent activation. These results suggest that the overall shape of the model generated activation curve is inconsistent with the experimental results. In each of the presented models, the activation curve generated by model predictions increased gradually as stimulation amplitude increased in a near-linear manner. The experimental data suggest that the activation profile curve should rise more quickly at low stimulation amplitudes and rise more slowly at high stimulation amplitudes but not fully plateau within the range so stimulation amplitudes evaluated. However, the currently available experimental data are insufficient to define an experimental activation profile. Future validation studies may address this issue by collecting experimental data at motor contraction stimulation thresholds and at a range of sub/supra threshold stimulation amplitudes. Additionally, future work should incorporate more samples in order to allow for the distribution and variance of an experimental activation to be characterized and considered in the context of model validation. Assuming the true activation profile rises sharply at low stimulation amplitudes and levels off near the behavioral threshold, one consideration that could change the shape of the model generated activation profile is the anatomical representation of the CST_{arm}, which was generated by thresholding probabilistic tractography results. This procedure generates a single three-dimensional surface, which was uniformly populated with multi-compartment axons. The surface provides a convenient means to geometrically constrain the creation of a population of model axons; however, this may not capture the true distribution of axons that project from a single cortical region within the CST. Retrograde tracing studies have shown these topographic representations of CST fibers to be density distributed in one region of the CST, but then be more sparsely represented throughout the full extent of the CST [185]. This in mind, perhaps probabilistic tractography should be utilized seed the density, rather than simply the primary location, of different fiber projections within various CST topographical regions. It is reasonable to hypothesize that a CST_{arm} representation with graded axon density could generate an activation profile curve with a steeper accent at slow stimulation amplitudes. However, extensive modeling would be required to show this effect, given the dependence of model outcomes on other parameters such as the brain tissue conductivity map. Comparisons between retrograde tracing studies and model axon trajectories generated using the proposed approach would provide valuable insight regarding the sensitivity of model outcomes to the anatomical representation of fiber tracts in the brain.

Model predictions of activation during stimulation using the DBS array (Subject N) were zero at the motor contraction threshold for all configurations using any of the tissue conductivity maps. In order to make a comparison between the models and experimental data, the stimulation amplitude required to generate 10% activation in the model was selected as a conservative threshold for generating a stimulation induced motor contraction. Modeling results indicated that the stimulation amplitudes required to achieve 10% activation were larger than 1 mA in all directions but posterior, the direction of the electrode facing the $\mathrm{CST}_{\mathrm{arm}}$. Comparing the model predicted stimulation amplitudes required to achieve 10% activation to the stimulation amplitudes required to induce motor contractions, the model required much higher (an order of magnitude in some cases) stimulation amplitudes. The model also resulted in a higher degree of directional steering than was observed in the experimental results. The large difference in stimulation amplitude makes interpreting these results difficult; however, it should be noted that the degree of model predicted steering using the DBSAs is consistent with previous DBSA experimental work [101,110,112]. This finding suggests that shorting or capacitive coupling between densely distributed conductors may be responsible for the limited directional steering observed *in vivo*. Despite the potential advantages with DBSA, by design these devices have many more failure points than conventional leads. Additionally, size limitations associated with increasing the number of electrodes requires the dense packaging of insulated conductors, and in some cases, required manufacturing techniques such as thin-film microfabrication that have not be proven clinically viable for long-term implanted devices. These factors are important considerations, and although they must be considered by device manufacturers, packaging and biocompatibility should be more thoroughly considered in early investigational studies of novel electrode designs for neural stimulation.

3.5.3. Model validation

To date, only one attempt at *in vivo* electrical field validation has been performed in the context of deep brain stimulation [86]. In this study, microelectrode recordings of tissue voltage during DBS were compared to FEA predictions using a homogenous tissue conductivity map and using a subject-specific inhomogeneous and anisotropic tissue conductivity map of the brain. The results of this study further established the importance of incorporating subject-specific inhomogeneous and anisotropic tissue properties into models of DBS to accurately predict stimulation-induced electric fields in the brain. Of particular interest, the study demonstrated very good alignment between the experimental measures of voltage in the brain during stimulation and FEA results using the SE tissue conductivity map. Our behavioral results in both animals suggest that the SE map produced overprediction of the stimulation threshold necessary to generate a motor contraction. Comparisons between the two studies are difficult to make because of several key differences: (1) Thalamus and STN were targeted rather than GPi, (2) DWI was captured at 3 Tesla rather than 7 Tesla, (3) a very low subthreshold stimulation amplitude, 0.03 mA, was used, (4) the model did not incorporate tissue capacitance, and (5) a 0.25 mm encapsulation layer was assigned a conductivity of 0.18 S/m rather than a 0.1 mm encapsulation layer with a conductivity of 0.066 S/m.

In an attempt to compare model results between studies we ran our DBS lead model using a 0.03 mA amplitude stimulation waveform and captured the peak voltage of the stimulation waveform in tissue. On average, the peak voltage was 54% higher in for the models using the NV and VC conductivity maps in comparison to the model using the SE conductivity map. Using the SE conductivity map, the peak potential in tissue ranged from 1 to 8 mV within a distance of 1 to 6 mm from the stimulation electrode. These values were similar to the *in vivo* peak voltage observed by Miocinovic et al. in thalamus, 1 to 6 mV within a distance of 1 to 6 mm from the stimulation electrode. This comparison indicates that the SE conductivity map may best reflect *in vivo* voltage measures while model predictions of cellular activation using the NV or VC conductivity maps more accurately reflect cortical recordings. However, it is not possible to conclude this using only the data provided especially for low stimulation amplitudes, where model predictions in our study are most similar. Additionally, clear differences in contrast between GP and thalamus were observable in the DWI suggesting a significant difference in conductivity between the two brain regions that could significantly affect the measured stimulation waveform amplitude. Although these experiments are extremely difficult to perform, full validation may require replication of the Miocinovic et al. for GPi stimulation using a range of stimulation amplitudes that include values near a behavioral threshold.

3.5.4. Limitations

There are several key limitations of this study. Although our models did include an inhomogeneous and anisotropic representation of the electric properties of brain tissue, our models excluded several tissue types including the skull, meninges, vasculature, and CSF surrounding the brain. We assumed that high conductivity pathways exist between the brain and cephalic chamber, which was used as ground, due to the presence of granulation tissue and residual fluid; however, stimulations were not conducted to confirm the validity of this assumption. The NV and VC conductivity maps assumed the ventricles to be isotropic and purely resistive. We observed that the lateral ventricles in both subjects to be extremely narrow and considered that the choroid plexus could take up large proportion, by volume, of the ventricles potentially invalidating the assumption that the ventricles were purely resistive, homogenous, isotropic, and non-reactive. Additionally, each of the conductivity maps relied on DWI imaging with 1.1 mm isotropic resolution to represent the anisotropy of fiber tracts within the brain. The size of myelinated axons within the rhesus macaque CST; however, are on the order of microns [121]. Due to the limitations associated with DWI resolution, therefore, our conductivity maps and probabilistic tractography are both too course to capture the precise directional contributions of individual fibers.

This study included one subject with each style DBS lead, only subject with a cortical array, and involved the targeting of a single brain region, GPi. It is therefore not possible difficult to generalize our findings to other targets or to other subjects. However, the difference in predictions between models using the SE and the other conductivity maps was large enough that variance due to factors such as model complexity and uncertainty in the conductivity values are unlikely to account for this difference [151,194]. Additional validation studies will be required to determine if the measures of model validity described here are generalizable across brain regions and across subjects. This validation study, being the first of its kind, outlines a technique and provides baseline measures of error for use in future validation studies and model optimization studies.

Histological evaluation was not used to verify the locations of the DBS leads and the cortical recording array. Currently, both subjects in this study are participants in parallel studies preventing histological confirmation of electrode locations. Although verification of lead location is commonly performed using fused preoperative MRI and postoperative CT, reports estimate DBS lead localization error to be in the range of 1-2 mm [198–201]. Computational modeling studies have demonstrated that lead misplacement within 1 mm can significantly impact model outcomes [87,100]. Additionally, the analysis of cortical activity relies on the assumption that neural recordings were captured from cortical layer V pyramidal cells. This assumption is reasonable given the electrode array depth of 1.5mm and the fact that putative antidromic activity was observed on many recording channels; however, histological verification is required to verify, with absolute certainty, the cortical layer from which the microelectrode recordings originated.

3.6.Conclusions

Model predictions using the NV and VC conductivity maps aligned well with predictions of cortical activation from $M1_{arm}$ while predictions using the SE conductivity map strongly under predicted activation. This finding suggests that future DBS modeling studies should utilize tissue conductivity models that incorporate measures of conductivity rather than relying on the more commonly utilized scaled eigenvalue method. $M1_{arm}$ percent activation required to evoke motor contractions were within the range of 8-16% for the four most distal electrodes, which were nearest to the CST_{arm}, and 0% for the two most proximal electrodes. For brain targets within several millimeters of a stimulating electrode, the range of 8-16% activation establishes a soft benchmark for assessing meaningful behavioral outcomes from model generated activation profile curves. Model results using the DBS array suggest a much greater directional bias than *in vivo* behavioral outcomes. However, the model predicted directional bias seems consistent with the limited published data demonstrating directional thresholds for stimulation induced motor contractions. These findings suggest that more work is required to quantify, *in vivo*, the degree of current steering that is possible using DBS arrays and suggests that more comprehensive models that include highly conductive paths between electrodes and capacitive coupling between densely distributed conductors may be required to model current steering with DBS arrays.

3.7.Supplement: Model complexity analysis

Previous DBS modeling work has evaluated the impact of model complexity for human DBS leads with cylindrical shell electrodes [155,191,202]. In accordance with this work, an analysis was performed to determine the appropriate complexity for running models of GPi-DBS with small electrodes in the rhesus macaque brain. The analysis was performed using a model of the subject with the implanted DBSA, Subject N. The following parameters were varied in the complexity analysis: brain mesh element size, mesh element shape function order, inclusion of the ETI equivalent circuit model, inclusion of dielectric dispersion. The five models that were compared to evaluate complexity were labeled: standard model, fine resolution, cubic shape order, ETI, and dielectric dispersion (Supplementary table 1).

Supplementary table 1. Details of model complexity study.

Model label	Mesh element size (mm)		Shape function order	Number of elements	Conductivity model	ETI
	Maximum	Minimum				
Standard	5	0.1	Quadratic	271754	Median frequency	No
Fine resolution	2	0.04	Quadratic	464111	Median frequency	No
Cubic shape	5	0.1	Cubic	271754	Median	No

function					frequency	
ETI	5	0.1	Quadratic	342858	Median frequency	Yes
Dielectric dispersion	5	0.1	Quadratic	271754	Frequency dependent	No

The results from models of varying complexity were compared by calculating the mean difference (MD) between the standard model activation profile and the activation profile from each of the other models. The mean difference was calculated within 0-1 mA at 0.025 mA increments using both the NV and VC conductivity maps. The SE conductivity map did not produce activation within 0-1 mA. Although the standard model was selected as the basis for comparison, but it was not assumed to produce results that represented the true activation profile. Therefore, variation in activation profile that could be attributed to complexity was considered in the context of the model validation results.

Overall, electrode-tissue interface and finite element model complexity (beyond the standard model parameter settings) was found to have a minimal effect on the activation profile (Supplementary figure 1). For both the VC and NV tissue conductivity models, the activation profiles from the fine resolution mesh and the cubic shape order models differed on average by less than one percentage point from the standard model, with the fine resolution model predicting slightly lower activation and the cubic shape order model predicting slightly higher activation. The ETI and dielectric dispersion models differed by as much as 2.62 percentage points on average from the standard model.

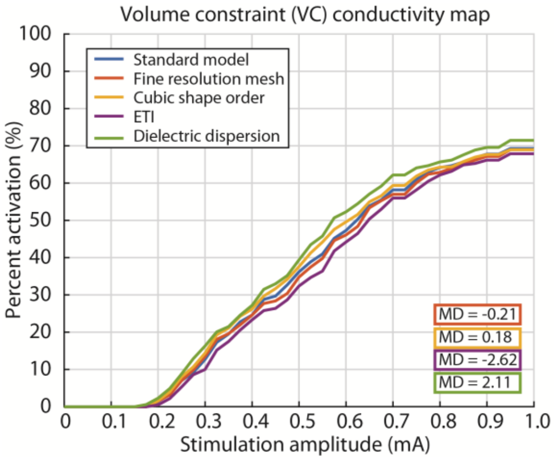

Supplementary figure 1. Activation profiles from models with varied complexity differed by up to 2.62 percentage points on average in comparison to the standard model.

Previous studies have evaluated the extent to which complexity affects model results and have concluded that highly complex models are necessary to achieve accurate results from models of DBS [118,194]. Examples of these highly complex models include those with higher order shape functions than what are mathematically required to solve the model [118], equivalent circuit models of the electrode tissue interface [118], and fully incorporated models of dielectric dispersion [191]. In such studies, error is commonly quantified with respect to the most complex model and using voltage predictions from the entire head or brain model or using a waveform reconstructed at a single point within the model. Calculations which use these techniques may generate measures of error that (1) are heavily biased by errors far from the stimulating electrode, (2) are too local and therefore not representative of error throughout the models, and (3) may have no bearing on the model outcome measure of interest, such as percent activation of a particular axonal pathway or VTA. Our results indicate that the general shape of percent activation curve for a population of axons within approximately 1 cm of the stimulating electrode was not affected by increasing model complexity by increasing mesh resolution, increasing shape order, including a model of the ETI, or including dielectric dispersion. Further, our results suggest that our standard model could have been further simplified by using a more coarse mesh.

In previous studies, it has been assumed that more complex models generate superior results [118,194]; however, variance in model outcomes must be considered in the context of the model goals, outcome measures, and the certainty of input parameters [86,181,203]. The simplest model we evaluated was selected as a reasonable predictor of the activation profile based on our findings that varying model complexity produced activation profile curves that were extremely similar in shape, and the range of values within the curves was approximately centered on the values predicted by the most simple model. Although these findings are specific to the models presented here, they have important implications. For example, assessing the precision of models, which use a similar framework where complexity is limited by computational resources and knowledge of electrode material properties, the former being highly relevant to models used in clinical practice and research studies that do not focus on model development.

3.8.Acknowledgements

This study was supported by the Michael J Fox Foundation; the National Institutes of Health (NIH grants R01-NS081118, R01-NS094206, and P50-NS098573); NSF-IGERT (Systems Neuroengineering, DGE-1069104); and an NSF-GRFP (00006595 to BT). We thank the Minnesota Supercomputing Institute for providing the computational resources. We also thank members of the University of Minnesota Neuromodulation Research and Technology Lab and University of Minnesota Neuromodulation Research Center for their technical support. BT thanks CT and BLT for their support during the preparation of this manuscript.

4. Computational modeling of endovascular DBS

Teplitzky BA, Connolly AT, Bajwa JA Johnson MD (2014) Computational modeling of an endovascular approach to deep brain stimulation. Journal of neural engineering, 11(2), 026011.

4.1.Overview

4.1.1. Objective

Deep brain stimulation (DBS) therapy currently relies on a transcranial neurosurgical technique to implant one or more electrode leads into the brain parenchyma. In this study, we used computational modeling to investigate the feasibility of using an endovascular approach to target DBS therapy.

4.1.2. Approach

Image-based anatomical reconstructions of the human brain and vasculature were used to identify 17 established and hypothesized anatomical targets of DBS, of which five were found adjacent to a vein or artery with intraluminal diameter ≥ 1 mm. Two of these targets, the fornix and subgenual cingulate white matter (SgCwm) tracts, were further investigated using a computational modeling framework that combined segmented volumes of the vascularized brain, finite element models of the tissue voltage during DBS, and multi-compartment axon models to predict the direct electrophysiological effects of endovascular DBS.

4.1.3. Main results

The models showed that: (1) a ring-electrode conforming to the vessel wall was more efficient at neural activation than a guidewire design, (2) increasing the length of a ring-electrode had minimal effect on neural activation thresholds, (3) large variability in neural activation occurred with suboptimal placement of a ring-electrode along the targeted vessel, and (4) activation thresholds for the fornix and SgCwm tracts were comparable for endovascular and stereotactic DBS, though endovascular DBS was able to produce significantly larger contralateral activation for a unilateral implantation.

4.1.4. Significance

Together, these results suggest that endovascular DBS can serve as a complementary approach to stereotactic DBS in select cases.

4.2.Background

The use of neuroendovascular techniques to deliver therapeutic electrical stimulation to deep brain structures has been proposed several times within the literature [204–207]; however, the feasibility of this technique has never been investigated in the context of known deep brain stimulation (DBS) targets and current state-of-the-art endovascular technology. Previous studies have established proof-of-concept demonstrations for navigating recording electrodes to cerebral capillaries in baboons [205] and humans [204]. A number of more recent studies have described recording neural activity using electrodes placed within larger vessels in the brain, including the middle cerebral artery [208–210], callosomarginal artery [210], basilar artery [210], middle meningeal artery [210–212], middle cerebral artery [209,210,213], and cavernous sinus [214,215]. Most recently, a study comparing endovascular sinus and subdural surface recording electrodes found similar results using the two modalities during seizure monitoring in an anesthetized swine model [62]. Endovascular electrodes have also been used to electrically stimulate cranial nerves, including the parasympathetic efferents of the vagus nerve from within the superior vena cava for cardiac rhythm management [216], and the phrenic nerve from within the brachiocephalic vein for respiratory maintenance [217]. Surprisingly, while many studies have focused on recording neural activity from within the vasculature, little is known about the mechanistic feasibility of electrically stimulating brain tissue using an endovascular electrode.

In this study, we developed a computational modeling framework to investigate the proximity of major blood vessels to known DBS targets and to estimate the intensity of stimulation necessary to modulate these DBS targets using endovascular electrodes. A three-dimensional reconstruction of the brain—including the parenchyma, vasculature, and ventricles—was coupled with a multi-compartment cable model of myelinated axons in the context of an inhomogeneous finite element model of the tissue voltage generated around a stimulating electrode [98,122,164]. Models of transvascular electrical stimulation were generated for two clinical DBS targets: (1) the fornix for memory disorders [218], and (2) the subgenual cingulate white matter (SgCwm) for treatment-resistant depression [219,220].

4.3.Methods

4.3.1. Human subject imaging

Retrospective data analysis was performed using anatomical T1-weighted magnetic resonance imaging (MRI) (Figure 24a) and gadolinium enhanced magnetic resonance angiography (MRA) (Figure 24b) from a single subject (51-year-old female). The subject's data showed no evidence of vascular damage/deformity in the deep cerebral veins or anterior cerebral arteries (ACAs); thus our analysis was constrained to these areas. Both imaging datasets were captured in the sagittal plane using a clinical 1.5 T scanner with slice thickness = 0.9 mm, field of view = 23 × 23 cm, matrix = 256 × 256 voxels.

Figure 24. Image alignment and reconstructed anatomical surfaces. Sagittal T1-weighted MRI from a single subject (a). Sagittal gadolinium contrast enhanced MRA (b) aligned by three-dimensional co-registration to the MRI. Surface reconstructions of the brain anatomy (c), including ventricles (green), cerebral veins and sinuses (blue), ACAs (red), cerebellum (orange), thalamus (yellow), and brainstem (pink), overlaid onto the MRI.

4.3.2. Anatomical surface reconstructions

Three-dimensional surface representations of the cranial anatomy were constructed for the purpose of generating axonal tracts and anatomically correct boundaries to regions with different electrical conductance values. In order to establish a common coordinate system for the entire analysis, the subject MRA was co-registered to the subject MRI in three dimensions. Surface representations of the ventricles and brain areas were reconstructed from the subject MRI in reference to the Mai human brain atlas [221] and surface representations of the cerebral veins and arteries were reconstructed from the MRA in reference to the Cerefy human cerebral vasculature atlas [222]. All surfaces were constructed using Mimics Innovation Suite (v15.0, Materialise, Leuven, Belgium). Image resolution enabled reconstruction of cerebral vasculature ≥1 mm in diameter. Surface reconstructions of the cerebral veins, arteries, ventricles, and brain regions were combined into a single three-dimensional anatomical model (Figure 24c).

4.3.3. Electrode construction and placement

Three-dimensional electrode models were digitally constructed and oriented within the anatomical model using Rhinoceros3D (v4.0, McNeel, Seattle, WA). An endovascular guidewire electrode, a compliant endovascular ring-electrode, and a clinical DBS lead were investigated. The cylindrical (diameter = 0.127 mm; length = 1 mm) guidewire electrode was constructed to model the exposed metallic tip of a 4 French (Fr) endovascular guidewire. An annular ring-electrode, which was morphed to the retaining vessel shape, was constructed (0.5–4.5 mm length; 0.1 mm wall thickness) to model a compliant endovascular snare or tightly meshed stent-style electrode. Only the macro features of each electrode were modeled. The primary coils of a guidewire, the primary coils of a snare, and the individual struts of a stent were not modeled because two-dimensional simulations incorporating these fine features showed the effect to be negligible in the tissue conductance model solution. In each rendition, the stimulating surface of the endovascular ring-electrode was created by sectioning and radially scaling the internal wall of the encapsulating vessel to 75% of its original diameter. This method produced electrodes that maintained the intraluminal shape of the surrounding vessel and that could be nested within the finite element mesh used to calculate the tissue voltage during stimulation. Because the model electrodes were inspired by actual endovascular devices, the surface areas of each electrode were not equal. The clinical DBS lead model was designed to replicate the quad-contact 3387 DBS lead (Medtronic Inc., Minneapolis, MN) with an electrode contact diameter of 1.27 mm, length of 1.5 mm, and inter-electrode spacing of 1.5 mm.

Model fornix and SgCwm tracts were targeted bilaterally using both endovascular and stereotactic approaches. Endovascular electrodes targeting fornix and SgCwm were positioned within the ipsilateral internal cerebral vein (ICV) and the ipsilateral A2 segment of ACA, respectively. For both endovascular targets, the electrode was initially placed within the vessel at the midpoint of the shared vessel/target border. Clinical DBS leads targeting the SgCwm were introduced through the superior frontal gyrus along a slight lateral to medial paracoronal trajectory [219]. For this trajectory, the active contact resided at the sagittal midpoint between the anterior commissure and the anterior aspect of the genu of the corpus callosum. Clinical DBS leads targeting the fornix were introduced through the superior frontal gyrus and lateral ventricles parallel to the anterior aspect of the fornix such that the ventral tip of the lead lay in close proximity to optic tract [218]. In this trajectory, the lead was external to the fornix and the three most ventral contacts were at equal distances from the target. The two most ventral contacts were in, or in close proximity to, the hypothalamus, and the more dorsal of the two center contacts was set as the active contact.

4.3.4. Axon models

Bilateral surface reconstructions of the fornix and SgCwm tracts were independently populated with 400 three-dimensional, multi-compartment axon cable models [75]. Axon geometries were bound by contours generated from cross-sections of the anatomical MRI reconstructions of each target. Each contour was populated with 500 uniformly distributed seed points using a Jordan curve algorithm [223], and the closest points from adjacent contours were connected using a nearest neighbor algorithm [87] in Matlab (vR2011b, Mathworks, Natick, MA). Fornix axon seed points were bounded by 16 contours (~1 mm separation) along the axial centerline of the tract in each hemisphere. In fornix only, axons were allowed to cross hemispheres to reflect anatomy described in retrograde labeling studies [224]. SgCwm axon seed points were bounded by five parasagittal contours (1 mm separation) in each hemisphere. Spline fits were applied to each set of connected points resulting in 500 three-dimensional traces, of which the 400 shortest length splines were used to create axon cable model compartments. The 2 µm diameter myelinated axon cable model consisted of nodes of Ranvier, myelin attachment segments, paranode main segments, and internode segments with each compartment connected through an axial resistance. These axonal equivalent circuit models included membrane capacitance, linear leakage properties, and nonlinear sodium and potassium conductances that were consistent with previous studies [96,98–100,122,164].

4.3.5. Predicting tissue voltage during DBS

Separate three-dimensional tissue conductance models of the brain were developed for each simulation. Anatomical surface reconstructions of the cerebral vasculature, ventricles, electrodes, and an implantable pulse generator (IPG) were nested within a cylindrical boundary (radius = 30 cm; height = 55 cm) and combined to form a single non-manifold assembly surface mesh. The model IPG was a 76 × 61 × 13 mm3 rectangular cuboid with rounded edges and was centered 33 cm below and 3.75 cm to the right of the geometric center of the head model. The resulting nested surface mesh was transformed to a volumetric mesh of tetrahedral elements using 3-Matic (Materialise Inc., Leuven, Belgium). Depending on electrode complexity, each volumetric mesh consisted of between 95,300 and 115,000 elements, with finer resolution near the electrode surface and more coarse resolution near the model perimeter. The conductance of blood, cerebrospinal fluid (CSF) and bulk tissue were modeled as 0.7 S/m [82] , 1.8 S/m [183], and 0.3 S/m [79,80], respectively. The model assumed ideal electrode behavior, isotropic conductances, and linear scaling of electric potentials in the tissue. Voltage sources were specified at the surface of each electrode and the IPG surface was set to ground while the outer surface of the bounding cylinder was assigned the condition of zero-flux. The tissue voltage solution (Figure 25a) for each electrode configuration was calculated by solving Poisson's equation using the finite element method (FEM) with Comsol Multiphysics (v4.0a, Comsol Inc., Burlington, MA).

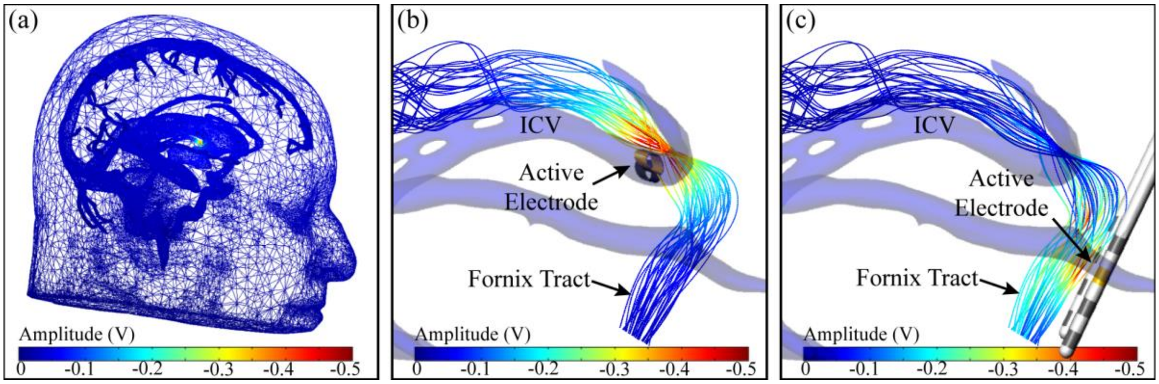

Figure 25. Modeling tissue and extracellular axonal cable model voltages during DBS. The FEM tissue voltage solution superimposed onto the anatomical surface mesh of the cranium, ventricles, and major blood vessels from 1 V stimulation applied across an endovascular ring-electrode in the ICV (a). The FEM solution from (a) superimposed onto a bilateral subpopulation (20/400) of model axons representing the fornix tract (b). The FEM solution from 1 V applied across a single contact of a clinical DBS lead targeting the fornix superimposed onto a bilateral subpopulation (20/400) of model axons representing the fornix tract.

4.3.6. Predicting axonal responses to DBS

Thresholds for driving axonal action potentials were calculated using the Neuron v7.2 programming environment [124]. Each axonal compartment of each axon was perturbed using the inserted extracellular mechanism by driving the variable, *e_extracellular* with the calculated peri-stimulation extracellular membrane potential. Conductance values required for the application of extracellular stimulation in this manner were assigned values consistent with previous work [122]. The applied extracellular membrane potential was consistent with a 130 Hz voltage-controlled stimulation waveform and scaled according to the FEM solution (Figure 25b and c). The voltage waveform was derived from an experimental recording of a voltage-controlled IPG (Medtronic, Minneapolis, MN), which exhibited a charge-balanced 90 µs cathodic pulse followed by a 400 µs interphase delay and a 3 ms anodic pulse. Electrical capture of axonal output with DBS was defined by axonal action potentials occurring within $1-3$ ms following the application of the stimulus with a probability ≥ 0.8. The percentage of the neural population activated by stimulation amplitudes between 0 and 10 V was calculated at 0.125 V increments and used to generate an activation profile for each simulation.

Activation plots were calculated for unilateral and bilateral stimulation of each target using both endovascular electrodes and stereotactic leads for delivering DBS.

4.4.Results

4.4.1. Endovascular stimulation targets

Seventeen known or hypothesized therapeutic targets for DBS were investigated in the context of the human neural vasculature. For each target, adjacent blood vessels with intraluminal diameters of ≥1 mm (Table 7) were identified using a three-dimensional atlas [222] of idealized cerebral blood vessels joined with T1-weighted anatomical MRI from a single subject. No large cerebral arteries or veins (≥1 mm diameter) were found directly adjacent to the following 12 targets: anterior limb of the internal capsule, centromedian/parafasicularis nucleus of the thalamus, globus pallidus internus, hippocampus, hypothalamus, inferior thalamic peduncle, lateral habenula, periaqueductal gray/periventricular gray, subthalamic nucleus, ventralis caudalis nucleus of the thalamus, ventrolateral intermedus nucleus of the thalamus, and the ventral posterolateral/ventro-posteromedial nucleus of the thalamus. Either the ICV or the A1/A2 segments of the ACA were found to directly border some aspect of the remaining five targets (Table 7). The dorsal aspect of the ICV was found to border the ventral aspect of the ipsilateral fornix, and the ventral aspect of the ICV was found to border the dorsal aspect of the ipsilateral anterior nucleus of thalamus. The dorsal border of the A1-ACA was found to border the ventral aspect of the ipsilateral nucleus accumbens and the A2-ACA was found to border the medial aspect of the subgenual cingulate and ventral capsule.

Table 7. Adjacent blood vessels to known and putatively therapeutic DBS targets.

Targeted neural region	Clinical disorder(s) [13–17]	Adjacent blood vessels [222]	Intraluminal vessel diameter [222] (mm)
Anterior limb of the internal capsule	TRD, OCD	-	
Anterior nucleus (Thal.)	Epilepsy	ICV	0.4-1.4
Centromedian/parafasicularis (Thal.)	PD, ET, TS, Epilepsy, DoC	-	
Fornix	AD	ICV	0.4-1.4
Globus pallidus internus	PD, dystonia, TRD, TS	-	
Hippocampus	Epilepsy	-	
Hypothalamus	Aggressive behavior, obesity, AM	-	
Inferior thalamic peduncle	TRD, OCD	-	
Lateral habenula	TRD, obesity, AM	-	
Nucleus accumbens	TRD, OCD, addiction, obesity,AM	A1-ACA	2.2-2.6

Periaqueductal gray/periventricular gray	Chronic pain	-	
Subgenual cingulate white matter	TRD	A2-ACA	1.9-2.2
Subthalamic nucleus	PD, dystonia, TRD, OCD, epilepsy	-	
Ventralis caudalis nucleus (Thal.)	Chronic pain	-	
Ventral capsule	OCD	A2-ACA	1.9-2.2
Ventrolateral intermedus (Thal.)	ET	-	
Ventral posterolateral/ventro-posteromedial (Thal.)	Chronic pain	-	

A1 = A1 segment and A2 = A2 segment of the ACA = anterior communicating artery, AD = Alzheimer's disease, AM = anorexia mentosa, ICA = internal carotid artery, ICV = internal cerebral vein, Thal. = thalamus, TRD = treatment resistant depression, OCD = obsessive-compulsive disorder, PD = Parkinson's disease, ET = essential tremor, TS = Gilles de la Tourette Syndrome, DoC = disorder of consciousness.

4.4.2. Endovascular navigation to the fornix and SgCwm

Theoretical endovascular implantation paths from the internal jugular to the ICV (to stimulate fornix) and from the internal carotid artery to the A2-ACA (to stimulate SgCwm) were characterized using the Cerefy human cerebral vasculature atlas [222]. Overall path length, vessel branching angles, and intraluminal vessel diameters were measured for right-sided endovascular access to each target. Fornix and SgCwm were selected for further investigation because (1) each is directly adjacent to a ≥1 mm diameter vessel, (2) each has shown potential efficacy in long-term (≥12 month) clinical trials [218,225], (3) together they include both venous and arterial approach paths, and (4) they present two extremes of relative axon-to-vessel angle.

The approach path to fornix was characterized by navigation through the right internal jugular vein, sigmoid sinus, transverse sinus, straight sinus, great cerebral vein of Galen, basal vein, and terminated in the ICV (Figure 26a, left). This implantation path would involve maneuvering through the large diameter, yet highly tortuous, sigmoid sinus and through four obtuse branching angles. The proposed electrode target was within a 1 mm diameter section of the ICV at the most anterior aspect of the shared ICV/fornix border (Figure 26a, right). At the site of the endovascular electrode implantation, the right ICV also bordered the ventral edge of the interventricular foramen and the dorsomedial aspect of the anterior thalamus. The approach path to SgCwm was characterized by navigation through the right internal carotid artery, A1-ACA, and terminated in the A2-ACA. Catheterization of the A2-ACA would require maneuvering through the tortuous carotid artery and two slightly obtuse branching angles (Figure 26b, left). The proposed electrode target was within a 2 mm diameter section of the A2-ACA just beneath the genu of the corpus callosum (Figure 26b, right).

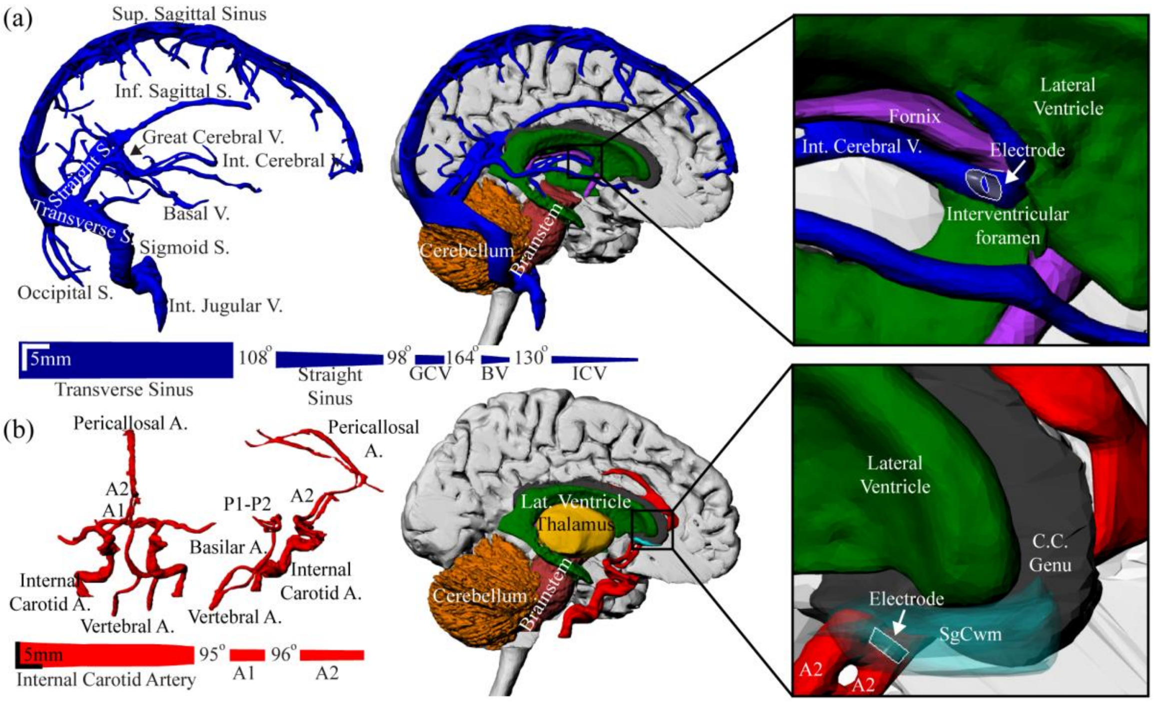

Figure 26. Endovascular targeting of the fornix (a) and SgCwm (b). Vascular reconstructions with estimated path length, vessel diameter, and vessel branching angles (left). Combined vascular and brain reconstructions (center). Ring-electrode model implant location (right).

4.4.3. Optimizing model features and electrode geometries

Pilot simulations were run to evaluate model sensitivity to tissue conductance homogeneity and multi-compartment axon population size. For endovascular stimulation, the addition of blood to an otherwise homogenous bulk neural tissue conductance model resulted in activation of an additional 5–25% of the axonal population. The inclusion of CSF resulted in activation of an additional 2–20% of the axonal population for fornix and resulted in no change in the activation profile for SgCwm. For stereotactic DBS, the predicted activation was not affected by the inclusion of blood or CSF in the tissue conductance model. Sensitivity to the number of axons for each target was evaluated by quantifying activation using 100, 200, 300, 400, and 500 axons in the model. For both targets, the amplitude-dependent activation predictions differed by ≤5% of the total population for models containing 300, 400, or 500 axons. Final model parameters included inhomogeneous tissue conductance models consisting of bulk neural tissue, blood, and CSF with 400 multi-compartment axons per target, per hemisphere.

Transvascular electrical stimulation from endovascular electrodes that utilized passive radial force for securing contacts against the vessel wall have been shown experimentally to drive behavioral effects with lower stimulation amplitudes in comparison to guidewire electrodes [226]. To evaluate this effect for endovascular SgCwm and fornix stimulation, model predictions of neural activation were calculated for ring-electrodes and free-floating guidewire electrodes at stimulation amplitudes from 0 to 10 V. Endovascular electrodes targeting SgCwm and fornix were positioned within the ipsilateral A2-ACA and the ipsilateral ICV, respectively, at the midpoint of the shared vessel/target border. Predicted activations were calculated using a 1 mm long endovascular ring-electrode and 1 mm long guidewire electrode, placed at five different locations within the target vessel (Figure 27). The model-predicted activation from an endovascular ring-electrode was consistently higher than guidewire electrodes in both targets. In SgCwm, predicted activation from guidewire electrodes increased with stimulation amplitude, but at a slower rate in comparison to the ring-electrode. The predicted SgCwm activation increased at approximately the same rate for each guidewire electrode. Guidewire stimulation activated axons at lower amplitudes for electrodes placed closer to the neural target (Figure 27a). In fornix, the predicted activation from the ring-electrode increased sharply between 1 and 2 V and increased at a slower rate between 2 and 10 V (Figure 27b). The activation profile of the guidewire nearest to the fornix mimicked that of the ring-electrode, with a sharp increase between 2 and 4 V and slower increase between 4 and 10 V. The models predicted much lower levels of activation from all other guidewire electrodes targeting fornix.

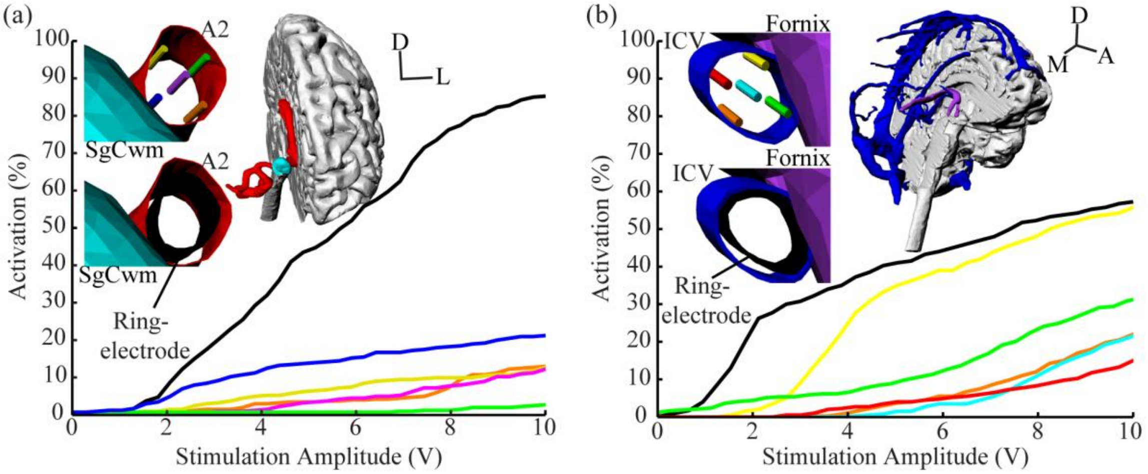

Figure 27. Ring-electrodes produced higher estimates of axonal activation than guidewire electrodes. Stimulation through a ring-electrode within the right A2-ACA produced approximately four times greater activation in the right SgCwm than guidewire electrodes for stimulation at high amplitudes (a). Stimulation through a ring-electrode within right ICV produced approximately two times greater activation in the right fornix than guidewire electrodes for stimulation at high amplitudes through all electrodes but the most dorsal, which produced nearly equivalent levels of activation for amplitudes beyond 4 V (b).

Previous modeling work has shown electrode length to be an important factor for optimizing the volume of tissue activated by DBS [227]. To evaluate the effect of electrode length in endovascular stimulation in these two targets, model predictions of neuronal activation of SgCwm and fornix were calculated for ring and guidewire electrodes measuring 0.5, 1.5, 2.5, 3.5, and 4.5 mm in length at stimulation amplitudes between 0 and 10 V. For all electrodes, the longitudinal midpoint was centered at the midpoint of shared vessel/target border, and guidewire electrodes were placed along the intraluminal wall closest to the shared vessel/target border (Figure 27a blue, Figure 27b yellow). Stimulation through longer electrodes yielded a ≤10% increase in the predicted levels of activation in both targets across the stimulation amplitude range (Figure 28).

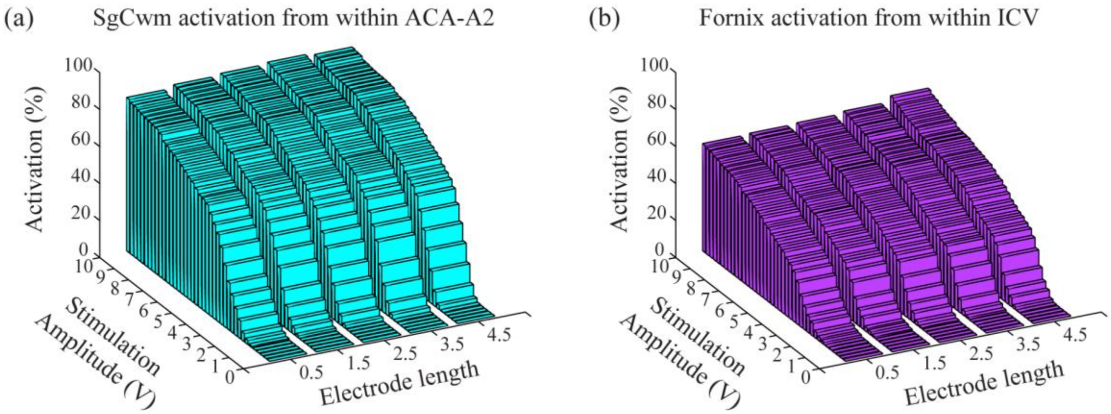

Figure 28. Endovascular ring-electrode length effect on predicted neural activation of the SgCwm (a) and fornix (b).

Precise lead implantation is known to be vital for delivering therapeutic stereotactic DBS. To determine the optimal location within each target vessel for delivering endovascular DBS, and to evaluate neural activation sensitivity to sub-optimal endovascular electrode placement, the location of a 1 mm long endovascular ring-electrode was systematically varied in 1 mm increments along the target vessel length from 5 mm posterior/ventral to 5 mm anterior/dorsal to the midpoint of the shared vessel/target border. Predictions of neural activation were generated at stimulation amplitudes between 0 and 10 V for each target at each location. For both targets, the models predicted the optimal ring-electrode placement to be anterior to the midpoint of the shared vessel/brain target border and that 1 mm deviations from the optimal location resulted in a minimal reduction in the predicted activation (Figure 29). For the SgCwm, the highest levels of activation were achieved using electrodes placed 0–2 mm dorsal to the midpoint of the shared vessel/brain target border. For the fornix, the optimal location was 3–4 mm anterior to the midpoint of the shared vessel/brain target border. Fornix stimulation at this placement involved delivery of current through the CSF-filled intraventricular foramen (Figure 26a). In both targets, across the entire stimulation amplitude range, placement of the endovascular electrode 1 mm away from the optimal location decreased the predicted neuronal activation by 1–10% of the total population, and placement 5 mm away from the optimal location decreased the predicted neuronal activation by 30–60% of the total population.

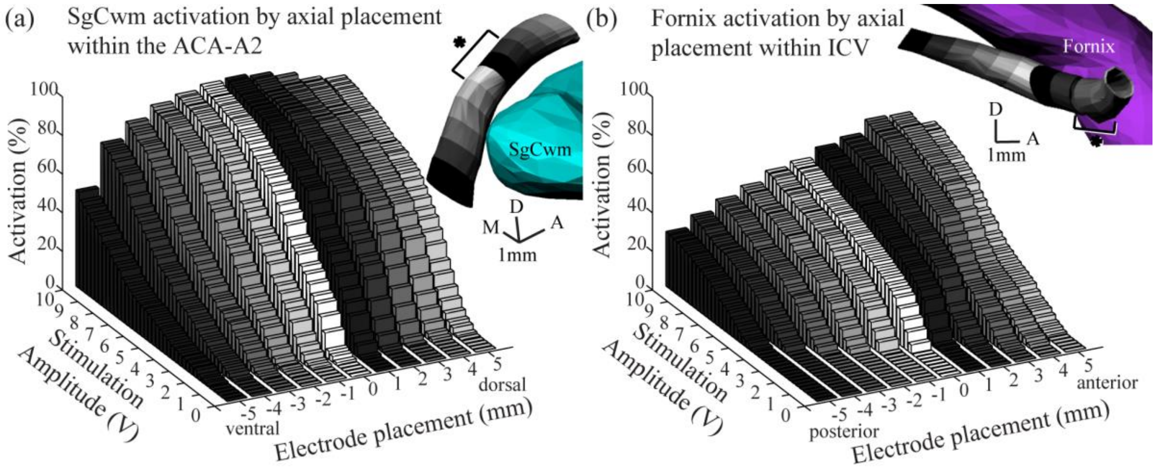

Figure 29. Endovascular ring-electrode placement effect on predicted neural activation of the SgCwm (a) and fornix (b). Asterisks (*) indicate optimal axial placements.

4.4.4. Comparing endovascular DBS to stereotactic DBS

To compare endovascular to stereotactic DBS, endovascular ring-electrodes and stereotactic DBS leads were placed within the model and stimulation was delivered using both unilateral and bilateral configurations. Ring-electrodes were placed anterior to the midpoint of the shared vessel/target border, in accordance with previous model predictions of optimal placement (Figure 30a and b, left). Stereotactic DBS leads were placed along the clinical implantation trajectory described previously (Figure 30a and b, right).

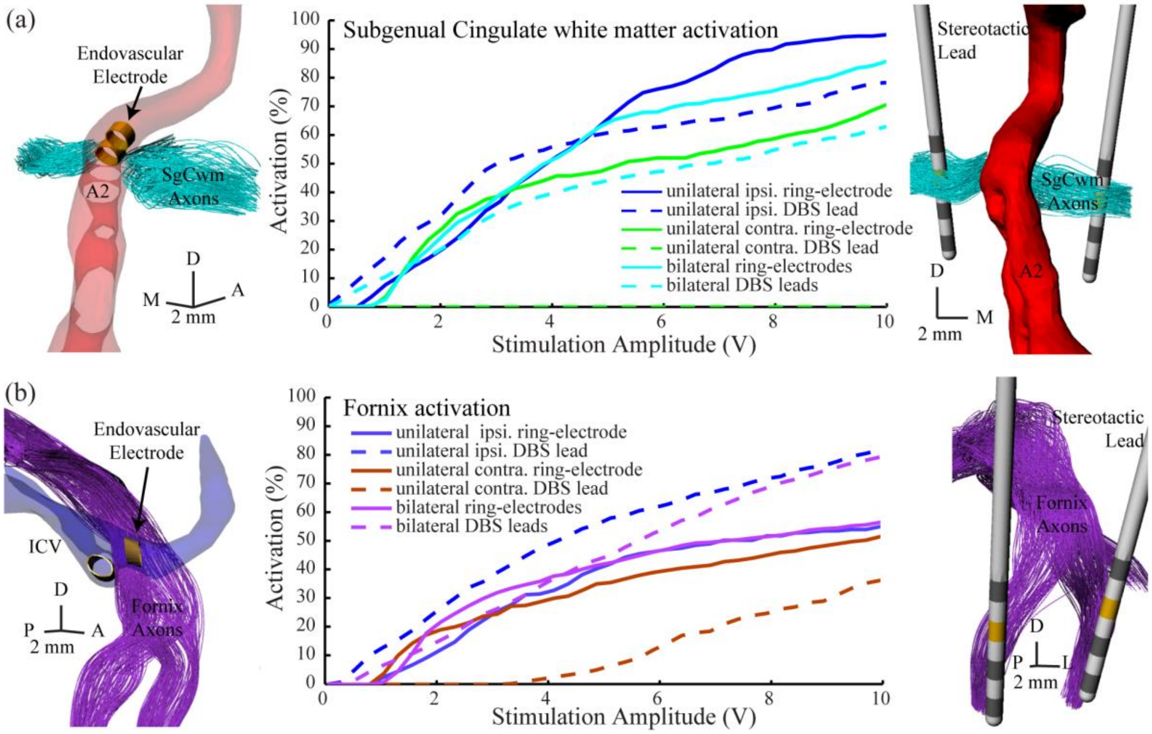

Figure 30. Comparison of predicted neuronal activation for stimulation delivered using unilateral and bilateral endovascular ring-electrodes (left) and stereotactic leads (right). Activation profiles for all stimulation configurations (center) were predicted for the SgCwm (a) and fornix (b).

For SgCwm, unilateral stimulation through an endovascular ring-electrode activated 10% less of the neuronal population than unilateral stimulation through the stereotactic DBS lead at low amplitudes, but activated 10% more of the neuronal population at high amplitudes, with an inversion in the activation profiles occurring at 4.25 V. With the endovascular electrode, the contralateral SgCwm was also activated, but at 10% less of the total population than the ipsilateral SgCwm. Contralateral activation was not achievable with a stereotactic DBS electrode (Figure 30a). At amplitudes below 1.25 V, bilateral stereotactic DBS activated a larger portion of the neural population than bilateral endovascular DBS. Above 1.25 V, however, bilateral endovascular stimulation activated 10–30% more of the total population than bilateral stereotactic DBS.

In the fornix, unilateral stereotactic DBS activated 10–30% more of the ipsilateral neuronal population than did unilateral endovascular stimulation across the 0–10 V range. Unlike in the SgCwm, unilateral stereotactic DBS activated a small portion of the contralateral fornix axons at large amplitudes, and remained significantly lower than the activation resulting from unilateral endovascular DBS. Neuronal activations from bilateral stimulation were comparable between endovascular and stereotactic DBS at amplitudes below 5 V. Above this threshold, stereotactic DBS activated more of the neural population than endovascular stimulation.

4.5.Discussion

This study provides a theoretical foundation for evaluating an endovascular approach to targeting DBS therapy. The purpose was to formally examine the feasibility of using an endovascular approach to implant electrodes within two vascular targets to modulate neural activity in nearby brain regions: the fornix and SgCwm, both of which are current targets of stereotactic DBS therapies.

4.5.1. Opportunities for neuroendovascular targeting

Neurovascular disorders including intracerebral aneurysm and ischemic stroke are routinely treated with endovascular techniques that deliver conductive devices, such as platinum aneurysm coils, Nitinol stents, and tungsten snares for mechanical occlusion or recanalization of the neural vasculature [228]. In these procedures, wire-guided microcatheters under fluoroscopic navigation enable device deployment to sub-millimeter diameter cerebral blood vessels by way of tortuous implantation trajectories in the presence of acute branching angles [229]. Several of these vascular targets are noteworthy given their proximity to established and investigational targets of DBS therapy. For example, the anterior communicating artery (ACoA), which demarcates the A1 and A2 segments of the ACAs, is a common target of neuroendovascular intervention that necessitates a complex implantation path [230], and it lies just proximal to the A2 segment of the ACA, the proposed vascular target for delivering endovascular DBS to the SgCwm. The ACoA has an intraluminal diameter of approximately 1 mm [231] and current technologies in endovascular intervention allow for catheter-based implantation of devices such as aneurysm coils, stents, and balloons into this target [232–234]. Delivery of a coil- or stent-shaped electrode into the A2 segment of the ACA would require navigation through or around the ACoA to a point with an approximately equal diameter that is approximately 2 cm distal to this more conventional target. To our knowledge, device implantation to within the deep cerebral veins, including the ICV, has not been described within the clinical literature. However, endovascular thrombolysis for the treatment of deep cerebral vein thrombosis involves catheter navigation to the straight sinus and/or great cerebral vein of Galen [235–239], 2–3 cm proximal to the ICV. Neuroendovascular navigation to deep cerebral veins may increase risk due to veins generally having thinner walls than arteries [240]; however, current technologies enable device implantation to arteries with equivalent diameters [233,241]. Navigating endovascular devices to neurovascular targets that are several centimeters distal to commonly catheterized vessels may increase targeting complexity, require novel designs for endovascular devices, and carry higher risk for some patients.

4.5.2. Transvascular stimulation feasibility

Although limited, in vivo demonstrations have established feasibility for delivering transvascular electrical stimulation. Direct, low frequency vagal nerve electrical stimulation (20 Hz) has been shown to induce acute bradycardia in humans [242–246], and subsequent studies have reproduced this effect with transvascular stimulation in canine and porcine models [247,248]. These studies show comparable degrees of cardiac modulation through direct vagal nerve stimulation using a nerve-cuff and transvascular vagal nerve stimulation using a multipolar diagnostic catheter. Studies investigating endovascular electrode design factors evaluated the use of a basket electrode [249–252] and a flexible-loop electrode lead [226,253]. They found that transvascular stimulation thresholds for modulating neural activity could be greatly reduced by using bipolar stimulation from electrodes that conform to the vessel wall, in comparison to monopolar stimulation delivered through a guidewire or diagnostic catheter, thus minimizing electrode-to-target proximity and securing the electrode within the vessel.

4.5.3. Electrode design for neuroendovascular stimulation

Our comparison of guidewire electrodes placed at different radial positions within the vasculature confirmed that target-to-electrode proximity plays a large role in neural activation thresholds. This result is somewhat surprising, considering that the relatively high conductive environment of the blood could cause the voltage distribution within the vessel to be relatively uniform. These results indicated that electrical stimulation in the presence of blood and blood vessel walls may not differ fundamentally from intra-parenchymal stimulation, and principles such as current steering may apply to transvascular electrical stimulation in the same manner as stimulation through stereotactically-placed DBS leads [87,100]. The models also indicated that, in comparison to guidewire electrodes, a ring-electrode ensured close proximity to the neural target and allowed for lower stimulation charge densities given the ring-electrode's larger surface area. Existing stents and some snare designs would fall into such a category [254].

When designing electrodes for endovascular DBS, several other specifications must be considered, given that the human neurovasculature is replete with small vessel diameters, tortuous vessels, and acute vessel branching angles that can impede navigation and deployment of endovascular devices. The models showed that, assuming a vascular implant position proximal to the neural target, increasing the length of the ring-electrode did not have a significant effect on neural activation thresholds. This is noteworthy because longer electrodes impose challenges with navigability through tortuous vessels. While shorter length designs provide similar activation levels to longer ones, misplacement due to migration of the electrode along the vessel, larger charge densities due to smaller surface area, and higher neural activation threshold sensitivity to off-target implantations may limit practical implementation of small device length designs. Though not specifically modeled in this study, mechanical and electrochemical material properties of endovascular devices, as well as their ability to migrate into the intimal layer of the vessel, will also have important implications in terms of electrode material sustainability and biocompatibility [255,256].

4.5.4. Comparison to current stereotactic DBS procedures

The model simulations also compared stimulation threshold amplitudes between endovascular and stereotactic DBS, showing comparable thresholds for unilateral DBS cases and potential for significant contralateral activation with unilateral endovascular

DBS cases targeting midline structures. Bilateral activation from unilateral stimulation could be advantageous because it would reduce potential complications resulting from implantation of two devices. While the target areas modeled in this study were limited to midline structures in close proximity to vessels with intraluminal diameters ≥1 mm, other targets may be accessible provided that neurovascular targeting techniques are advanced; however, charge density limits with small endovascular electrodes may limit the overall volume of tissue activation and therefore reduce the ability to deliver effective therapy with stimulation.

The low surgical complication rates for stereotactic DBS [257] reflect years of experience perfecting the surgical procedure and the strict patient selection criteria. Indeed, complications associated with craniotomy, meningeal damage, micro bleeds, ventricular penetration, and risk of severe hemorrhage can disqualify patients from surgical candidacy. Risk factors for the occurrence of hemorrhage in DBS surgery have been studied extensively and are correlated with the use of microelectrode recording, sulcal incursion, and breaching the ventricular walls during implantation [36–41]. The reported symptomatic effects of clearly observable vascular events following DBS surgery include increased relative risk of post-operative seizure [42], permanent neurological deficit [43], post-operative confusion [44], and subsequent extended hospital stays [45]. Reports on the symptomatic effects of small bleeds exist, but remain difficult to interpret as small bleeds are likely underreported [38] due to a lack of blood-sensitive pre- and post-operative imaging [36,46]. Increased risk of hemorrhage has been shown to vary across anatomical targets [51,52] and may relate to lead trajectory and target proximity to large blood vessels. For example, GPi-DBS for PD carries a higher risk of hemorrhage than STN-DBS [52–54,258] and this may be related to the close proximity of the A1 segment of the ACA to the ventral border of GPi. Alternatively, reports of cognitive complications with STN-DBS are higher in comparison to GPi-DBS and are correlated with the use of transventricular [44] and transcaudate [259] lead implantation trajectories.

For those cases that do not fit the selection criteria for stereotactic DBS or that seek to target heavily vascularized brain regions, endovascular DBS approaches may provide a suitable alternative. However, further study is needed to evaluate risks associated with endovascular targeting procedures, including vessel wall damage, vasospasm, occlusion, and hemorrhage. While there is the possibility that thrombosis and vasoconstriction could occur with electrical stimulation [260], some studies have shown that cathodic electrical stimulation can prevent thrombosis formation due to the effect of the applied negative charge on blood cells [261,262]. Since the clinical DBS waveform utilizes a large amplitude cathodic pulse followed by a low amplitude anodic pulse, the likelihood of stimulation-induced clot formation may not be significant, but still needs to be verified.

4.5.5. Model limitations

The computational modeling approach used here made several assumptions worth discussing. While the reconstructions were specific for the two DBS targets, anatomy of the cerebral veins, arteries, and sinuses can differ significantly among subjects [263–267]. While our models showed that inhomogeneity of the vessel wall did not have a large effect on the parenchymal tissue voltage during endovascular DBS, studies performing simultaneous subdural and endovascular EEG from within arteries and venous sinuses suggest that the vessel wall acts as a low-pass filter but does not completely attenuate high frequencies [62,209,214,215]. The traditional DBS tissue conductance model did not include the low conductance encapsulation tissue which can reduce the volume of tissue activated by up to 50% [91]. Also, because diffusion tensor MRI was not available in the patient data, anisotropic conduction was not included in the tissue conductance model. The effect of higher conduction along the fiber tracts is difficult to estimate in general terms; however, based on the axon-to-electrode orientation slightly lower than predicted voltages would likely occur within the fornix tract and slightly higher than predicted voltages would occur within the SgCwm. Additionally, the absolute neural activation percentages calculated by the models are based on the excitability of multi-compartment axons, which are in turn determined by model parameter assumptions [96,268] that do not fully represent the true diversity of neuronal membrane dynamics and cellular morphologies.

Scaling of the ring-electrode was also required in order to properly generate an inhomogeneous mesh with which to perform the finite element modeling. In reality, a stent would tightly conform to the vessel wall, securing it in place and reducing the electrode-to-target proximity. The modeling of the ring-electrode in this study did not include the mesh structure of a stent that would be required for insertion using an endovascular technique or the primary coils of an endovascular snare that would increase the electrode surface area. Modeling these features in a two-dimensional setting, we found that due to the high conductance of blood and the reduction in the scaling of the stent-electrode, the effects of the lattice structure and primary coils were negligible. Even so, it is worth noting that a stent-electrode with a large free cell area may result in higher charge densities at the lattice struts.

4.6.Conclusions

Endovascular delivery of DBS electrodes may provide a complementary technique for treating a number of neurological disorders. This study investigated endovascular DBS through a computational modeling approach. The models predicted that activation of neural targets using an endovascular device is feasible using current catheter technology for midline thalamic and cortical targets. In comparison to endovascular guidewire designs, endovascular ring-electrode designs were found to allow for reduced electrode-to-target distance, more robust anchoring to the vessel wall, and increased predicted levels of neural activation. Using endovascular ring-electrodes to target specific neural structures (fornix and SgCwm), the models predicted neuronal activation comparable to that achieved following stereotactic DBS implantation, suggesting further research in this alternative targeting strategy for clinical DBS applications.

4.7.Acknowledgments

This study was supported by the College of Science and Engineering, Institute for Translational Neuroscience at the University of Minnesota, R01-NS081118, NSF-IGERT (Systems Neuroengineering, DGE-1069104), and NSF-GRFPs (00006595 to BT and AC). We thank Fareed Suri and Adnan Qureshi for the imaging data and the Minnesota Supercomputing Institute (MSI) for the computational resources.

5. Conclusions and future directions

Deep brain stimulation is a valuable therapy that provides to the means to target specific brain regions and disrupt pathologic activity. In the US, DBS is currently approved or granted exemption for the treatment of four disorders. However, ongoing studies are exploring many more applications and brain targets for DBS. These investigational applications are primarily composed of treating disorders for which medication is ineffective or not well tolerated by patients. In such cases, neurosurgical intervention could greatly benefit patient quality of life by reducing symptoms and improving the efficacy of pharmaceutical intervention, as is the case for DBS to treat Parkinson's disease. Successful implementation of DBS relies on the precise placement of stimulating electrodes within small and deep brain structures.

Studies investigating complications associated with DBS have established suboptimal lead placement and lead migration to occur at a rate somewhere between 1-5% [269–272]. However, the vast majority of these analyses are performed at academic centers by clinicians who specialize in DBS. In a recent study, which analyzed complication rates between 2004 and 2013 using data from the Centers for Medicare and Medicaid Services and the National Surgical Quality Improvement Program, it was estimated that 15-34% of DBS procedures were performed for the purpose of revising the lead placement or lead removal [273]. The authors highlight the contrast between the occurrence of suboptimal placement within academic centers and the nationwide occurrence. These data suggest that suboptimal lead placement is, by far, the most prevalent complication in DBS. Additionally, these data suggest that this complication rate is likely to increase over time due to the increasing popularity and applications of DBS and due to an increase in the number of non-academic clinical practices performing DBS surgery. For these reasons it is imperative that next-generation DBS technology be able to compensate for suboptimal lead placement, or be delivered using novel methods that improve targeting success. Computational models of DBS can facilitate the process of designing and evaluating next-generation DBS technologies by enabling high-throughput studies which explore the impact of changing lead design features within a large design feature parameter space.

Models can also generate predictions of stimulation efficacy and be used to guide programming of next-generation DBS technologies which may offer an increasingly complex assortment of stimulation configurations.

This thesis leverages computational modeling to prospectively evaluate novel electrode designs and to retrospectively evaluate model parameters in the context of experimental data. These studies show how independent current controlled stimulation with advanced machine learning algorithms can negate the need for highly dense DBS arrays to shift, steer, and sculpt regions of modulation within the brain. Additionally, these studies show that while advanced and personalized computational models of DBS can predict many of the behavioral and electrophysiological outcomes of DBS, there are remaining inconsistencies that suggest there are additional physiological mechanisms of DBS that are not yet well understood. Finally, the results show how computational models can be beneficial for prospective development of novel approaches to neuromodulation prior to large-scale preclinical and clinical studies.

5.1.Designing deep brain stimulation arrays

In the past five years, several novel DBS array designs have entered clinical trials. These innovative designs and clinical trials are motivated by the need for DBS leads that can radially steer current in order to compensate for suboptimal lead placement. Recent publications describing clinical demonstrations using DBS arrays have shown improved short-term outcomes in single patients [110,112]. However, studies have not demonstrated that current DBSA designs are optimal, nor have studies demonstrated that any single design is maintains equivalent efficacy when used to target brain regions with different geometry and cellular makeup. The computational modeling study in chapter 2 takes a first step toward optimizing DBSA lead design by comparing electrode charge storage capacity, electrode charge injection limit, and radial steering capacity for DBS leads and DBS arrays with different numbers of electrodes. In this study, radial steering capacity was evaluated using groups of electrodes in a single plane within a population of lead-parallel axons. A natural extension of this work to be considered in future studies is the ability of DBSA leads with different designs to steer current in three-dimensions in the context of specific brain targets with anatomically correct electrical properties and distributions of cells and fiber pathways. This work also demonstrated the successful classification of stimulation settings using various machine learning algorithms that could feasibly be used to guide programming of stimulation parameters in patients implanted with a four radial electrode DBSA. Perfect classification was achieved using only a simple feature set to consisting of the RoA center of mass and orientation. Again, a natural extension of this work to be considered in future studies is classification accuracy using three-dimensional representation of features in subject-specific models. This work will be crucial for determining the degree to which machine learning classification for programming DBSAs is generalizable and clinically applicable. Therefore, in order expand on this work, personalized models of DBS were created using various proposed methods and a validation study was conducted in a preclinical model of DBS.

5.2.Validation of computational models of DBS

Personalized models of deep brain stimulation rely on a model framework that includes volume conductor models of the brain and multi-compartment cell models to predict cellular responses to stimulation. Outcome measures from computational models of DBS include activation curves and spatial activation profiles. Although certain aspects of these models have been validated, no studies have directly compared model predicted cellular responses to experimentally acquired measures of cellular responses during stimulation. Additionally, the imprecise relationship between model results and behavioral outcomes limit the usefulness of personalized computational modeling results.

While a limited number of studies have attempted to relate model predictions of cellular activation to behavioral outcomes [100,148], no current studies have established a robust guideline for relating percent activation to the occurrence of some side-effect. The study detailed in chapter 3 compared model predictions of activation to cortical recordings of activation at the stimulation threshold for inducing a motor contraction. Results from this study suggest that although results from one of the models aligned with experimentally acquired cortical recording data, no percent activation threshold was found to be consistently predictive of motor contractions induced by stimulation. This finding may be related to the conventional technique for modeling the distribution of fibers within the corticospinal tract and suggests the new for novel techniques to determine personalized anatomically correct fiber distributions that can be directly incorporated into models of the brain.

The commonly proposed use-case for the spatial activation profile, RoA in two-dimensions and volume of tissue activated (VTA) in three-dimensions, is to superimpose the spatial activation profile onto preoperative patient imaging and select the stimulating electrode and amplitude that precisely fills the targeted brain region. Spillover into nearby brain regions that might induce side-effects is avoided, but some spillover is generally unavoidable due to the axisymmetric VTA generated by conventional DBS being superimposed onto brain targets with asymmetric geometry. To address this issue, deep brain stimulation arrays with thousands of electrodes have been proposed [71,133]. In chapter 2, we used computational modeling to show that leads with radial four electrodes around the lead provide a reasonable balance between electrode surface area, which allows for safe stimulation at conventional amplitudes with capacity to steer and shift a RoA. However, in chapter 3, our results indicated that model predictions of radial current steering may significantly over predict the capacity to steer current, although comparisons with recent studies suggest that issue related to lead design may be responsible for the lack of current steering observed *in vivo*. This contradiction illustrates the need for model validation and suggests the need for incremental advancement of deep brain stimulation arrays that can leverage conventional manufacturing and materials in their construction.

As DBS arrays enter the market, clinical programing and hardware design will rely on computational modeling more than ever. Validation of these model outcomes will be key for regulatory body acceptance and integration into clinical practice. Studies on computational models of DBS have been established that model predictions are sensitive to the electric parameters of tissue [190], which are not well established and are subject to significant uncertainty [151]. Further, it remains unclear how precisely to interpret model outcomes in the context of behavioral effects. In Chapter three, we demonstrate a first attempt at model validation by comparing model predictions of cellular activation to *in vivo* cortical recordings and behavioral outcomes. We found that one model aligned best with the cortical recording data and was, in general, consistently predictive across electrodes. However, behavioral outcomes were not consistently associated with a specific percent activation. This finding suggested, in the case of the two most proximal electrodes, that stimulation of circuits other than the $CST_{arm}/M1_{arm}$ were responsible for driving the upper limb motor contractions that were observed. Currently we can only speculate as to which circuits may be involved, but future validation work might circumvent this issue using functional imaging such as fMRI or PET to gain a more complete picture of brain regions that are modulated by stimulation. Functional imaging may also play a role in validating the relationship between therapeutic effectiveness and model predictions of spatial activation profile coverage of the targeted brain region (STN, GPi, and VIM Thalamus). It should be noted, however, that electrophysiological studies have provided evidence that the therapeutic effect of stimulation may be related to stimulation driving action potentials in a manner that disrupts information flow, termed an information lesion [7,8]. Stimulation therefore, may not simply have the effect of suppressing or enhancing overall activation in a particular brain region, making functional imaging measures difficult to interpret.

5.3.Endovascular DBS

Although several studies investigating endovascular neural stimulation have been conducted in the past several decades, this method for delivering stimulation has yet to be translated into clinical practice. Previous studies investigating the endovascular electrodes for stimulating neural tissue have relied on custom electrodes, which were used for stimulating cranial nerves [216,217]. In the past five years, a growing interest in endovascular electrodes has been motivated by the prevalence of neuroendovascular procedures, the need for less invasive cortical recording devices for use in epilepsy monitoring prior to resection surgery, and the need for less invasive neural stimulation technologies. In addition to the computational modeling study in chapter 4, experimental work by Bower et al. and Oxley et al. have demonstrated the feasibility of delivering recording and stimulating electrodes to the brain using an endovascular approach

[62,64,274]. Together this work establishes an exciting foundation for endovascular approaches to neural stimulation; however, such electrodes currently exist only as a research tool. Continued research focusing on device refinement and endovascular stimulation efficacy in preclinical models are required before these devices can be evaluated in human subjects and validated personalized computational models of endovascular DBS may help to drive these efforts forward.

References

[1] Lyons K E and Pahwa R 2004 Deep brain stimulation and essential tremor *J Clin Neurophysiol* **21** 2–5

[2] Benabid A L 2003 Deep brain stimulation for Parkinson's disease *Curr Opin Neurobiol* **13** 696–706

[3] Krauss J K, Yianni J, Loher T J and Aziz T Z 2004 Deep brain stimulation for dystonia *J Clin Neurophysiol* **21** 18–30

[4] de Koning P P, Figee M, van den Munckhof P, Schuurman P R and Denys D 2011 Current status of deep brain stimulation for obsessive-compulsive disorder: a clinical review of different targets *Curr Psychiatry Rep* **13** 274–82

[5] Schwalb J M and Hamani C 2008 The history and future of deep brain stimulation *Neurotherapeutics* **5** 3–13

[6] Sironi V A 2011 Origin and evolution of deep brain stimulation *Front Integr Neurosci* **5** 42

[7] Agnesi F, Connolly A T, Baker K B, Vitek J L and Johnson M D 2013 Deep Brain Stimulation Imposes Complex Informational Lesions *PLoS ONE* **8** e74462

[8] Grill W M, Snyder A N and Miocinovic S 2004 Deep brain stimulation creates an informational lesion of the stimulated nucleus *Neuroreport* **15** 1137–40

[9] Ruck C, Karlsson A, Steele J D, Edman G, Meyerson B A, Ericson K, Nyman H, Asberg M and Svanborg P 2008 Capsulotomy for obsessive-compulsive disorder: long-term follow-up of 25 patients *Arch Gen Psychiatry* **65** 914–21

[10] Sachdev P S and Sachdev J 2005 Long-term outcome of neurosurgery for the treatment of resistant depression *J Neuropsychiatry Clin Neurosci* **17** 478–85

[11] Valenstein E S, Cox V C and Kakolewski J W 1968 Modification of motivated behavior elicited by electrical stimulation of the hypothalamus *Science* **159** 1119–21

[12] Hamani C, McAndrews M P, Cohn M, Oh M, Zumsteg D, Shapiro C M, Wennberg R A and Lozano A M 2008 Memory enhancement induced by hypothalamic/fornix deep brain stimulation *Ann. Neurol.* **63** 119–23

[13] Awan N R, Lozano A and Hamani C 2009 Deep brain stimulation: current and future perspectives *Neurosurg Focus* **27** E2

[14] Benabid A L and Torres N 2012 New targets for DBS *Parkinsonism Relat. Disord.* **18**, **Supplement 1** S21–3

[15] Hauptman J S, DeSalles A A, Espinoza R, Sedrak M and Ishida W 2008 Potential surgical targets for deep brain stimulation in treatment-resistant depression *Neurosurg Focus* **25** E3

[16] Lyons M K 2011 Deep brain stimulation: current and future clinical applications *Mayo Clin. Proc.* **86** 662–672

[17] Tierney T S, Sankar T and Lozano A M 2011 Deep brain stimulation emerging indications *Prog. Brain Res.* **194** 83–95

[18] Franzini A, Cordella R, Messina G, Marras C E, Romito L M, Albanese A, Rizzi M, Nardocci N, Zorzi G, Zekaj E, Villani F, Leone M, Gambini O and Broggi G 2012 Targeting the brain: considerations in 332 consecutive patients treated by deep brain stimulation (DBS) for severe neurological diseases *Neurol Sci* **33** 1285–303

[19] Leone M, Franzini A, Broggi G and Bussone G 2003 Hypothalamic deep brain stimulation for intractable chronic cluster headache: a 3-year follow-up *Neurol. Sci.* **24** S143-5

[20] Mink J W, Walkup J, Frey K A, Como P, Cath D, Delong M R, Erenberg G, Jankovic J, Juncos J, Leckman J F, Swerdlow N, Visser-Vandewalle V and Vitek J L 2006 Patient selection and assessment recommendations for deep brain stimulation in Tourette syndrome *Mov Disord* **21** 1831–8

[21] Volkmann J and Benecke R 2002 Deep brain stimulation for dystonia: Patient selection and evaluation *Mov. Disord.* **17** S112–5

[22] Deuschl G and Bain P 2002 Deep brain stimulation for trauma: Patient selection and evaluation *Mov. Disord.* **17** S102–11

[23] Bronstein J M, Tagliati M, Alterman R L, Lozano A M, Volkmann J, Stefani A, Horak F B, Okun M S, Foote K D, Krack P, Pahwa R, Henderson J M, Hariz M I, Bakay R A, Rezai A, Marks W J, Moro E, Vitek J L, Weaver F M, Gross R E and DeLong M R 2011 Deep brain stimulation for Parkinson disease: an expert consensus and review of key issues *Arch. Neurol.* **68** 165

[24] Ellis T-M, Foote K D, Fernandez H H, Sudhyadhom A, Rodriguez R L, Zeilman P, Jacobson C E and Okun M S 2008 Reoperation for suboptimal outcomes after deep brain stimulation surgery *Neurosurgery* **63** 754-760-761

[25] Rezai A R, Kopell B H, Gross R E, Vitek J L, Sharan A D, Limousin P and Benabid A-L 2006 Deep brain stimulation for Parkinson's disease: Surgical issues *Mov. Disord.* **21** S197–218

[26] Halpern C H, Danish S F, Baltuch G H and Jaggi J L 2008 Brain shift during deep brain stimulation surgery for Parkinson's disease *Ster. Funct Neurosurg* **86** 37–43

[27] Khan M F, Mewes K, Gross R E and Skrinjar O 2008 Assessment of brain shift related to deep brain stimulation surgery *Ster. Funct Neurosurg* **86** 44–53

[28] Miyagi Y, Shima F and Sasaki T 2007 Brain shift: an error factor during implantation of deep brain stimulation electrodes *J Neurosurg* **107** 989–97

[29] Butson C R, Cooper S E, Henderson J M and McIntyre C C 2007 Patient-specific analysis of the volume of tissue activated during deep brain stimulation *Neuroimage* **34** 661–70

[30] Wei X F and Grill W M 2005 Current density distributions, field distributions and impedance analysis of segmented deep brain stimulation electrodes *J. Neural Eng.* **2** 139–47

[31] Chaturvedi A, Foutz T J and McIntyre C C 2012 Current steering to activate targeted neural pathways during deep brain stimulation of the subthalamic region *Brain Stimul* **5** 369–77

[32] Barbe M T, Maarouf M, Alesch F and Timmermann L 2014 Multiple source current steering--a novel deep brain stimulation concept for customized programming in a Parkinson’s disease patient *Park. Relat Disord* **20** 471–3

[33] Barbe M T, Dembek T A, Becker J, Raethjen J, Hartinger M, Meister I G, Runge M, Maarouf M, Fink G R and Timmermann L 2014 Individualized current-shaping reduces DBS-induced dysarthria in patients with essential tremor *Neurology* **82** 614–9

[34] Volkmann J, Moro E and Pahwa R 2006 Basic algorithms for the programming of deep brain stimulation in Parkinson’s disease *Mov. Disord.* **21** S284–9

[35] Kumar R 2002 Methods for programming and patient management with deep brain stimulation of the globus pallidus for the treatment of advanced Parkinson’s disease and dystonia *Mov. Disord.* **17** S198–207

[36] Nowinski W L, Chua B C, Volkau I, Puspitasari F, Marchenko Y, Runge V M and Knopp M V 2010 Simulation and assessment of cerebrovascular damage in deep brain stimulation using a stereotactic atlas of vasculature and structure derived from multiple 3-and 7-tesla scans: Technical note *J. Neurosurg.* **113** 1234–1241

[37] Palur R S, Berk C, Schulzer M and Honey C R 2002 A metaanalysis comparing the results of pallidotomy performed using microelectrode recording or macroelectrode stimulation *J Neurosurg* **96** 1058–62

[38] Terao T, Takahashi H, Yokochi F, Taniguchi M, Okiyama R and Hamada I 2003 Hemorrhagic complication of stereotactic surgery in patients with movement disorders *J Neurosurg* **98** 1241–6

[39] Gorgulho A, De Salles A A, Frighetto L and Behnke E 2005 Incidence of hemorrhage associated with electrophysiological studies performed using macroelectrodes and microelectrodes in functional neurosurgery *J Neurosurg* **102** 888–96

[40] Ben-Haim S, Asaad W F, Gale J T and Eskandar E N 2009 Risk factors for hemorrhage during microelectrode-guided deep brain stimulation and the introduction of an improved microelectrode design *Neurosurgery* **64** 754-62-3

[41] Elias W J, Sansur C A and Frysinger R C 2009 Sulcal and ventricular trajectories in stereotactic surgery *J Neurosurg* **110** 201–7

[42] Pouratian N, Reames D L, Frysinger R and Elias W J 2011 Comprehensive analysis of risk factors for seizures after deep brain stimulation surgery. Clinical article *J Neurosurg* **115** 310–5

[43] Rodriguez-Oroz M C, Obeso J A, Lang A E, Houeto J L, Pollak P, Rehncrona S, Kulisevsky J, Albanese A, Volkmann J, Hariz M I, Quinn N P, Speelman J D, Guridi J, Zamarbide I, Gironell A, Molet J, Pascual-Sedano B, Pidoux B, Bonnet A M, Agid Y, Xie J, Benabid A L, Lozano A M, Saint-Cyr J, Romito L, Contarino M F, Scerrati M, Fraix V and Van Blercom N 2005 Bilateral deep brain stimulation in Parkinson’s disease: a multicentre study with 4 years follow-up *Brain* **128** 2240–9

[44] Gologorsky Y, Ben-Haim S, Moshier E L, Godbold J, Tagliati M, Weisz D and Alterman R L 2011 Transgressing the ventricular wall during subthalamic deep brain stimulation surgery for Parkinson disease increases the risk of adverse neurological sequelae *Neurosurgery* **69** 294-9-300

[45] Bourne S K, Conrad A, Konrad P E, Neimat J S and Davis T L 2012 Ventricular width and complicated recovery following deep brain stimulation surgery *Ster. Funct Neurosurg* **90** 167–72

[46] Cardinale F, Cossu M, Castana L, Casaceli G, Schiariti M P, Miserocchi A, Fuschillo D, Moscato A, Caborni C, Arnulfo G and Lo Russo G 2013 Stereoelectroencephalography: Surgical Methodology, Safety, and Stereotactic Application Accuracy in 500 Procedures *Neurosurgery* **72** 353–66

[47] Xiaowu H, Xiufeng J, Xiaoping Z, Bin H, Laixing W, Yiqun C, Jinchuan L, Aiguo J and Jianmin L 2010 Risks of intracranial hemorrhage in patients with Parkinson’s disease receiving deep brain stimulation and ablation *Park. Relat Disord* **16** 96–100

[48] Voges J, Hilker R, Botzel K, Kiening K L, Kloss M, Kupsch A, Schnitzler A, Schneider G H, Steude U, Deuschl G and Pinsker M O 2007 Thirty days complication rate following surgery performed for deep-brain-stimulation *Mov Disord* **22** 1486–9

[49] Sansur C A, Frysinger R C, Pouratian N, Fu K M, Bittl M, Oskouian R J, Laws E R and Elias W J 2007 Incidence of symptomatic hemorrhage after stereotactic electrode placement *J Neurosurg* **107** 998–1003

[50] Fukaya C, Shimoda K, Watanabe M, Morishita T, Sumi K, Otaka T, Obuchi T, Toshikazu K, Kobayashi K, Oshima H, Yamamoto T and Katayama Y 2012 Fatal Hemorrhage From AVM After DBS Surgery: Case Report *Neuromodulation*

[51] Binder D K, Rau G and Starr P A 2003 Hemorrhagic complications of microelectrode-guided deep brain stimulation *Ster. Funct Neurosurg* **80** 28–31

[52] Binder D K, Rau G M and Starr P A 2005 Risk factors for hemorrhage during microelectrode-guided deep brain stimulator implantation for movement disorders *Neurosurgery* **56** 722-32-32

[53] Machado A G, Deogaonkar M and Cooper S 2012 Deep brain stimulation for movement disorders: patient selection and technical options *Cleve Clin J Med* **79 Suppl 2** S19-24

[54] Zrinzo L, Foltynie T, Limousin P and Hariz M I 2012 Reducing hemorrhagic complications in functional neurosurgery: a large case series and systematic literature review *J Neurosurg* **116** 84–94

[55] Lang A E, Houeto J L, Krack P, Kubu C, Lyons K E, Moro E, Ondo W, Pahwa R, Poewe W, Troster A I, Uitti R and Voon V 2006 Deep brain stimulation: preoperative issues *Mov Disord* **21 Suppl 14** S171-96

[56] Lopiano L, Rizzone M, Bergamasco B, Tavella A, Torre E, Perozzo P and Lanotte M 2002 Deep brain stimulation of the subthalamic nucleus in PD: an analysis of the exclusion causes *J. Neurol. Sci.* **195** 167–70

[57] Pizzolato G and Mandat T 2012 Deep brain stimulation for movement disorders *Front Integr Neurosci* **6** 2

[58] Rodriguez R L, Fernandez H H, Haq I and Okun M S 2007 Pearls in patient selection for deep brain stimulation *Neurologist* **13** 253–60

[59] Silberstein P, Bittar R G, Boyle R, Cook R, Coyne T, O’Sullivan D, Pell M, Peppard R, Rodrigues J, Silburn P, Stell R, Watson P and Australian D B S R G W G 2009 Deep brain stimulation for Parkinson’s disease: Australian referral guidelines *J Clin Neurosci* **16** 1001–8

[60] Louis E D and Gillman A 2011 Factors associated with receptivity to deep brain stimulation surgery among essential tremor cases *Park. Relat Disord* **17** 482–5

[61] Wachter T, Minguez-Castellanos A, Valldeoriola F, Herzog J and Stoevelaar H 2011 A tool to improve pre-selection for deep brain stimulation in patients with Parkinson’s disease *J. Neurol.* **258** 641–6

[62] Bower M R, Stead M, Van Gompel J J, Bower R S, Sulc V, Asirvatham S J and Worrell G A 2013 Intravenous recording of intracranial, broadband EEG *J Neurosci Methods* **214** 21–6

[63] Sefcik R K, Opie N L, John S E, Kellner C P, Mocco J and Oxley T J 2016 The evolution of endovascular electroencephalography: historical perspective and future applications *Neurosurg. Focus* **40** E7

[64] Oxley T J, Opie N L, John S E, Rind G S, Ronayne S M, Wheeler T L, Judy J W, McDonald A J, Dornom A, Lovell T J H, Steward C, Garrett D J, Moffat B A, Lui E H, Yassi N, Campbell B C V, Wong Y T, Fox K E, Nurse E S, Bennett I E, Bauquier S H, Liyanage K A, van der Nagel N R, Perucca P, Ahnood A, Gill K P, Yan B, Churilov L, French C R, Desmond P M, Horne M K, Kiers L, Prawer S, Davis S M, Burkitt A N, Mitchell P J, Grayden D B, May C N and O'Brien T J 2016 Minimally invasive endovascular stent-electrode array for high-fidelity, chronic recordings of cortical neural activity *Nat. Biotechnol.* **34** 320–7

[65] Birdno M J and Grill W M 2008 Mechanisms of deep brain stimulation in movement disorders as revealed by changes in stimulus frequency *Neurotherapeutics* **5** 14–25

[66] Butson C R, Cooper S E, Henderson J M and McIntyre C C 2007 Patient-specific analysis of the volume of tissue activated during deep brain stimulation *Neuroimage* **34** 661–70

[67] Frankemolle A M M, Wu J, Noecker A M, Voelcker-Rehage C, Ho J C, Vitek J L, McIntyre C C and Alberts J L 2010 Reversing cognitive-motor impairments in Parkinson's disease patients using a computational modelling approach to deep brain stimulation programming *Brain* **133** 746–61

[68] Maks C B, Butson C R, Walter B L, Vitek J L and McIntyre C C 2009 Deep brain stimulation activation volumes and their association with neurophysiological mapping and therapeutic outcomes *J. Neurol. Neurosurg. Psychiatry* **80** 659–66

[69] Miocinovic S, Noecker A M, Maks C B, Butson C R and McIntyre C C 2007 Cicerone: stereotactic neurophysiological recording and deep brain stimulation electrode placement software system *Operative Neuromodulation* Acta Neurochirurgica Supplements ed D E Sakas and B A Simpson (Springer Vienna) pp 561–7

[70] Teplitzky B A, Zitella L M, Xiao Y and Johnson M D 2016 Model-Based Comparison of Deep Brain Stimulation Array Functionality with Varying Number of Radial Electrodes and Machine Learning Feature Sets *Front. Comput. Neurosci.* 58

[71] Willsie A C and Dorval A D 2015 Computational Field Shaping for Deep Brain Stimulation With Thousands of Contacts in a Novel Electrode Geometry *Neuromodulation Technol. Neural Interface* **18** 542–51

[72] Wongsarnpigoon A and Grill W M 2010 Energy-efficient waveform shapes for neural stimulation revealed with a genetic algorithm *J. Neural Eng.* **7** 46009

[73] Plonsey R 1969 *Bioelectric phenomena* (McGraw-Hill)

[74] McIntyre C C and Grill W M 1999 Excitation of central nervous system neurons by nonuniform electric fields *Biophys J* **76** 878–88

[75] McIntyre C C and Grill W M 2000 Selective microstimulation of central nervous system neurons *Ann Biomed Eng* **28** 219–33

[76] McIntyre C C and Grill W M 2001 Finite element analysis of the current-density and electric field generated by metal microelectrodes *Ann Biomed Eng* **29** 227–35

[77] Zhang T C and Grill W M 2010 Modeling deep brain stimulation: point source approximation versus realistic representation of the electrode *J. Neural Eng.* **7** 66009

[78] Cole K S 1972 *Membranes, Ions and Impulses: A Chapter of Classical Biophysics* (University of California Press)

[79] Ranck J B 1963 Specific impedance of rabbit cerebral cortex *Exp. Neurol.* **7** 144–52

[80] Stances A . L S J 1975 Impedance and Current Density Studies *Electroanesthesia: Biomedical and Biophysical Studies* ed C A Caceres (New York, New York: Academic Press) pp 114–47

[81] Gabriel S, Lau R W and Gabriel C 1996 The dielectric properties of biological tissues: II. Measurements in the frequency range 10 Hz to 20 GHz *Phys. Med. Biol.* **41** 2251

[82] Gabriel C, Gabriel S and Corthout E 1996 The dielectric properties of biological tissues .1. Literature survey *Phys. Med. Biol.* **41** 2231–49

[83] Gabriel S, Lau R W and Gabriel C 1996 The dielectric properties of biological tissues: III. Parametric models for the dielectric spectrum of tissues *Phys. Med. Biol.* **41** 2271

[84] Nicholson P W 1965 Specific impedance of cerebral white matter *Exp. Neurol.* **13** 386–401

[85] Butson C R and McIntyre C C 2008 Current steering to control the volume of tissue activated during deep brain stimulation *Brain Stimul* **1** 7–15

[86] Miocinovic S, Lempka S F, Russo G S, Maks C B, Butson C R, Sakaie K E, Vitek J L and McIntyre C C 2009 Experimental and theoretical characterization of the voltage distribution generated by deep brain stimulation *Exp Neurol* **216** 166–76

[87] Zitella L M, Mohsenian K, Pahwa M, Gloeckner C and Johnson M D 2013 Computational modeling of pedunculopontine nucleus deep brain stimulation *J Neural Eng* **10** 45005

[88] Tuch D S, Wedeen V J, Dale A M, George J S and Belliveau J W 2001 Conductivity tensor mapping of the human brain using diffusion tensor MRI *Proc. Natl. Acad. Sci.* **98**

[89] Wolters C H, Anwander A, Tricoche X, Weinstein D, Koch M A and MacLeod R S 2006 Influence of tissue conductivity anisotropy on EEG/MEG field and return current computation in a realistic head model: a simulation and visualization study using high-resolution finite element modeling *NeuroImage* **30** 813–26

[90] Güllmar D, Haueisen J and Reichenbach J R 2010 Influence of anisotropic electrical conductivity in white matter tissue on the EEG/MEG forward and inverse solution. A high-resolution whole head simulation study *NeuroImage* **51** 145–63

[91] Butson C R and McIntyre C C 2005 Tissue and electrode capacitance reduce neural activation volumes during deep brain stimulation *Clin Neurophysiol* **116** 2490–500

[92] Hines M L and Carnevale N T 1997 The NEURON simulation environment *Neural Comput* **9** 1179–209

[93] Rattay F 1989 Analysis of models for extracellular fiber stimulation *IEEE Trans. Biomed. Eng.* **36** 676–82

[94] Rattay F 1986 Analysis of Models for External Stimulation of Axons *IEEE Trans. Biomed. Eng.* **BME-33** 974–7

[95] McNeal D R 1976 Analysis of a Model for Excitation of Myelinated Nerve *IEEE Trans. Biomed. Eng.* **BME-23** 329–37

[96] McIntyre C C, Richardson A G and Grill W M 2002 Modeling the excitability of mammalian nerve fibers: Influence of afterpotentials on the recovery cycle *J Neurophysiol* **87** 995–1006

[97] Kuncel A M and Grill W M 2004 Selection of stimulus parameters for deep brain stimulation *Clin Neurophysiol* **115** 2431–41

[98] Johnson M D and McIntyre C C 2008 Quantifying the Neural Elements Activated and Inhibited by Globus Pallidus Deep Brain Stimulation *J Neurophysiol* **100** 2549–63

[99] Johnson M D, Zhang J, Ghosh D, McIntyre C C and Vitek J L 2012 Neural targets for relieving parkinsonian rigidity and bradykinesia with pallidal deep brain stimulation *J Neurophysiol* **108** 567–77

[100] Keane M, Deyo S, Abosch A, Bajwa J A and Johnson M D 2012 Improved spatial targeting with directionally segmented deep brain stimulation leads for treating essential tremor *J. Neural Eng.* **9** 46005

[101] Martens H C, Toader E, Decre M M, Anderson D J, Vetter R, Kipke D R, Baker K B, Johnson M D and Vitek J L 2011 Spatial steering of deep brain stimulation volumes using a novel lead design *Clin Neurophysiol* **122** 558–66

[102] Teplitzky B A, Connolly A T, Bajwa J A and Johnson M D 2014 Computational modeling of an endovascular approach to deep brain stimulation *J. Neural Eng.* **11**

[103] Holsheimer J, Nuttin B, King G W, Wesselink W A, Gybels J M and de Sutter P 1998 Clinical evaluation of paresthesia steering with a new system for spinal cord stimulation *Neurosurgery* **42** 541–7

[104] Manola L, Holsheimer J, Veltink P H, Bradley K and Peterson D 2007 Theoretical investigation into longitudinal cathodal field steering in spinal cord stimulation *Neuromodulation* **10** 120–32

[105] Firszt J B, Koch D B, Downing M and Litvak L 2007 Current steering creates additional pitch percepts in adult cochlear implant recipients *Otol Neurotol* **28** 629–36

[106] Berenstein C K, Mens L H, Mulder J J and Vanpoucke F J 2008 Current steering and current focusing in cochlear implants: comparison of monopolar, tripolar, and virtual channel electrode configurations *Ear Hear* **29** 250–60

[107] Matteucci P B, Chen S C, Tsai D, Dodds C W, Dokos S, Morley J W, Lovell N H and Suaning G J 2013 Current steering in retinal stimulation via a quasimonopolar stimulation paradigm *Invest Ophthalmol Vis Sci* **54** 4307–20

[108] Dumm G, Fallon J B, Williams C E and Shivdasani M N 2014 Virtual Electrodes by Current Steering in Retinal Prostheses *Invest Ophthalmol Vis Sci*

[109] Buhlmann J, Hofmann L, Tass P A and Hauptmann C 2011 Modeling of a Segmented Electrode for Desynchronizing Deep Brain Stimulation *Front. Neuroengineering* **4**

[110] Contarino M F, Bour L J, Verhagen R, Lourens M A, de Bie R M, van den Munckhof P and Schuurman P R 2014 Directional steering: A novel approach to deep brain stimulation *Neurology* **83** 1163–9

[111] Cubo R, Astrom M and Medvedev A 2014 Target coverage and selectivity in field steering brain stimulation *Conf Proc IEEE Eng Med Biol Soc* **2014** 522–5

[112] Pollo C, Kaelin-Lang A, Oertel M F, Stieglitz L, Taub E, Fuhr P, Lozano A M, Raabe A and Schupbach M 2014 Directional deep brain stimulation: an intraoperative double-blind pilot study *Brain* **137** 2015–26

[113] Bour L J, Lourens M A J, Verhagen R, de Bie R M A, van den Munckhof P, Schuurman P R and Contarino M F 2015 Directional Recording of Subthalamic Spectral Power Densities in Parkinson's Disease and the Effect of Steering Deep Brain Stimulation *Brain Stimulat.*

[114] Xiao Y, Pena E and Johnson M D 2016 Theoretical Optimization of Stimulation Strategies for a Directionally Segmented Deep Brain Stimulation Electrode Array *IEEE Trans. Biomed. Eng.* **63** 359–71

[115] Chaturvedi A, Luján J L and McIntyre C C 2013 Artificial neural network based characterization of the volume of tissue activated during deep brain stimulation *J. Neural Eng.* **10** 56023

[116] Grill W M and Mortimer J T 1994 Electrical properties of implant encapsulation tissue *Ann. Biomed. Eng.* **22** 23–33

[117] Lempka S F, Miocinovic S, Johnson M D, Vitek J L and McIntyre C C 2009 In vivo impedance spectroscopy of deep brain stimulation electrodes *J. Neural Eng.* **6** 46001

[118] Howell B, Naik S and Grill W M 2014 Influences of interpolation error, electrode geometry, and the electrode-tissue interface on models of electric fields produced by deep brain stimulation *IEEE Trans. Biomed. Eng.* **61** 297–307

[119] Wei X F and Grill W M 2009 Impedance characteristics of deep brain stimulation electrodes *in vitro* and *in vivo J. Neural Eng.* **6** 46008

[120] Tommasi G, Krack P, Fraix V, Bas J-F L, Chabardes S, Benabid A-L and Pollak P 2008 Pyramidal tract side effects induced by deep brain stimulation of the subthalamic nucleus *J. Neurol. Neurosurg. Psychiatry* **79** 813–9

[121] Kamiya K, Hori M, Miyajima M, Nakajima M, Suzuki Y, Kamagata K, Suzuki M, Arai H, Ohtomo K and Aoki S 2014 Axon Diameter and Intra-Axonal Volume Fraction of the Corticospinal Tract in Idiopathic Normal Pressure Hydrocephalus Measured by Q-Space Imaging *PLoS ONE* **9** e103842

[122] McIntyre C C, Grill W M, Sherman D L and Thakor N V 2004 Cellular Effects of Deep Brain Stimulation: Model-Based Analysis of Activation and Inhibition *J. Neurophysiol.* **91** 1457–69

[123] Lempka S F, Johnson M D, Miocinovic S, Vitek J L and McIntyre C C 2010 Current-controlled deep brain stimulation reduces in vivo voltage fluctuations observed during voltage-controlled stimulation *Clin Neurophysiol* **121** 2128–33

[124] Hines M L and Carnevale N T 1997 The NEURON simulation environment *Neural Comput.* **9** 1179–209

[125] Merrill D R, Bikson M and Jefferys J G 2005 Electrical stimulation of excitable tissue: design of efficacious and safe protocols *J Neurosci Methods* **141** 171–98

[126] Cogan S F 2008 Neural Stimulation and Recording Electrodes *Annu. Rev. Biomed. Eng.* **10** 275–309

[127] McCreery D B, Agnew W F, Yuen T G H and Bullara L 1990 Charge density and charge per phase as cofactors in neural injury induced by electrical stimulation *IEEE Trans. Biomed. Eng.* **37** 996–1001

[128] Giselsson T M, Midtiby H S and Jorgensen R N 2013 Seedling Discrimination with Shape Features Derived from a Distance Transform *Sensors* **13** 5585–602

[129] Hu M 1962 Visual-Pattern Recognition by Moment Invariants *Ire Trans. Inf. Theory* **8** 179–87

[130] Lowe D G 1999 Object recognition from local scale-invariant features *The Proceedings of the Seventh IEEE International Conference on Computer Vision, 1999* The Proceedings of the Seventh IEEE International Conference on Computer Vision, 1999 vol 2pp 1150–7 vol.2

[131] Lauer F and Guermeur Y 2011 MSVMpack: A Multi-Class Support Vector Machine Package *J. Mach. Learn. Res.* **12** 2293–6

[132] Breiman L 2001 Random Forests *Mach. Learn.* **45** 5–32

[133] Willsie A and Dorval A 2015 Fabrication and initial testing of the μDBS: a novel Deep Brain Stimulation electrode with thousands of individually controllable contacts *Biomed. Microdevices* **17** 1–12

[134] Connolly A T, Vetter R J, Hetke J F, Teplitzky B A, Kipke D R, Pellinen D S, Anderson D J, Baker K B, Vitek J L and Johnson M D 2016 A Novel Lead Design for Modulation and Sensing of Deep Brain Structures *IEEE Trans. Biomed. Eng.* **63** 148–57

[135] Cogan S F, Plante T D and Ehrlich J 2004 Sputtered iridium oxide films (SIROFs) for low-impedance neural stimulation and recording electrodes *26th Annual International Conference of the IEEE Engineering in Medicine and Biology Society, 2004. IEMBS '04* 26th Annual International Conference of the IEEE Engineering in Medicine and Biology Society, 2004. IEMBS '04 vol 2pp 4153–6

[136] Luo X, Weaver C L, Zhou D D, Greenberg R and Cui X T 2011 Highly stable carbon nanotube doped poly (3, 4-ethylenedioxythiophene) for chronic neural stimulation *Biomaterials* **32** 5551–5557

[137] Grill W M and Wei X F 2009 High Efficiency Electrodes for Deep Brain Stimulation *Conf. Proc. Annu. Int. Conf. IEEE Eng. Med. Biol. Soc. IEEE Eng. Med. Biol. Soc. Conf.* **2009** 3298–301

[138] Hegarty D 2011 Spinal Cord Stimulation: The Clinical Application of New Technology *Anesthesiol. Res. Pract.* **2012** e375691

[139] Wilson B S and Dorman M F 2008 Cochlear implants: Current designs and future possibilities *J. Rehabil. Res. Dev.* **45** 695–730

[140] Dallas P 1992 The active cochlea *J. Neurosci.* **2** 4575–4585

[141] Bonham B H and Litvak L M 2008 Current focusing and steering: Modeling, physiology, and psychophysics *Hear. Res.* **242** 141–53

[142] Montgomery E B 2010 *Deep Brain Stimulation Programming: Principles and Practice* (Oxford University Press)

[143] Herrero M-T, Barcia C and Navarro J 2002 Functional anatomy of thalamus and basal ganglia *Child's Nerv. Syst.* **18** 386–404

[144] Riva-Posse P, Choi K S, Holtzheimer P E, McIntyre C C, Gross R E, Chaturvedi A, Crowell A L, Garlow S J, Rajendra J K and Mayberg H S 2014 Defining Critical White Matter Pathways Mediating Successful Subcallosal Cingulate Deep Brain Stimulation for Treatment-Resistant Depression *Biol. Psychiatry* **76** 963–9

[145] Greenberg B D, Malone D A, Friehs G M, Rezai A R, Kubu C S, Malloy P F, Salloway S P, Okun M S, Goodman W K and Rasmussen S A 2006 Three-Year Outcomes in Deep Brain Stimulation for Highly Resistant Obsessive-Compulsive Disorder *Neuropsychopharmacology* **31** 2384–93

[146] Little S and Brown P 2012 What brain signals are suitable for feedback control of deep brain stimulation in Parkinson's disease? *Ann. N. Y. Acad. Sci.* **1265** 9–24

[147] Chaturvedi A, Butson C R, Lempka S F, Cooper S E and McIntyre C C 2010 Patient-specific models of deep brain stimulation: Influence of field model complexity on neural activation predictions *Brain Stimulat.* **3** 65–77

[148] Zitella L M, Teplitzky B A, Yager P, Hudson H M, Brintz K, Duchin Y, Harel N, Vitek J L, Baker K B and Johnson M D 2015 Subject-specific computational modeling of DBS in the PPTg area *Front. Comput. Neurosci.* **9** 93

[149] Schmidt C and van Rienen U 2012 Modeling the Field Distribution in Deep Brain Stimulation: The Influence of Anisotropy of Brain Tissue *IEEE Trans. Biomed. Eng.* **59** 1583–92

[150] Faes T J C, Meij H A van der, Munck J C de and Heethaar R M 1999 The electric resistivity of human tissues (100 Hz-10 MHz): a meta-analysis of review studies *Physiol. Meas.* **20** R1

[151] Schmidt C, Grant P, Lowery M and van Rienen U 2013 Influence of Uncertainties in the Material Properties of Brain Tissue on the Probabilistic Volume of Tissue Activated *IEEE Trans. Biomed. Eng.* **60** 1378–87

[152] Johnson M D, Otto K J and Kipke D R 2005 Repeated voltage biasing improves unit recordings by reducing resistive tissue impedances *IEEE Trans. Neural Syst. Rehabil. Eng. Publ. IEEE Eng. Med. Biol. Soc.* **13** 160–5

[153] Otto K J, Johnson M D and Kipke D R 2006 Voltage pulses change neural interface properties and improve unit recordings with chronically implanted microelectrodes *IEEE Trans. Biomed. Eng.* **53** 333–40

[154] Williams J C, Hippensteel J A, Dilgen J, Shain W and Kipke D R 2007 Complex impedance spectroscopy for monitoring tissue responses to inserted neural implants *J. Neural Eng.* **4** 410

[155] Yousif N and Liu X 2009 Investigating the depth electrode–brain interface in deep brain stimulation using finite element models with graded complexity in structure and solution *J. Neurosci. Methods* **184** 142–51

[156] Blomstedt P, Sandvik U and Tisch S 2010 Deep brain stimulation in the posterior subthalamic area in the treatment of essential tremor *Mov. Disord.* **25** 1350–6

[157] Hashimoto T, Elder C M, Okun M S, Patrick S K and Vitek J L 2003 Stimulation of the Subthalamic Nucleus Changes the Firing Pattern of Pallidal Neurons *J. Neurosci.* **23** 1916–23

[158] Debanne D 2004 Information processing in the axon *Nat. Rev. Neurosci.* **5** 304–16

[159] Chomiak T and Hu B 2007 Axonal and somatic filtering of antidromically evoked cortical excitation by simulated deep brain stimulation in rat brain *J. Physiol.* **579** 403–12

[160] Rosenbaum R, Zimnik A, Zheng F, Turner R S, Alzheimer C, Doiron B and Rubin J E 2014 Axonal and synaptic failure suppress the transfer of firing rate oscillations, synchrony and information during high frequency deep brain stimulation *Neurobiol. Dis.* **62** 86–99

[161] Ludwig K A, Langhals N B, Joseph M D, Richardson-Burns S M, Hendricks J L and Kipke D R 2011 Poly(3,4-ethylenedioxythiophene) (PEDOT) polymer coatings facilitate smaller neural recording electrodes *J. Neural Eng.* **8** 14001

[162] Weiland J D, Anderson D J and Humayun M S 2002 In vitro electrical properties for iridium oxide versus titanium nitride stimulating electrodes *IEEE Trans. Biomed. Eng.* **49** 1574–9

[163] Johnson M D and McIntyre C C 2008 Quantifying the Neural Elements Activated and Inhibited by Globus Pallidus Deep Brain Stimulation *J Neurophysiol* **100** 2549–63

[164] Miocinovic S, Parent M, Butson C R, Hahn P J, Russo G S, Vitek J L and McIntyre C C 2006 Computational analysis of subthalamic nucleus and lenticular fasciculus activation during therapeutic deep brain stimulation *J Neurophysiol* **96** 1569–80

[165] Hartmann C J, Chaturvedi A and Lujan J L 2015 Quantitative analysis of axonal fiber activation evoked by deep brain stimulation via activation density heat maps *Neuroprosthetics* **9** 28

[166] Abosch A, Yacoub E, Ugurbil K and Harel N 2010 An Assessment of Current Brain Targets for Deep Brain Stimulation Surgery With Susceptibility-Weighted Imaging at 7 Tesla *Neurosurgery* **67** 1745–56

[167] Lenglet C, Abosch A, Yacoub E, De Martino F, Sapiro G and Harel N 2012 Comprehensive in vivo mapping of the human basal ganglia and thalamic connectome in individuals using 7T MRI *PLoS One* **7** e29153

[168] Xiao Y, Zitella L M, Duchin Y, Teplitzky B A, Kastl D, Adriany G, Yacoub E, Harel N and Johnson M D 2016 Multimodal 7T Imaging of Thalamic Nuclei for Preclinical Deep Brain Stimulation Applications *Brain Imaging Methods* 264

[169] Zitella L M, Xiao Y, Teplitzky B A, Kastl D J, Duchin Y, Baker K B, Vitek J L, Adriany G, Yacoub E, Harel N and Johnson M D 2015 In Vivo 7T MRI of the Non-Human Primate Brainstem *PLOS ONE* **10** e0127049

[170] Moffitt M A, Mcintyre C C and Grill W M 2004 Prediction of myelinated nerve fiber stimulation thresholds: limitations of linear models *IEEE Trans. Biomed. Eng.* **51** 229–36

[171] Warman E N, Grill W M and Durand D 1992 Modeling the effects of electric fields on nerve fibers: Determination of excitation thresholds *IEEE Trans. Biomed. Eng.* **39** 1244–54

[172] McIntyre C C, Savasta M, Kerkerian-Le Goff L and Vitek J L 2004 Uncovering the mechanism(s) of action of deep brain stimulation: activation, inhibition, or both *Clin Neurophysiol* **115** 1239–48

[173] Johnson D, Zhang S, Miocinovic S and Johnson M 2016 Developing a Python-based Open-Source Stereotactic Surgical Planning Software Package

[174] Elder C M, Hashimoto T, Zhang J and Vitek J L 2005 Chronic implantation of deep brain stimulation leads in animal models of neurological disorders *J. Neurosci. Methods* **142** 11–6

[175] Hutchison W D, Allan R J, Opitz H, Levy R, Dostrovsky J O, Lang A E and Lozano A M 1998 Neurophysiological identification of the subthalamic nucleus in surgery for Parkinson's disease *Ann Neurol* **44** 622–8

[176] Filion M, Tremblay L and Bedard P J 1988 Abnormal influences of passive limb movement on the activity of globus pallidus neurons in parkinsonian monkeys *Brain Res* **444** 165–76

[177] Maynard E M, Nordhausen C T and Normann R A 1997 The Utah Intracortical Electrode Array: A recording structure for potential brain-computer interfaces *Electroencephalogr. Clin. Neurophysiol.* **102** 228–39

[178] Rousche P J and Normann R A 1992 A method for pneumatically inserting an array of penetrating electrodes into cortical tissue *Ann. Biomed. Eng.* **20** 413–22

[179] Jenkinson C F, Beckmann T E, Behrens M W, Woolrich M W and Smith S M 2012 FSL *NeuroImage* **62** 782–90

[180] Jenkinson M and Smith S M 2001 A Global Optimisation Method for Robust Affine Registration of Brain Images *Med. Image Anal.* **5** 143–56

[181] Behrens T E J, Woolrich M W, Jenkinson M, Johansen-Berg H, Nunes R G, Clare S, Matthews P M, Brady J M and Smith S M 2003 Characterization and propagation of uncertainty in diffusion-weighted MR imaging *Magn. Reson. Med.* **50** 1077–88

[182] Basser P J, Mattiello J and LeBihan D 1994 MR diffusion tensor spectroscopy and imaging. *Biophys. J.* **66** 259–67

[183] Baumann S B, Wozny D R, Kelly S K and Meno F M 1997 The electrical conductivity of human cerebrospinal fluid at body temperature *IEEE Trans Biomed Eng* **44** 220–3

[184] Paxinos G 2009 *The Rhesus Monkey Brain: In Stereotaxic Coordinates* (Elsevier/Academic Press)

[185] Schmahmann J D and Pandya D N 2006 *Fiber pathways of the brain* (Oxford ; New York: Oxford University Press)

[186] Jenkinson M, Bannister P, Brady J M and Smith S M 2002 Improved Optimisation for the Robust adn Accurate Linear Registration and Motion Correction of Brain Images *Neuroimage* **17** 825–41

[187] Behrens T E J, Berg H J, Jbabdi S, Rushworth M F S and Woolrich M W 2007 Probabilistic diffusion tractography with multiple fibre orientations: What can we gain? *NeuroImage* **34** 144–55

[188] Król P, Król B, Holler P and Telitsyna N 2006 Polyurethane anionomers synthesised with aromatic, aliphatic or cycloaliphatic diisocyanates, polyoxyethylene glycol and 2,2-bis(hydroxymethyl)propionic acid *Colloid Polym. Sci.* **284** 1107–20

[189] Yousif N, Bayford R and Liu X 2008 The influence of reactivity of the electrode–brain interface on the crossing electric current in therapeutic deep brain stimulation *Neuroscience* **156** 597–606

[190] Butson C R and McIntyre C C 2005 Tissue and electrode capacitance reduce neural activation volumes during deep brain stimulation *Clin. Neurophysiol. Off. J. Int. Fed. Clin. Neurophysiol.* **116**

[191] Grant P F and Lowery M M 2010 Effect of dispersive conductivity and permittivity in volume conductor models of deep brain stimulation *IEEE Trans. Biomed. Eng.* **57** 2386–93

[192] Hines M L and Carnevale N T 1997 The NEURON simulation environment *Neural Comput.* **9** 1179–209

[193] Teplitzky B A, Connolly A T, Bajwa J A and Johnson M D 2014 Computational modeling of an endovascular approach to deep brain stimulation *J. Neural Eng.* **11**

[194] Howell B and McIntyre C C 2016 Analyzing the tradeoff between electrical complexity and accuracy in patient-specific computational models of deep brain stimulation *J. Neural Eng.* **13** 36023

[195] Akkal D, Dum R P and Strick P L 2007 Supplementary Motor Area and Presupplementary Motor Area: Targets of Basal Ganglia and Cerebellar Output *J. Neurosci.* **27** 10659–73

[196] Middleton F A and Strick P L 1997 Dentate output channels: motor and cognitive components *Prog Brain Res* **114** 553–66

[197] Bostan A C, Dum R P and Strick P L 2013 Cerebellar networks with the cerebral cortex and basal ganglia *Trends Cogn. Sci.* **17** 241–54

[198] Thani N B, Bala A, Swann G B and Lind C R P 2011 Accuracy of postoperative computed tomography and magnetic resonance image fusion for assessing deep brain stimulation electrodes *Neurosurgery* **69**207–214; discussion 214

[199] O’Gorman R L, Jarosz J M, Samuel M, Clough C, Selway R P and Ashkan K 2009 CT/MR Image Fusion in the Postoperative Assessment of Electrodes Implanted for Deep Brain Stimulation *Stereotact. Funct. Neurosurg.* **87** 205–10

[200] Pinsker M O, Herzog J, Falk D, Volkmann J, Deuschl G and Mehdorn M 2008 Accuracy and Distortion of Deep Brain Stimulation Electrodes on Postoperative MRI and CT *Cent. Eur. Neurosurg. - Zentralblatt Für Neurochir.* **69** 144–7

[201] Geevarghese R, O'Gorman Tuura R, Lumsden D E, Samuel M and Ashkan K 2016 Registration Accuracy of CT/MRI Fusion for Localisation of Deep Brain Stimulation Electrode Position: An Imaging Study and Systematic Review *Stereotact. Funct. Neurosurg.* **94** 159–63

[202] Bossetti C A, Birdno M J and Grill W M 2008 Analysis of the quasi-static approximation for calculating potentials generated by neural stimulation *J. Neural Eng.* **5** 44

[203] Schmidt C and Rienen U van 2012 Quantification of uncertainties in brain tissue conductivity in a heterogeneous model of deep brain stimulation using a non-intrusive projection approach *2012 Annual International Conference of the IEEE Engineering in Medicine and Biology Society* 2012 Annual International Conference of the IEEE Engineering in Medicine and Biology Society pp 4136–9

[204] Driller J, Hilal S K, Michelsen W J, Sollish B, Katz B and Konig W Jr 1969 Development and use of the POD catheter in the cerebral vascular system *Med Res Eng* **8** 11–6

[205] Penn R D, Hilal S K, Michelsen W J, Goldensohn E S and Driller J 1973 Intravascular intracranial EEG recording. Technical note *J Neurosurg* **38** 239–43

[206] Llinas R R, Walton K D, Nakao M, Hunter I and Anquetil P A 2005 Neuro-vascular central nervous recording/stimulating system: Using nanotechnology probes *J. Nanoparticle Res.* **7** 111–27

[207] Watanabe H, Takahashi H, Nakao M, Walton K and Llinas R R 2009 Intravascular Neural Interface with Nanowire Electrode *Electron. Commun. Jpn.* **92** 29–37

[208] Zeitlhofer J, Feldner G, Heimberger K, Mayr N and Samec P 1990 [Transarterial EEG in superselective cerebral angiography] *EEG EMG Z Elektroenzephalogr Elektromyogr Verwandte Geb* **21** 70–2

[209] Nakase H, Ohnishi H, Touho H, Furuoka N, Yamada K, Takaoka M, Senoh M, Komatsu T, Karasawa J, Yamamoto S and et al. 1993 [Spike discharge detected by intra-arterial electroencephalography from intra-arterial guide wire in temporal lobe epilepsy] *No Shinkei* **45** 973–7

[210] Stoeter P, Dieterle L, Meyer A and Prey N 1995 Intracranial electroencephalographic and evoked-potential recording from intravascular guide wires *AJNR Am J Neuroradiol* **16** 1214–7

[211] Ishida S, Shimamoto H, Abe T, Motooka H, Sakurai S, Takayama K, Yamaguchi H and Maeda H 1998 Intracranial EEG Recording from Intravascular Electrodes in Patients with Temporal Lobe Epilepsy *Epilepsia* **39** 77–77

[212] Garcia-Asensio S, Guelbenzu S, Barrena R and Valero P 1999 Technical aspects of intra-arterial electroencephalogram recording *Interv. Neuroradiol.* **5** 289–99

[213] Boniface S J and Antoun N 1997 Endovascular electroencephalography: the technique and its application during carotid amytal assessment *J Neurol Neurosurg Psychiatry* **62** 193–5

[214] Mikuni N, Ikeda A, Murao K, Terada K, Nakahara I, Taki W, Kikuchi H and Shibasaki H 1997 "Cavernous Sinus EEG": A New Method for the Preoperative Evaluation of Temporal Lobe Epilepsy *Epilepsia* **38** 472–482

[215] Kunieda T, Ikeda A, Mikuni N, Ohara S, Sadato A, Taki W, Hashimoto N and Shibasaki H 2000 Use of cavernous sinus EEG in the detection of seizure onset and spread in mesial temporal lobe epilepsy *Epilepsia* **41** 1411–9

[216] Schauerte P, Mischke K, Plisiene J, Waldmann M, Zarse M, Stellbrink C, Schimpf T, Knackstedt C, Sinha A and Hanrath P 2001 Catheter stimulation of cardiac parasympathetic nerves in humans: a novel approach to the cardiac autonomic nervous system *Circulation* **104** 2430–5

[217] Ponikowski P, Javaheri S, Michalkiewicz D, Bart B A, Czarnecka D, Jastrzebski M, Kusiak A, Augostini R, Jagielski D, Witkowski T, Khayat R N, Oldenburg O, Gutleben K J, Bitter T, Karim R, Iber C, Hasan A, Hibler K, Germany R and Abraham W T 2012 Transvenous phrenic nerve stimulation for the treatment of central sleep apnoea in heart failure *Eur. Heart J.* **33** 889–94

[218] Laxton A W, Tang-Wai D F, McAndrews M P, Zumsteg D, Wennberg R, Keren R, Wherrett J, Naglie G, Hamani C, Smith G S and Lozano A M 2010 A phase I trial of deep brain stimulation of memory circuits in Alzheimer's disease *Ann. Neurol.* **68** 521–34

[219] Mayberg H S, Lozano A M, Voon V, McNeely H E, Seminowicz D, Hamani C, Schwalb J M and Kennedy S H 2005 Deep brain stimulation for treatment-resistant depression *Neuron* **45** 651–60

[220] Kennedy S H, Giacobbe P, Rizvi S J, Placenza F M, Nishikawa Y, Mayberg H S and Lozano A M 2011 Deep brain stimulation for treatment-resistant depression: follow-up after 3 to 6 years *Am J Psychiatry* **168** 502–10

[221] Mai J K . P G .Voss, T 2007 *Atlas of the Human Brain* (Düsseldorf, Germany: Elsevier Inc.)

[222] Nowinski W L . T A; Volkau I .Marchenko Y; Runge V M . 2009 *The Cerefy Atlas of Cerebral Vasculature* (New York: Thieme Medical Publishers)

[223] Hales T C 2007 The Jordan curve theorem, formally and informally *Am. Math. Mon.* **114** 882–94

[224] Saunders R C and Aggleton J P 2007 Origin and topography of fibers contributing to the fornix in macaque monkeys *Hippocampus* **17** 396–411

[225] McNeely H E, Mayberg H S, Lozano A M and Kennedy S H 2008 Neuropsychological impact of Cg25 deep brain stimulation for treatment-resistant depression: preliminary results over 12 months *J Nerv Ment Dis* **196** 405–10

[226] Nabutovsky Y, Florio J, Morgan K, Grill W M and Farazi T G 2007 Lead design and initial applications of a new lead for long-term endovascular vagal stimulation *Pacing Clin Electrophysiol* **30 Suppl 1** S215-8

[227] Butson C R and McIntyre C C 2006 Role of electrode design on the volume of tissue activated during deep brain stimulation *J Neural Eng* **3** 1–8

[228] Duffis E J, Tank V, Gandhi C D and Prestigiacomo C J 2013 Recent advances in neuroendovascular therapy *Clin Neurol Neurosurg* **115** 853–8

[229] Boulos A S, Levy E I, Bendok B R, Kim S H, Qureshi A I, Guterman L R and Hopkins L N 2004 Evolution of neuroendovascular intervention: a review of advancement in device technology *Neurosurgery* **54** 438-52-3

[230] Gonzalez N, Sedrak M, Martin N and Vinuela F 2008 Impact of anatomic features in the endovascular embolization of 181 anterior communicating artery aneurysms *Stroke* **39** 2776–82

[231] Crowell R M and Morawetz R B 1977 The anterior communicating artery has significant branches *Stroke* **8** 272–3

[232] Moret J, Pierot L, Boulin A, Castaings L and Rey A 1996 Endovascular treatment of anterior communicating artery aneurysms using Guglielmi detachable coils *Neuroradiology* **38** 800–5

[233] Saatci I, Geyik S, Yavuz K and Cekirge S 2011 X-configured stent-assisted coiling in the endovascular treatment of complex anterior communicating artery aneurysms: a novel reconstructive technique *AJNR Am J Neuroradiol* **32** E113-7

[234] Cohen J E, Gomori J M, Moscovici S and Itshayek E 2012 Balloon-guided navigation technique to perform stenting in an acutely angled anterior cerebral artery *J Clin Neurosci* **19** 452–4

[235] Gerszten P C, Welch W C, Spearman M P, Jungreis C A and Redner R L 1997 Isolated deep cerebral venous thrombosis treated by direct endovascular thrombolysis *Surg Neurol* **48** 261–6

[236] Holder C A, Bell D A, Lundell A L, Ulmer J L and Glazier S S 1997 Isolated straight sinus and deep cerebral venous thrombosis: successful treatment with local infusion of urokinase. Case report *J Neurosurg* **86** 704–7

[237] Spearman M P, Jungreis C A, Wehner J J, Gerszten P C and Welch W C 1997 Endovascular thrombolysis in deep cerebral venous thrombosis *AJNR Am J Neuroradiol* **18** 502–6

[238] Philips M F, Bagley L J, Sinson G P, Raps E C, Galetta S L, Zager E L and Hurst R W 1999 Endovascular thrombolysis for symptomatic cerebral venous thrombosis *J Neurosurg* **90** 65–71

[239] Yamini B, Loch Macdonald R and Rosenblum J 2001 Treatment of deep cerebral venous thrombosis by local infusion of tissue plasminogen activator *Surg Neurol* **55** 340–6

[240] L'Italien G J, Kidson I G, Megerman J and Abbott W M 1979 In vivo measurement of blood vessel wall thickness *Am J Physiol* **237** H265-8

[241] Chaynes P 2003 Microsurgical anatomy of the great cerebral vein of Galen and its tributaries *J Neurosurg* **99** 1028–38

[242] Murphy D A, Johnstone D E and Armour J A 1985 Preliminary observations on the effects of stimulation of cardiac nerves in man *Can. J. Physiol. Pharmacol.* **63** 649–55

[243] Carlson M D, Geha A S, Hsu J, Martin P J, Levy M N, Jacobs G and Waldo A L 1992 Selective stimulation of parasympathetic nerve fibers to the human sinoatrial node *Circulation* **85** 1311–7

[244] Murphy D A and Armour J A 1992 Human cardiac nerve stimulation *Ann. Thorac. Surg.* **54** 502–6

[245] Asconapé J J, Moore D D, Zipes D P, Hartman L M and Duffell W H 1999 Bradycardia and asystole with the use of vagus nerve stimulation for the treatment of epilepsy: a rare complication of intraoperative device testing *Epilepsia* **40** 1452–4

[246] Tatum W O, Moore D B, Stecker M M, Baltuch G H, French J A, Ferreira J A, Carney P M, Labar D R and Vale F L 1999 Ventricular asystole during vagus nerve stimulation for epilepsy in humans *Neurology* **52** 1267–1267

[247] Goldberger J J, Kadish A H, Johnson D and Qi X 1999 New technique for vagal nerve stimulation *J. Neurosci. Methods* **91** 109–14

[248] Thompson BSc G W, Levett MD J M, Miller MD S M, Hill PhD M R S, Meffert MD W G, Kolata DVM R J, Clem DVM M F, Murphy DVM M , David A and Armour MD P JAndrew 1998 Bradycardia Induced by Intravascular Versus Direct Stimulation of the Vagus Nerve *Ann. Thorac. Surg.* **65** 637–42

[249] Schauerte P, Scherlag B J, Scherlag M A, Goli S, Jackman W M and Lazzara R 1999 Ventricular rate control during atrial fibrillation by cardiac parasympathetic nerve stimulation: a transvenous approach *J. Am. Coll. Cardiol.* **34** 2043–50

[250] Schauerte P N, Scherlag B J, Scherlag M A, Goli S, Jackman W and Lazzara R 1999 Transvenous parasympathetic cardiac nerve stimulation: an approach for stable sinus rate control *J Cardiovasc Electrophysiol* **10** 1517–24

[251] Schauerte P, Scherlag B J, Scherlag M A, Jackman W M and Lazzara R 2000 Transvenous parasympathetic nerve stimulation in the inferior vena cava and atrioventricular conduction *J Cardiovasc Electrophysiol* **11** 64–9

[252] Scherlag B J, Yamanashi W S, Schauerte P, Scherlag M, Sun Y X, Hou Y, Jackman W M and Lazzara R 2002 Endovascular stimulation within the left pulmonary artery to induce slowing of heart rate and paroxysmal atrial fibrillation *Cardiovasc. Res.* **54** 470–5

[253] Hasdemir C, Scherlag B J, Yamanashi W S, Lazzara R and Jackman W M 2003 Endovascular stimulation of autonomic neural elements in the superior vena cava using a flexible loop catheter *Jpn Heart J* **44** 417–27

[254] Stoeckel D, Bonsignore C and Duda S 2002 A survey of stent designs *Minim. Invasive Ther. Allied Technol.* **11** 137–47

[255] Palmaz J C 1993 Intravascular Stents - Tissue-Stent Interactions and Design Considerations *Am. J. Roentgenol.* **160** 613–8

[256] Shabalovskaya S A 2002 Surface, corrosion and biocompatibility aspects of Nitinol as an implant material *Biomed. Mater. Eng.* **12** 69–109

[257] Weaver F M, Follett K, Stern M, Hur K, Harris C, Marks W J Jr, Rothlind J, Sagher O, Reda D, Moy C S, Pahwa R, Burchiel K, Hogarth P, Lai E C, Duda J E, Holloway K, Samii A, Horn S, Bronstein J, Stoner G, Heemskerk J, Huang G D and Group C S P S 2009 Bilateral deep brain stimulation vs best medical therapy for patients with advanced Parkinson disease: a randomized controlled trial *JAMA* **301** 63–73

[258] Binder D K, Rau G and Starr P A 2003 Hemorrhagic complications of microelectrode-guided deep brain stimulation *Ster. Funct Neurosurg* **80** 28–31

[259] Witt K, Granert O, Daniels C, Volkmann J, Falk D, van Eimeren T and Deuschl G 2013 Relation of lead trajectory and electrode position to neuropsychological outcomes of subthalamic neurostimulation in Parkinson's disease: results from a randomized trial *Brain* **136** 2109–19

[260] Palanker D, Vankov A, Freyvert Y and Huie P 2008 Pulsed electrical stimulation for control of vasculature: temporary vasoconstriction and permanent thrombosis *Bioelectromagnetics* **29** 100–7

[261] Sawyer P N, Brattain W H and Boddy P J 1964 Electrochemical Precipitation of Human Blood Cells and Its Possible Relation to Intravascular Thrombosis *Proc Natl Acad Sci U A* **51** 428–32

[262] Sawyer P N 1983 The relationship between surface charge (potential characteristics) of the vascular interface and thrombosis *Ann N Acad Sci* **416** 561–83

[263] Dahl E, Flora G and Nelson E 1965 Electron Microscopic Observations on Normal Human Intracranial Arteries *Neurology* **15** 132–40

[264] Flora G, Dahl E and Nelson E 1967 Electron microscopic observations on human intracranial arteries. Changes seen with aging and atherosclerosis *Arch Neurol* **17** 162–73

[265] Ono M, Rhoton A L Jr, Peace D and Rodriguez R J 1984 Microsurgical anatomy of the deep venous system of the brain *Neurosurgery* **15** 621–57

[266] Rhoton A L Jr 2002 The cerebral veins *Neurosurgery* **51** S159-205

[267] Dagain A, Vignes J R, Dulou R, Dutertre G, Delmas J M, Guerin J and Liguoro D 2008 Junction between the great cerebral vein and the straight sinus: an anatomical, immunohistochemical, and ultrastructural study on 25 human brain cadaveric dissections *Clin Anat* **21** 389–97

[268] Destexhe A, Neubig M, Ulrich D and Huguenard J 1998 Dendritic low-threshold calcium currents in thalamic relay cells *J. Neurosci.* **18** 3574–88

[269] Fenoy A J and Simpson R K 2013 Risks of common complications in deep brain stimulation surgery: management and avoidance *J. Neurosurg.* **120** 132–9

[270] Patel D M, Walker H C, Brooks R, Omar N, Ditty B and Guthrie B L 2015 Adverse events associated with deep brain stimulation for movement disorders: analysis of 510 consecutive cases *Neurosurgery* **11 Suppl 2** 190–9

[271] Baizabal Carvallo J F, Mostile G, Almaguer M, Davidson A, Simpson R and Jankovic J 2012 Deep brain stimulation hardware complications in patients with movement disorders: risk factors and clinical correlations *Stereotact. Funct. Neurosurg.* **90** 300–6

[272] Hu X, Jiang X, Zhou X, Liang J, Wang L, Cao Y, Liu J, Jin A and Yang P 2010 Avoidance and management of surgical and hardware-related complications of deep brain stimulation *Stereotact. Funct. Neurosurg.* **88** 296–303

[273] Rolston J D, Englot D J, Starr P A and Larson P S An unexpectedly high rate of revisions and removals in deep brain stimulation surgery: Analysis of multiple databases *Parkinsonism Relat. Disord.*

[274] Opie N L, John S E, Rind G S, Ronayne S M, Grayden D B, Burkitt A N, May C N, O'Brien T J and Oxley T J 2016 Chronic impedance spectroscopy of an endovascular stent-electrode array *J. Neural Eng.* **13** 46020

[275] Osofsky A, LeCouteur R A and Vernau K M 2007 Functional neuroanatomy of the domestic rabbit (Oryctolagus cuniculus) *Vet Clin North Am Exot Anim Pr.* **10**713–30, v

[276] Smith K R Jr 1963 The Cerebellar Cortex of the Rabbit. An Electron Microscopic Study *J. Comp. Neurol.* **121** 459–83

6. Appendix I: Immunohistochemical markers of neural activation for DBS

6.1.Introduction

Deep brain stimulation (DBS) is an enabling technology used to treat a range of brain disorders; however, its therapeutic mechanisms remain poorly understood. Current hypotheses are primarily supported by single-cell electrophysiological recordings in preclinical animal models of DBS. While electrophysiological recordings provide cell-specific high-resolution temporal data, broad spatial cell sampling is generally impractical. Immunohistochemistry (IHC) complements electrophysiology by providing broad spatial sampling of single-cells at a single time point, but is extremely underutilized in preclinical animal model studies of DBS. In this study we hypothesized that unilateral electrical stimulation of the anterior limb of the internal capsule would drive cellular activation and increase the number of cells expressing the immediate-early genes cFos and EGR-1 in the non-human primate.

6.1.1. Methods

A small-diameter (0.635 mm) 8-electrode version of a clinical DBS lead was stereotactically implanted into the anterior limb of the internal capsule ALIC of an anesthetized rhesus macaque. Charge-balanced monopolar current-regulated 100 μsec digital pulses were delivered at 130 Hz through an electrode in the ALIC for 1.5 hours. Transcardial perfusion with 25mM phosphate buffered saline (PBS) followed by 4% paraformaldehyde in 25mM PBS (PFA) was performed 1 hour after stimulation was stopped. The brain was postfixed, cryoprotected, and sectioned at 50 μm in the coronal plane using a freezing microtome. Blockface photos were captured during sectioning through the entire brain so that three dimensional reconstructions could be used to verify lead location. Immunohistochemistry (IHC) was performed using the avidin-biotin-peroxidase complex method on free-floating sections. Primary antibody incubations were performed for 48 hours at 4°C and consisted of a polyclonal anti-cFos primary antibody (1:1000, Abcam, Cat #: ab7963) or a monoclonal anti-EGR1 antibody (1:1000, Cell signaling, Cat #: 15F7). Secondary antibody incubations were performed for 45 minutes at room temperature using a biotinylated goat anti-mouse antibody (1:200, Vector laboratories, BA-9200). Sections were processed using the Vector laboratories ABC kit and reacted with a solution of 3% H2O2, 73µg/ml DAB in 0.05 M Tris. Section images were captured using a transparency scanner and microscopy was performed using a Leica TCS SPE.

6.1.2. Results

The final DBS lead location was visually confirmed to be in the anterior limb of the internal capsule. More specifically, most distal electrode, which was used to deliver stimulation, was confirmed to in the ALIC directly between the thalamus and putamen (Figure 31).

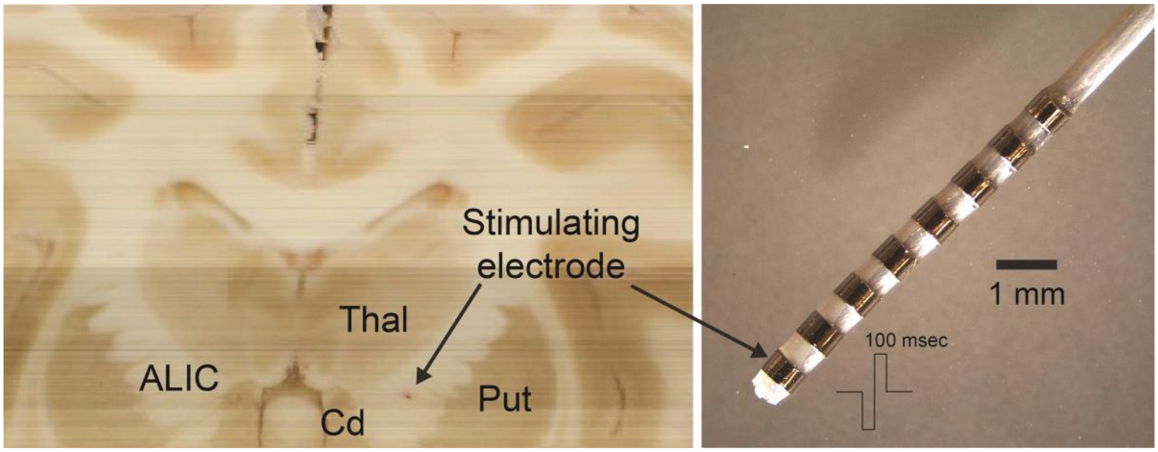

Figure 31. DBS lead and implant location. Visual inspection using three-dimensional reconstructions of blockface images from sectioning confirmed the lead location. The location of the stimulating electrode within the ALIC was confirmed through visual inspection of reconstructed blockface images.

ALIC stimulation resulted in unilateral staining of cFos and EGR-1 -like expression in two cortical regions: SMA and M1 (Figure 32 and Figure 33). Expression was only found in the hemisphere ipsilateral to stimulation and was completely lacking in the non-stimulated hemisphere. The location and region where expression was detected was comparable between cFos and EGR-1; however, more background staining was observed in the case of cFos. Expression of cFos and EGR-1 were also detected in the basal ganglia and limbic system, but with no clear hemispheric-bias in expression.

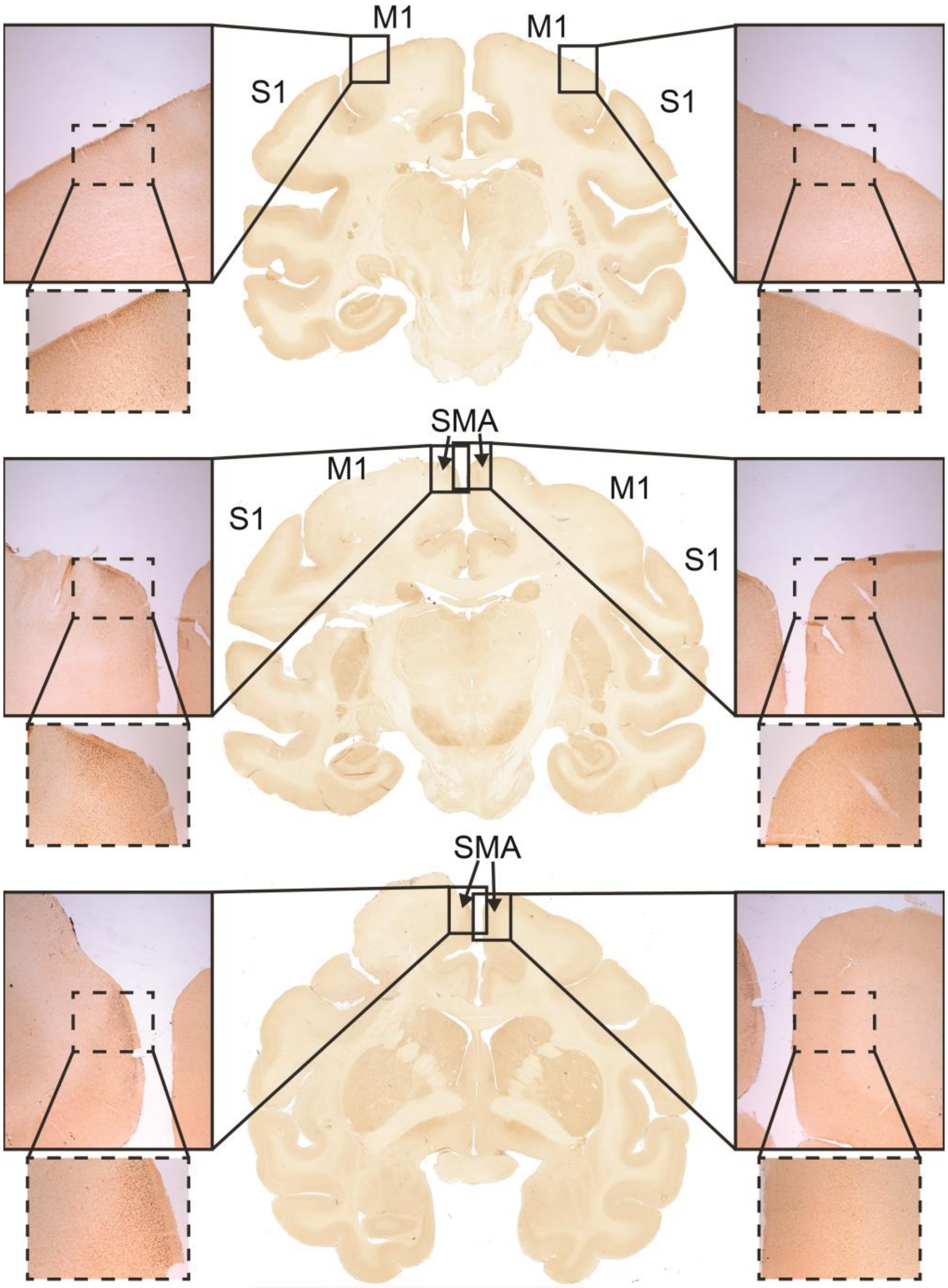

Figure 32. Results of cFos staining. cFos-like immunoreactive cells was observed ipsilateral to electrical stimulation. Brain regions with the most prominent staining included primary motor cortex (top) and supplementary motor area (middle and bottom).

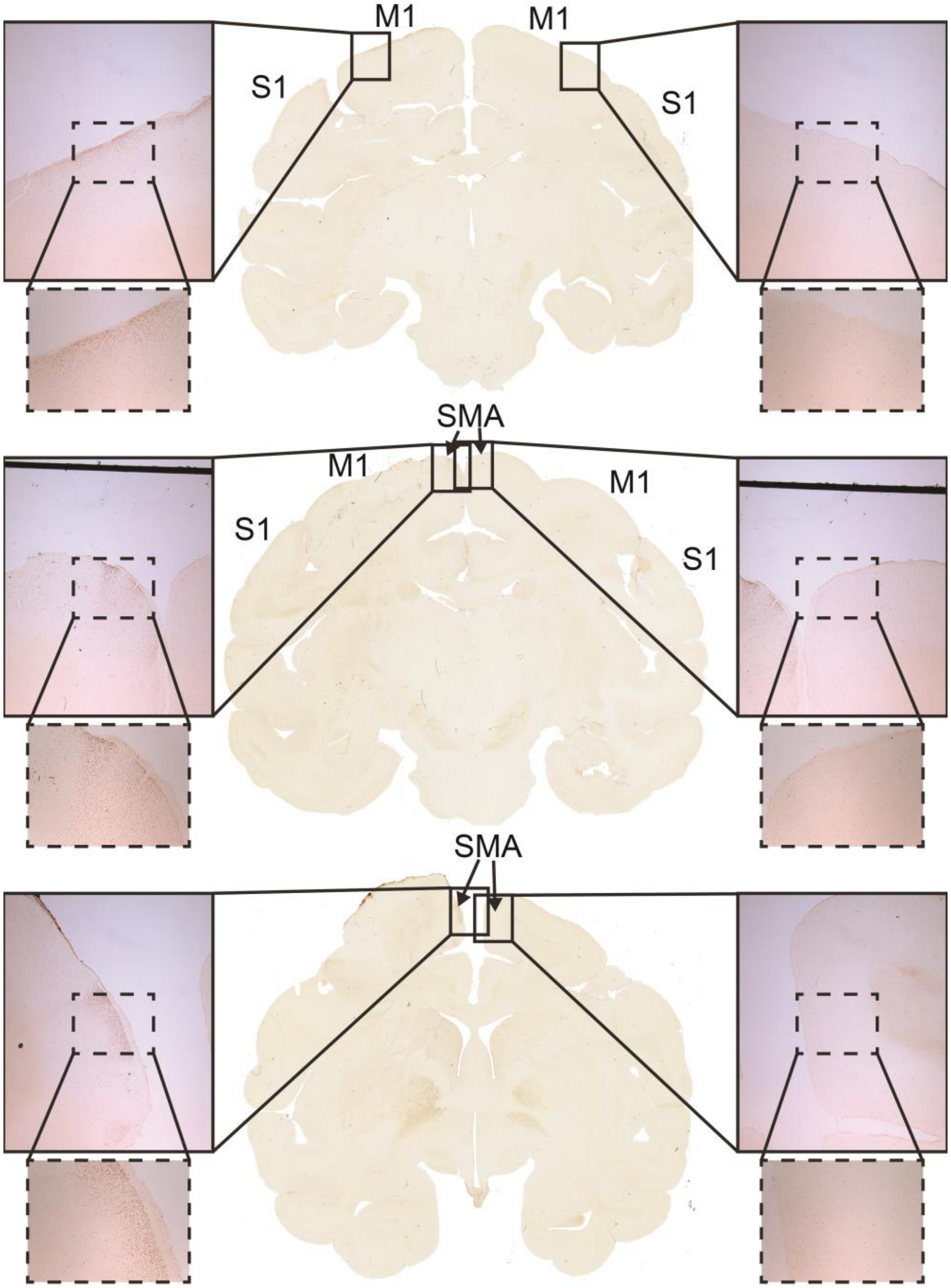

Figure 33. Results of EGR-1 staining. EGR-1-like immunoreactive cells were observed only ipsilateral to electrical stimulation. Brain regions with the most prominent staining included primary motor cortex (top) and supplementary motor area (middle and bottom).

6.1.3. Discussion

IHC can produce whole-brain analysis that provide detailed information about the spread and network effects of DBS. ALIC stimulation resulted in unilateral cFos and EGR-1 expression in two cortical regions: SMA and M1. Studies using anterograde tract-tracer labeling have demonstrated the existence of white matter projections through the ALIM to M1 and SMA in the rhesus macaque [185]. Immunohistochemical staining using antibodies targeting both cFos and EGR-1 generated results that are in alignment with anterograde tract-tracer labeling and suggest that increased cFos and EGR-1 expression in the brain hemisphere ipsilateral to stimulation identified cortical cells that are actively driven by DBS within the ALIC. Further, these results demonstrate that IHC can be a powerful tool for determining which brain regions are driven during deep brain stimulation.

7. Appendix II: Endovascular neural stimulation in a rabbit

7.1.Introduction

Although transvascular brain stimulation has never been formally investigated, demonstrations of transvascular VNS in dogs [247] and transvascular brain recording in pigs [62] provide a basis for developing such a technique. The goals of this work include development of a rabbit model of transvascular neural stimulation by determining a vascular approach to from the rabbit femoral vein/artery to the brain and demonstrating transvascular neural stimulation in the periphery.

7.2.Methods

7.2.1. Subject and imaging

CT angiography was performed on one New Zealand White rabbit. Anesthesia was initiated by intramuscular injection of ketamine-xylazine (34 mg/kg-5 mg/kg) and maintained with isoflorine (1.5-3.0%) delivered via nose cone. In each animal, the femoral vein was catheterized, standard CT was captured, and CT angiography was captured at 10, 20, and 30 seconds following contrast injection (Figure 34a). The skeleton, veins, arteries, and the brain were reconstructed using a combination of thresholding and dynamic region growing using Mimics Innovation Suite (v15.0, Materialise, Leuven, Belgium).

7.2.2. Surgical procedure and stimulation protocol

An endovascular approach was used to implant a 36 AWG 316 stainless steel Teflon insulated wire electrode (Cooner Wire Company, Chatsworth, CA) to the internal jugular vein in an anesthetized New Zealand White rabbit. The electrode was prepared by removing precisely 1 mm of insulation from the distal tip of the transvascular guidewire. Using a femoral approach, a 4 french endovascular catheter was placed adjacent to the vagus nerve in right side internal jugular vein, just distal of the internal and external branches. Transvascular electrical stimulation was delivered using an external waveform generator and dual current isolation units (S88X and SIU-C, Grass Technologies, West Warwick, RI) using a monopolar, charge-balanced, repeating waveform (135 Hz, 90 µs cathodic pulse width). A veterinary patient monitor (BM5Vet, Bionet America, Inc, Tustin, CA) was used to record SpO2 and EKG before, during, and after a 15-second transvascular stimulation block.

7.3.Results

7.3.1. Anatomical rabbit reconstructions

The endovascular trajectory for reaching the sigmoid sinus in the rabbit was found to require navigation through the external jugular vein as opposed to the internal vein as in humans. In alignment with previous reports on rabbit vascular anatomy [275,276], the external jugular vein was found to follow the lateral edge of the neck and enter the skull near the base of the skull at the mandibular joint (Figure 34b). Reconstructions estimated the diameter of the sigmoid sinus to be approximately 2 mm in diameter.

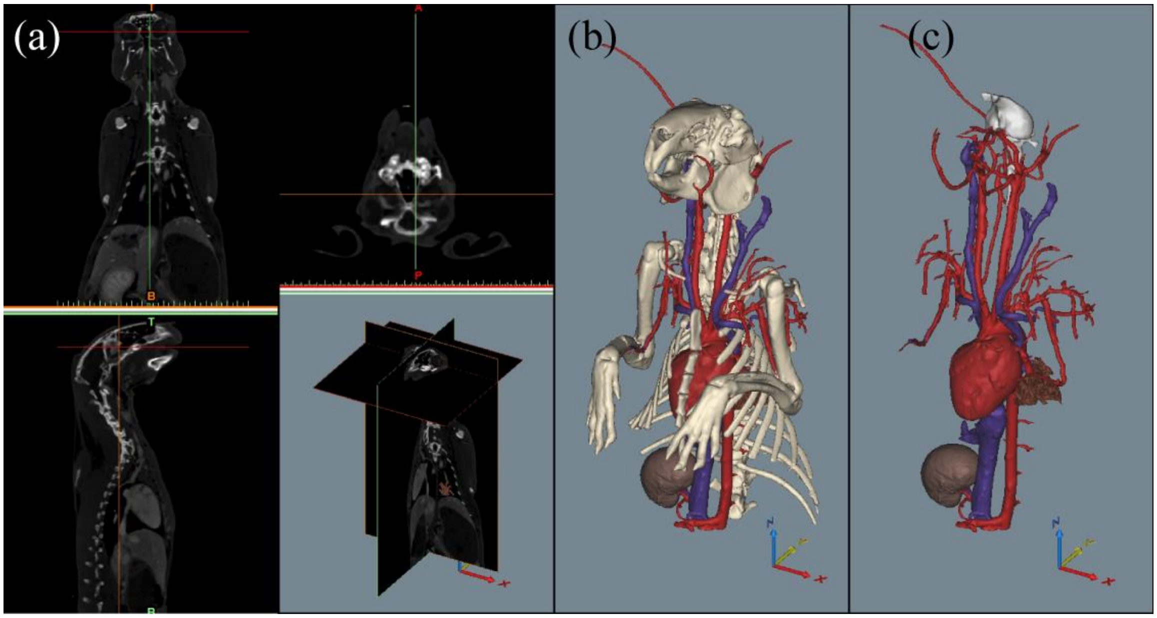

Figure 34. Vascular reconstruction of the New Zealand white rabbit. Radiopaque CT angiography (a) in a single subject and subsequent reconstructions of the skeleton (b), veins, arteries, and the brain (c).

7.3.2. Transvascular vagus nerve stimulation

Respiration rate was observable within the SpO2 and EKG traces and stimulation artifacts were observable within the EKG trace, only. No clear behavioral outcome was observed during low amplitude, ≤ 2 mA stimulation (0.1 mA shown); however, counts of the visible cardiac R-waves during stimulation indicate the occurrence of stimulation induced bradycardia (Figure 35, top). Moderate stimulation amplitudes, 3-5 mA increased respiration rate (Figure 35, bottom) and high stimulation amplitudes, ≥ 5 mA produced visible neck muscle contractions. The cardiac rhythm and repertory pattern observed during low and moderate stimulation were rhythmic, but neither was synchronized to stimulation frequency.

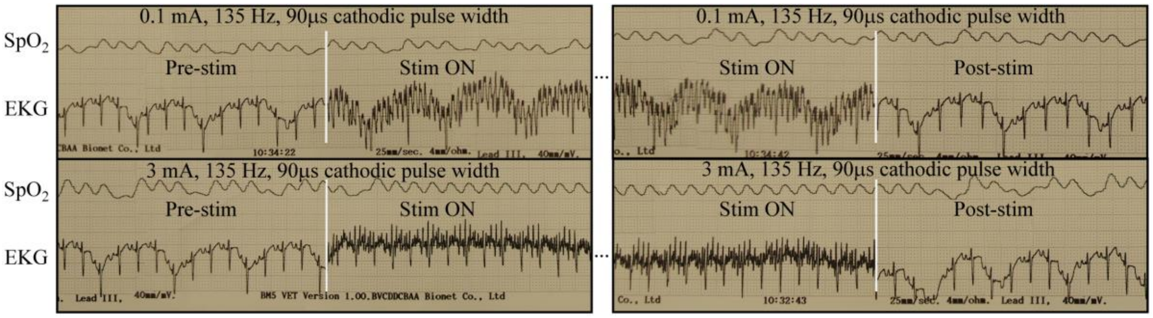

Figure 35. Endovascular vagus nerve stimulation in the rabbit. Low amplitude transvascular electrical stimulation delivered via endovascular internal jugular vein wire electrode produced no clear behavioral effect (top). Moderate amplitude stimulation modulated respiration rate.

7.4.Discussion

Bradycardia and altered respiratory patterns are commonly reported effects of transvascular vagus nerve stimulation (VNS) in healthy anesthetized animal preparations [75, 128]. These data indicate that the effects of low and moderate electrical stimulation were a result of successful neuromodulation through transvascular VNS in an anesthetized rabbit preparation.